Elaboration de polypropylène ou de polystyrène à l'aide du dioxyde de carbone supercritique : procédé, microstructure, propriétés mécaniques

Jin-Biao Bao

Nancy-Université INPL

en co-tutelle avec l'East-China University of Science and Technology

Ecole Doctorale : Ressources Procédés Produits Environnement (RP2E)

Ecole Nationale Supérieure des Industries Chimiques (ENSIC)

Laboratoire Réactions et Génie des Procédés (LRGP-CNRS UPR 3349)

Elaboration de polypropylène ou de polystyrène à l'aide du dioxyde de carbone supercritique : procédé – microstructure – propriétés mécaniques

Supercritical carbon dioxide assisted toughening of polypropylene or polystyrene: process, microstructure and mechanical properties

THESE

présentée en vue de l'obtention du

DOCTORAT DE L'INSTITUT NATIONAL POLYTECHNIQUE DE LORRAINE

Spécialité : Génie des Procédés et des Produits

par

Jin-Biao BAO

Soutenance prévue le 16 décembre 2011 à 15:30

Composition du jury :

Rapporteurs :	Jacques FAGES	Professeur à l' Ecole des Mines d'Albi
	Lian-fang FENG	Professeur à l'Université de Zhejiang, Chine
Examinateurs :	Guo-Hua HU	Professeur à l'INPL et membre de l'IUF
	Ling ZHAO	Professeur à l'East-China University of Science and Technology

Abstract

In a conventional supercritical carbon dioxide ($scCO_2$) batch foaming process, CO_2 is dissolved in a polymer matrix, which increases the free volume between molecular chains and chain mobility, and consequently affects its crystallization behavior. After the saturation process, CO_2 is depressurized quickly to induce foaming in the polymer matrix. This type of process normally produces microcellular foams with an average cell size of about 10 μm and a cell density of more than 10^9 cells/cm^3. Properties and applications of polymer foams depend very much on cell morphologies. As a widely used general-purpose polymer due to its excellent performance-to-price ratio, polypropylene (PP) and polystyrene (PS) have been widely studied and their foaming has also been subjected to intense studies. In this work, $scCO_2$ induced foaming of PP or PS is systematically studied with emphasis on the relationship between process, microstructure and mechanical properties.

The first part of the thesis deals with the toughening of iPP by $scCO_2$ induced crystallization for the fine separation of rigid crystalline domains and soft amorphous ones in the polymer matrix. The results indicate that the toughness of injection molded iPP specimens can be significantly improved without loss of strength by controlled shearing, CO_2 induced re-crystallization and adequate cooling. Under shear, a high degree of orientation can be obtained with “shish-kebab” crystals formed in the shear zone. During the subsequent CO_2 treatment, a crystal network morphology may be formed as a result of an increase in the number of the primary lamellae and that of crosshatched subsidiary lamellae, which leads to an increase in the toughness. In addition, quenching in ice-water of $scCO_2$ treated iPP promotes the formation of nano-sized mesomorphic phase domains in the shear zone, which further toughens the iPP. The impact strength of the best toughened iPP is more than 12 times that of the original one while retaining the tensile strength and modulus.

Moreover, the highly oriented iPP with “shish-kebab” and “spherulite” are used for CO_2 foaming to investigate the effect of crystalline structure on the formation of cell nucleation and growth. The impact property is also studied. A nanocellular foam is achieved by CO_2 foaming of shish-kebab crystalline structure in the solid state. The underlying principle is localized cell nucleation and growth in amorphous domains confined by the shish-kebab crystalline domains. Therefore, nano-cells are generated in amorphous domains confined by shish-kebab crystalline domains which cannot foam. At a chosen CO_2 pressure, the cell morphology depends very much on the foaming temperature, as the crystal morphology depends on the temperature when the CO_2 pressure is constant. Moreover, the impact tests

indicate that the nanocellular bubbles among the network crystals structure can further toughen the $scCO_2$ treated iPP.

In addition, the effect of the foaming conditions and the cell structural parameters of PS foams on the mechanical properties are studied systematically. PS foams with isotropic cell morphology and oriented cell one are prepared. For the isotropic cell morphologies, the mechanical properties of the PS foams increase with increasing relative density. When the relative density is constant, the cell size does not affect the tensile strength and modulus but has a slight effect on the impact strength. The relative impact strength increases with decreasing cell size. The results indicate that the solid area fraction on the fracture surface (f_s) and the cell walls are the key parameters for toughening PS foams. For oriented foams, the cell morphologies oriented perpendicular to the impact direction could significantly enhance the impact properties of PS foams. Moreover, the oriented cells along the tensile direction and the oriented molecular chains sheared by the bubbles may both lead to the improvement of strength in the oriented direction. On the other hand, the cells oriented in the other two directions result in the poor impact properties, because their larger f_s and worse dispersion of cell walls compared with those of isotropic foams.

Finally, a two-step depressurization batch process is developed to produce bi-modal cell structure PS foams by using $scCO_2$ as the blowing agent. This unique cell structure with both small and large cells homogenously distributed throughout the entire volume of the foam sample might have particular properties which include both advantages of small cells and large cells. The results indicate that the bi-modal cell structure foams can be achieved by depressurization in two distinct steps and can be significantly affected by the process parameters. For both bi-modal foams and uniform foams, the relative impact strength increases with increasing relative density. When the relative density is constant, the impact strength of bi-modal foams increases with increasing f_s. Moreover, when f_s is 80%, the relative impact strengths of bi-modal foams are always higher than those of the uniform one, with relative density ranging from 0.2 to 0.5. It indicates that the bi-modal cell structure could have stronger absorption of impact energy than the uniform one.

Keywords: polypropylene, polystyrene, $scCO_2$, crystallization, foam, mechanical property

RESUME

Dans un procédé de moussage discontinu classique par le dioxyde de carbone supercritique ($scCO_2$), le CO_2 est dissout dans une matrice polymère, ce qui augmente le volume libre entre les chaînes et leur mobilité et par voie de conséquence influe sur son comportement de cristallisation. Après une phase de saturation, le CO_2 est rapidement dépressurisé afin d'amorcer le moussage au sein de la matrice polymère. Normalement ce type de procédé produit des mousses micro-cellulaires avec une taille moyenne de cellules de l'ordre de 10 µm et une densité de cellules supérieure à 10^9 cellules/cm^3. Les propriétés et les applications de mousses en polymères dépendent beaucoup de la morphologie des cellules. En tant que polymères de grande diffusion dûs à leur excellent rapport performance – prix, le polypropylène (PP) et le polystyrène (PS) ont été largement étudiés et leur comportement de moussage a aussi fait l'objet d'études intenses. Dans ce travail, le moussage du PP et du PS par le $scCO_2$ est étudié de manière systématique avec l'accent sur la relation entre le procédé, la microstructure et les propriétés mécaniques.

La première partie de cette thèse porte sur l'amélioration de la résistance au choc du PP par cristallisation induite par le $scCO_2$ qui vise à obtenir une séparation fine des domaines cristallins rigides et amorphes mous dans la matrice polymère. Les résultats obtenus montrent que la résistance au choc des échantillons du PP injectés est fortement améliorée sans perte de module grâce au contrôle adéquat de la re-cristallisation et du refroidissement. Lors de l'injection, des cristaux à structure « shish-kebab » sont formés dans la zone de fort cisaillement et sont hautement orientés. Le traitement au CO_2 conduit à la formation d'une morphologie de cristaux en réseaux due à l'augmentation du nombre de lamelles primaires et de celui des lamelles subsidiaires hachurés de manière latérale, ce qui contribue à une amélioration de la résistance au choc du PP. Notons que la résistance au choc la plus élevée est plus que 12 fois celle du PP vierge alors que la force de traction et le module demeurent inchangés.

Dans un deuxième temps, le PP fortement orienté avec des structures shish-kebab et sphérolite est utilisé pour étudier l'influence de la structure cristalline sur la nucléation et la croissance des cellules pendant le procédé de moussage sous le $scCO_2$. Une mousse nano-cellulaire est obtenue avec une structure shish-kebab à l'état solide sous $scCO_2$. Le principe est que la nucléation et la croissance de cellules se font dans les domaines amorphes qui sont confinés par ceux à structure shish-kebab crystalline qui ne peuvent pas mousser. Pour une pressure CO_2 donnée, la morphologie de cellules dépend fortement de la

température de moussage car à pressure CO_2 constante, la morphologie cristalline dépend de la température. Par ailleurs, il a été démontré que la présence de cellules nanométriques dans une structure crystalline en réseaux améliore davantage la résistance au choc du PP traité au préalable par le $scCO_2$.

Ensuite, les influences des conditions de moussage ainsi que celles des paramètres structuraux de la mousse de PS ont été étudiées. Les mousses de PS à cellules isotropes ont été comparées avec celles de PS à cellules orientées. Dans le premier cas, les propriétés mécaniques augmentent avec la densité relative de la mousse. A densité relative constante, la taille des cellules n'influe pas sur la force de traction et le module mais un peu sur la résistance au choc relative. La résistance au choc relative augmente avec la taille des cellules. Il a été démontré que la fraction de l'aire solide sur la surface de fracture (fs) ainsi que les parois de cellules sont les paramètres structuraux clés qui régissent la résistance au choc de la mousse de PS. Dans le cas des cellules orientées, les mousses dont les celles sont orientées de manière perpendiculaire à la direction ont une résistance au choc plus élevée que celles dont les cellules sont réparties de manière isotrope. De plus, l'orientation des cellules suivant la direction de la traction et celle des chaînes polymères par les cellules contribuent toutes les deux à l'amélioration de la force de traction dans la direction de l'orientation.

Enfin, un procédé de moussage discontinu en deux étapes est développé afin de produire des mousses de PS à cellules bi-modales en utilisant le $scCO_2$ en tant qu'agent de moussage. Cette structure unique de petites et grandes cellules réparties de manière homogène au travers de l'ensemble du volume de la mousse confère à cette dernière des propriétés particulières. Il a été démontré qu'une telle structure peut être obtenue par dépressurisation en deux étapes distinctes et qu'elle peut être fortement influencée par les paramètres du procédé. Pour les mousses bi-modales et uniformes, la résistance au choc relative augmente avec la densité relative. A densité relative constante, la résistance au choc relative des mousses bi-modales augmente avec fs. De plus, quand fs est de 80% et lorsque la densité relative varie entre 0,2 et 0,5, la résistance au choc relative des mousses bi-modales est que celles des mousses uniformes, ce qui signifie qu'une mousse bi-modale peut absorber plus d'énergie au choc qu'une mousse uniforme.

Mots-Clés : polypropylène, polystyrène, $scCO_2$, cristallisation, mousse, propriétés mécaniques.

Table of content

Chapter 1 Introduction

1.1 Motivation and objectives

Recently carbon dioxide (CO_2) has been increasingly explored for polymer preparation and processing including polymer functionalization, crystallization and foaming [1-5]. The effect of CO_2 on the crystallization behavior of polymers has been widely studied. The dissolution of CO_2 in the polymer increases the free volume between molecular chains and chain mobility, and consequently affects its crystallization behavior [6-12]. Moreover, microcellular foams with average cell sizes of less than 10 microns and cell densities greater than 10^9cells/cm^3 are generated [13,14]. Foams with such structures were proposed by Suh et al. [15, 16] in the early 1980s as a means to reduce materials consumption and to increase the toughness of such cellular materials. The initial idea of the toughening mechanism is using microbubbles to substitute rubber parties in polymer matrices for toughening.

As a widely used general-purpose polymer due to its excellent performance-to-price ratio, polypropylene (PP) and polystyrene (PS) have been widely studied, including their foaming [17-21]. However, both of them exhibit low impact toughness which greatly limits their application potential. Toughening of polymers has been a subject of intense studies [22-32]. Toughening methods include copolymerization of polymer with other types of olefin monomers, blending of polymer with particles or a phase separated second polymer, and addition of a nucleating agent. In one word, the basic concept of toughening is to make the finely separated phases in the polymer matrix for impact energy absorption. Unfortunately, the enhancement of toughness is often at the expense of other properties such as strength and heat resistance [33]. There are extremely few successful examples for simultaneously efficiently reinforcing and toughening PP and PS [34-36]. Thus, it is a great challenge to enhance the performance of PP and PS for both strength and toughness.

For semi-crystalline polymers such as isotactic polypropylene (iPP), their final properties are dictated by their crystallinity and crystalline morphology, which in turn are affected by the thermomechanical history (flow and temperature) they have experienced during processing [37-41]. It has been well established that for iPP oriented crystals (i.e., shish-kebabs) can bring out notable reinforcement on iPP. However, the improvement in performances of polymers seems to be available only in the oriented direction [35, 36, 40]. In the perpendicular direction, the performances such as impact strength are often more or less reduced. To a certain extent, the crystals in the semi-crystalline polymer matrix can be

considered as fillers in a multiphase system, in which the crystal is one phase and the amorphous is another phase. Especially for the iPP sample with the shish-kebab crystalline structure, the oriented crystals can be considered as the rigid phase in nano size. In this way, the theories established for other multiphase systems can be applied to the iPP sample with shish-kebab crystalline structure. Naturally, an idea arises that the increase of the oriented crystals in the perpendicular direction could improve the impact strength of the iPP samples. Therefore, the highly oriented iPP are subjected to re-crystallization in the solid state under $scCO_2$. With the additional fine lamellae generated, a network crystalline structure is formed and the toughness of the highly oriented iPP will be improved while retaining the high tensile strength.

Furthermore, in the case of a solid-state foaming process, the crystal structure of the iPP may have a great effect on the cell formation and cell morphology, as cell nucleation and growth only occur in amorphous regions where CO_2 is dissolved [17, 42]. On the other hand, it is well-known that the so-called shish-kebab structure consists of a long central fiber core (shish) surrounded by lamellar crystalline structure (kebab) periodically attached along the shish [43-45]. In other words, the amorphous domains among the crystal domains are confined in nanometer scale by the shish-kebab crystalline structure. Therefore, it is expected that the use of a highly oriented iPP with a shish-kebab crystalline structure as a template may lead to nanocellular morphology by CO_2 foaming. With the formation of the nano-bubbles among the network crystalline structure, the mechanical properties of iPP samples are expected to be further increased.

For the amorphous polymer, PS, it is a brittle material. The aim of this work is to toughen the PS foams by introducing the micron bubbles as the particles into the PS matrix while reducing materials consumption. It is well-known that the properties and applications of polymeric foams depend very much on cell morphologies [46-50]. In the past decade, efforts have been made to investigate the influence of processing conditions and the nature of polymers on the final cell morphologies of polymer foams [51-54]. Moreover, the effect of cell morphologies on impact strength of microcellular foams has also been studied in several polymer systems and the results have been mixed [55-66]. In this study, a systematic study of the effect of the foaming conditions and the cell structural parameters of PS foams on the mechanical properties was first presented. Thereafter, the oriented, anisotropic cell morphologies were prepared to investigate the relationship between the directions of cell oriented and the corresponding tensile and impact strength. Finally, a two-step depressurization process of CO_2 foaming was studied for producing bimodal cell structure

PS foams. The relationship between the processing parameters, the final bimodal cell structure and the corresponding mechanical properties were investigated.

The objective of the work presented in this thesis is as follows: (a) study the crystallization behavior of iPP with CO_2 to tune and control the crystalline structure of iPP for toughening; (b) CO_2 foaming of highly oriented iPP with various crystal morphologies to investigate the effect of crystalline structure on the formation of cell nucleation and growth; (c) systematically study the effect of the foaming conditions and the cell structural parameters of PS foams on the mechanical properties; (d) study a two-step depressurization process for producing bimodal cell structure PS foams by using scCO_2 as blowing agent with emphasis on the relationship between the processing parameters, the final bimodal cell structure and the corresponding mechanical properties.

1.2 overview of thesis

A brief overview of this thesis is as follows.

Chapter 2 describes the main experiments in this study.

Chapter 3 proposes a novel process for significantly toughening isotactic polypropylene (iPP) by finely tuning and controlling the structure and morphology of iPP. The toughness of injection molded iPP specimens can be significantly improved by controlled shearing, CO_2 induced recrystallization and adequate cooling without loss of strength. Under shear, a high degree of orientation can be obtained with “shish-kebab” crystals formed in the shear zone. During the subsequent CO_2 treatment, a crystal network morphology may be formed as a result of an increase in the number of the primary lamellae and that of crosshatched subsidiary lamellae, which leads to an increase in the toughness. Wide-angle X-ray diffraction patterns indicate that quenching in ice-water of scCO_2 treated iPP promotes the formation of nano-sized mesomorphic phase domains in the shear zone, which further toughens the iPP. The impact strength of the best toughened iPP is over 12 times that of the original one without loss in tensile strength and modulus.

In chapter 4, the injection molded iPP samples with “shish-kebab” and spherulite were used for CO_2 foaming to investigate the effect of crystalline structure on the formation of cell nucleation and growth. A nanocellular foam was achieved by CO_2 foaming of shish-kebab crystalline structure in the solid state. Nano-cells are generated in amorphous domains confined by shish-kebab crystalline domains which cannot foam. At a chosen CO_2 pressure, the cell morphology depends very much on the foaming temperature. Moreover, the relationship between the cell structure and the mechanical properties are studied.

In chapter 5, a systematic study of the effect of the foaming conditions and the cell structural parameters of PS foams on the mechanical properties is first presented. After that, the oriented, anisotropic cell morphologies are prepared to investigate the relationship between the directions of cell oriented and the corresponding tensile and impact strength. The results indicate that the oriented cells perpendicular to the impact direction could significantly improve the toughness of PS foams, compared with those of isotropy foams.

In chapter 6, the method of two-step depressurization batch process is developed to produce bi-modal cell structure PS foams by using $scCO_2$ as the blowing agent. Bi-modal cell structure foams could be achieved by depressurization in two distinct steps and could be significantly affected by the process parameters. The process conditions at the holding stage between the two steps are the key to controlling the bi-modal cell structure. In addition, the relationship between the cell structure and the mechanical properties are studied.

Chapter 2 Experimental

2.1 Materials

The materials used in this thesis are as follows:

Product designation	Characteristics	Supplier
Polypropylene (RS1684)	Mass average molar mass and polydispersity index were 231800 g/mol and 14.8, respectively.	LyondellBasell Industries.
Polystyrene (158K)	Mass average molar mass and polydispersity index were 335000 g/mol and 2.85, respectively.	Yangzi-Basf Styrenics Co., Ltd.
Carbon dioxide	(purity: 99.9% w/w)	Air Products Co., Shanghai, China.

2.2 Sample preparation

2.2.1 Preparation of polypropylene specimen by injection molding

The iPP was injection-molded on an 80-ton Chen Hsong injection molding machine equipped with an instrumented mold to make ASTM-D256 impact bars and ASTM-D638 tensile bars. It is well-known that the alignment of macromolecules along a perferred direction is the result of a conpetition between the characteristic relaxation time, λ, which is a function of thermomechanical and crystallinity histories, and the flow characteristic time, t_f, which is the reciprocal of the deformation rate. High orientation levels can be reached when the ratio t_f/λ is high [37]. Therefore, two iPP specimens were injection-molded under two different sets of conditions: PP1 under standard conditions (the melt temperature is 200 ^{o}C, mold temperature is 100 ^{o}C and injection speed is 70%) and PP2 under conditions (the melt temperature is 180 ^{o}C, mold temperature is 40 ^{o}C and injection speed is 30%) that were more favorable for orienting the iPP. In both cases the holding pressure and holding time were 200 bar and 10 s, respectively. Prior to the CO_2 treatment, both PP1 and PP2 specimens were annealed in a vacuum oven at 110 ^{o}C for 5 h in order to remove their previous thermal history.

2.2.2 Preparation of polystyrene specimen

A Haake MiniJet (Thermo Electron, Germany) equipped with an instrumented mold was employed to make PS specimens. The cylinder temperature and mould temperature were 190 and 60 ^{o}C, respectively. The injection pressure was 800 bar and the injection time was 3 second. The post pressure and holding time were 650 bar and 60 second, respectively.

Prior to the CO_2 treatment, the PS specimens were annealed in a vacuum oven at 100 ^oC for 5 h in order to remove their previous thermal history.

2.2.3 CO_2 swelling of samples

The swelling process was performed under CO_2 in a high-pressure vessel placed in a homemade oil bath with a temperature controller (Figure 2.1) [17, 20, 42]. The temperature of the oil bath was controlled at a desired temperature with an accuracy of ±0.2 ^oC. After the high-pressure vessel was purged with low-pressure CO_2, a given amount of CO_2 was pumped into the vessel. The CO_2 loading was achieved by a DZB-1A syringe pump of Beijing Satellite Instrument Co., China, with an accuracy of 0.01 cm^3. The specimens were saturated with CO_2 under prescribed pressure and temperature for at least 5h so that the saturation was surely reached. Then, it was cooled in an ice-water bath or in the ambient water before the CO_2 was released. The cooling rates for "ice-water bath" and "ambient water" were about 30 K/min and 12 K/min, respectively.

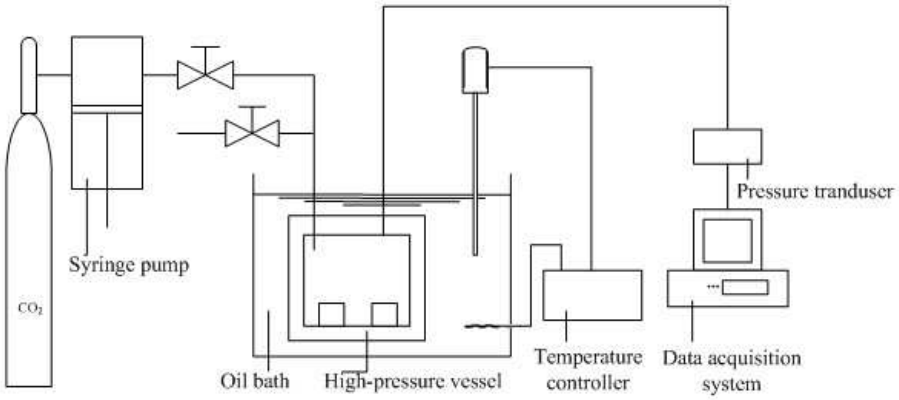

Fig. 2.1 Schematic of the CO_2 treatment apparatus.

2.2.4 Foaming process

The foaming process was also performed with CO_2 in a high-pressure vessel placed in a homemade oil bath with a temperature controller as shown in Fig. 2.1. The samples were saturated with CO_2 under prescribed pressure and temperature for a certain time in order that the saturation conditions were largely reached. Thereafter, the valve was rapidly opened to release the CO_2 in the high-pressure vessel to ambient pressure. Once the pressure was completely released, the high-pressure vessel was quickly opened up to take out the foamed samples for subsequent analyses. The maximum value of the depressurization rate was denoted as the depressurization rate of each foaming process. Fig. 2.2 shows the pressure change during a typical depressurization process.

For confined foaming, the samples were put into a mould in the vessel and the mould was adjusted in size to restrict the foam expansion with the walls of the mould. Therefore, the foam expansion could be controlled to grow in one direction (a-axis, b-axis or c-axis) with the other two directions confined (Fig. 2.3). After foaming, the cells were drawn into cylinder-like geometries. Three different cell morphologies could be observed on cross section (as shown in Fig. 2.3). Thus, the foams with three series of cell orientation distribution were employed for mechanical properties tests (impact direction is perpendicular to c-axis).

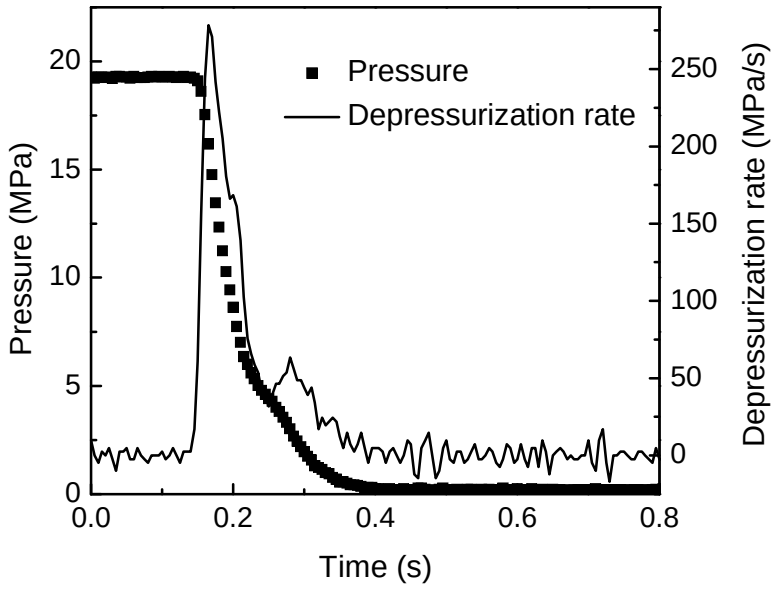

Fig. 2.2 Changes in pressure and depressurization rate with time during a typical depressurization process.

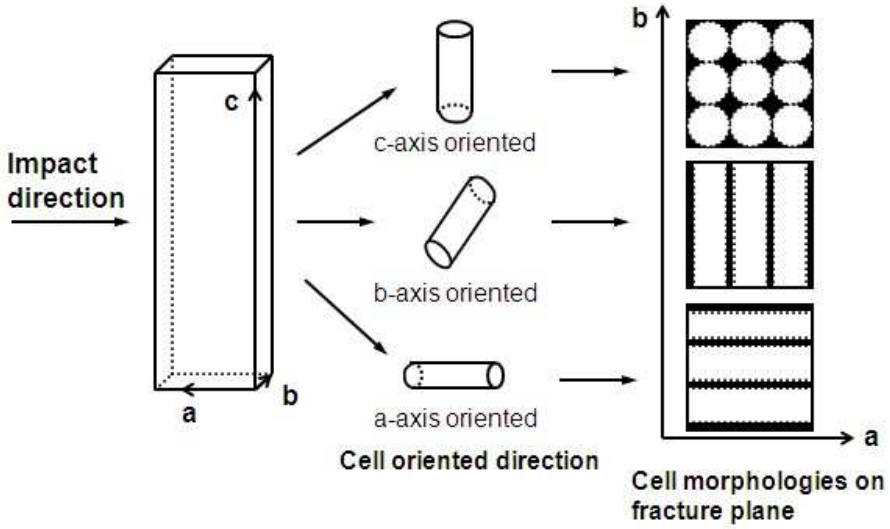

Fig. 2.3 Schematic of cell oriented growth in the mould during the confined foaming.

2.3 Characterization

2.3.1 Mechanical properties

The tensile test was performed at 23 ^{o}C according to ASTM D-638 at a cross-head speed of 5 mm/min, while to evaluate the tensile modulus, a draw speed of 1 mm/min was applied. The notched and non-notched impact tests were carried out at 23 ^{o}C according to ASTM D-256. At least five to ten samples were tested. All CO_2-treated samples were allowed to desorb gas for at least two weeks before property testing. For the reference of unfoamed PS, prior to the mechanical tests, the specimens were swelling under CO_2 pressure of 20 MPa and temperature of 100 ^{o}C for at least 5h before cooling in an ice-water bath. Then the unfoamed samples were allowed to desorb gas for at least two weeks before property testing.

2.3.2 PLM analysis

The iPP specimens were cut into slices of about 25 μm thick using a Leica slit microtome from their central positions (see Figure 2.4). They were analyzed by polarized light optical microscopy (Leika Metalographic Aristomet model) to visualize crystal orientation.

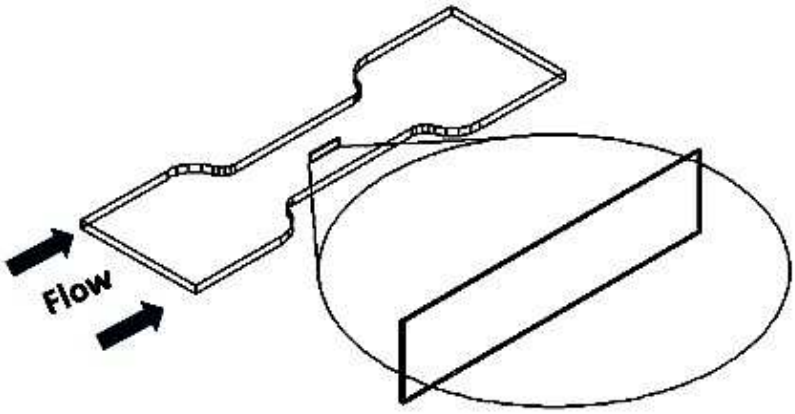

Fig. 2.4 Schematic of the positions of iPP samples for optical light microscopy

2.3.3 DSC analysis

High-pressure DSC of type NETZSCH DSC 204 HP was used to characterize the melting behavior of the iPP specimens under high pressure CO_2. About 5 to 10 mg of an iPP film was held at 30^{o}C under CO_2 at a desired pressure for 2h to ensure full saturation of the film with CO_2 before heating [3]. It was then heated from 30 to 200 ^{o}C at 10 ^{o}C/min. The

thermophysical properties of the foamed iPP were also measured under nitrogen. The crystallinity (X_c) can be evaluated from the heat evolved during crystallization (ΔH_c) using the following relation:

$$X_c = \frac{\Delta H}{\Delta H_m^0} \times 100\% \quad (2.1)$$

where ΔH was the enthalpy of crystallization per gram of sample and ΔH_m^0 the enthalpy of crystallization per gram of 100% crystalline iPP. The latter was 209 J/g [67].

2.3.4 WAXD analysis

WAXD of type Rigaku D/max 2550 VB/VC X-Ray Diffractometer (Cu Kα Ni-filtered radiation) was used to study their crystalline structures. The scan rate was 1°(θ)/min and the diffraction angle 2θ ranged from 3 to 50°. Subsequently, through deconvoluting the peaks of WAXD profiles, the overall crystallinity X_c was calculated by

$$X_c = \frac{\sum A_{cryst}}{\sum A_{cryst} + \sum A_{amorp}} \quad (2.2)$$

where A_{cryst} and A_{amorp} are the fitted areas of crystal and amorphous, respectively. The relative amount of the β-form crystal K_β was evaluated by the method of Turner-Jones et al.[68]

$$K_\beta = \frac{A_\beta(300)}{A_\beta(300) + A_\alpha(040) + A_\alpha(110) + A_\alpha(130)} \quad (2.3)$$

$A_\beta(300)$ was the area of the (300) reflection peak; $A_\alpha(040)$, $A_\alpha(110)$, and $A_\alpha(130)$ were the areas of the (040), (110) and (130) reflection peaks, respectively. Meanwhile, the crystallinity of the β-form crystal X_β was given by

$$X_\beta = K_\beta X_c \quad (2.4)$$

2.3.5 SAXS analysis

Small angle X-ray scattering (SAXS) measurements were conducted to monitor the formation of shish and lamellar crystals or kebab, which were carried out on the BL16B1 beamline in the Shanghai Synchrotron Radiation Facility (SSRF). Two-dimensional diffraction patterns were recorded using an image intensified CCD detector. All

experiments were carried out at room temperature with the radiation wavelength λ = 0.154 nm. The scattering intensities were corrected for absorption, background scattering, and incident X-ray fluctuations of the samples.

2.3.6 FTIR analysis

The orientation of the amorphous and crystalline phases of the iPP samples from the skin to the core was measured by Fourier transform infrared spectroscopy (FTIR). The orientation function was calculated as:

$$f = \left(\frac{D-1}{D+2} \right) \tag{2.5}$$

where D was the dichroic ratio, namely the ratio between the absorbance of the infrared radiations polarized along the directions parallel and perpendicular to the orientation one. For the orientation function of the crystal phase, f_c, the band 998 cm^{-1} was considered. D was then the ratio between the absorbance in the parallel direction $A_{=}$ at 998 cm^{-1} and the corresponding one in the perpendicular direction $A_{\perp}$. As for the amorphous phase bands, the peak at 973 cm^{-1} was the most commonly adopted [37].

2.3.7 SEM analysis

To observe the crystalline morphology, iPP sample surfaces were etched by permanganic acid. Then, the surfaces of all the samples were gold-sputtered to enhance conductivity. Their morphologies were observed with scanning electron microscopy (SEM) of type NOVA NanoSEM 230 with an operating voltage of 500 Kv. To observe the cell morphologies, the foamed samples were immersed in liquid nitrogen for 10 min and then fractured. After that, the surfaces of all the foamed samples were gold-sputtered and characterized by a JSM-6360LV scanning electron microscopy (SEM).

2.3.8 Foam characterization

The mass densities of foamed samples were determined using a balance equipped with the density measurement kit provided by Mettler Toledo. This method involved weighing specimen in air and water, respectively. When weighing a specimen in water, a net-like metal cover was used to immerse the specimen in water. According to ASTM 792-00, the mass densities of foamed PP, ρ_f, was calculated by:

$$\rho_f = \frac{a}{a+w-b}\rho_{water} \tag{2.6}$$

where a is the apparent mass of specimen in air, w is the apparent mass of the totally immersed net-like metal cover in water and b is the apparent mass of specimen and cover completely immersed in water. The volume expansion ratio of the foamed sample, R_v, was defined as the ratio of the bulk density of the unfoamed sample (ρ_p) to that of the foamed one (ρ_f):

$$R_v = \rho_p / \rho_f \tag{2.7}$$

The relative density of the foamed sample, R_ρ, was defined as the ratio of the foamed sample (ρ_f) to that of the unfoamed one (ρ_p):

$$R_\rho = \rho_f \Big/ \rho_p \tag{2.8}$$

The average cell size was obtained through the analysis of the SEM photographs by the software Image-Pro Plus. The volume-average diameter of all the cells in the micrograph, D_{avg}, was calculated using the following equation:

$$D_{avg} = \left[\frac{\sum_{i=1}^{n} d_i^3}{n} \right]^{1/3} \tag{2.9}$$

where n is the number of cells, and d_i is the perimeter-equivalent diameter of each counted cell.

The cell density N_c on the fracture surface, defined as the number of cells per unit area of the foam on the cross section, was calculated by

$$N_c = \frac{nM^2}{A} \tag{2.10}$$

where n is the number of cells in the micrograph, A the area of the micrograph (cm^2), and M the magnification factor. Then the cell density N_f, defined as the number of cells per unit volume of the foam, was calculated by

$$N_f = \left(N_c\right)^{\frac{3}{2}} \tag{2.11}$$

A_f, the area fraction occupied by the voids on the cross section, was calculated by

$$A_f = \left(\frac{\pi}{4}\right) D_{avg}{}^2 N_c \tag{2.12}$$

Then, A_s, the area fraction of solid area on the cross section, was calculated by

$$A_s = \frac{1}{A_f} \tag{2.13}$$

V_f, the volume fraction occupied by the voids, was calculated by

$$V_f = \left(\frac{\pi}{6}\right) D_{avg}{}^3 N_f \tag{2.14}$$

The cell density N_0, defined as the number of cells per unit volume of the original (unfoamed) polymer, was calculated according to the following expression:

$$N_0 = N_f \times R_v \tag{2.15}$$

2.3.9 Solubility measurement

The apparent solubility of CO_2 in the iPP melts was measured directly using MSB as shown in Fig. 2.5 (Rubotherm Prazisionsmesstechnik GmbH, Germany). The MSB has an electronically controlled magnetic suspension coupling that transmits the weight of the sample in a pressure vessel to a microbalance outside of the cell. The MSB can be used at pressures up to 35 MPa and temperatures up to 523 K. Resolution and accuracy of the microbalance (Mettler AT261, Switzerland) are 0.01 mg and 0.002%, respectively. The system temperature and pressure can be controlled at the accuracy of ±0.2 ^oC and ±0.05 MPa, respectively. Details of the apparatus and experimental procedure used in this work have been described in previous publications [101, 102].

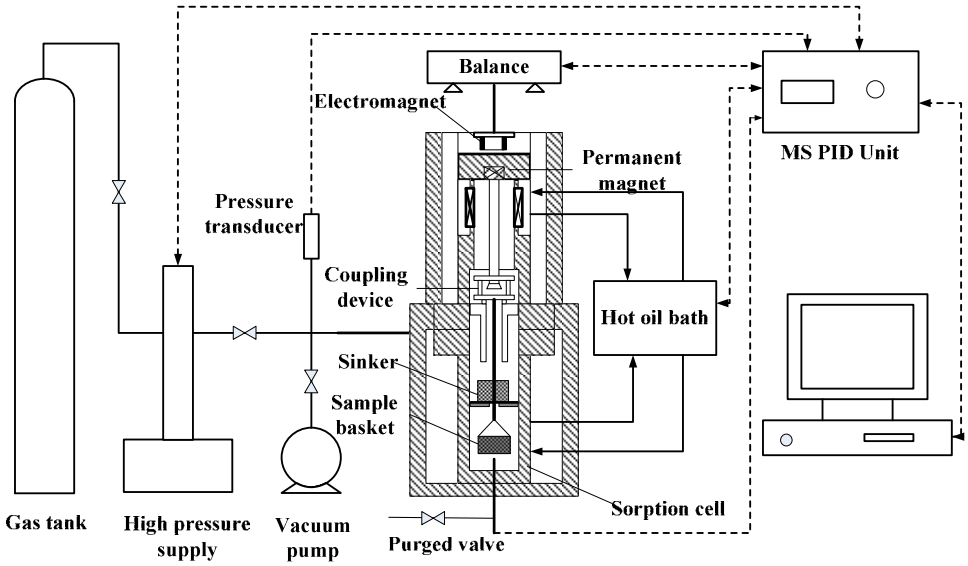

Fig. 2.5 The schematic diagram for sorption measurement by using magnetic suspension balance

Chapter 3 Carbon Dioxide Induced Crystallization for Toughening Polypropylene

3.1 Introduction

Isotactic polypropylene (iPP) has good comprehensive properties, such as easy processing, high heat resistance, and good stiffness, etc., and in turn is widely used as a commodity plastic [34]. However, under conventional processing conditions, iPP crystallizes into sizable spherulites with few tie molecules between spherulites. With such a crystalline texture, iPP exhibits very low impact toughness, especially at lower temperature, which restricts its more extensive application. Therefore, toughening of iPP has always been an open research.

Injection molding is one of the most widely employed processes for manufacturing polymer products and consists of three main steps: filling, packing/holding and cooling. Typically, multiple layers or a skin-core structure of iPP samples are formed during injection molding [35, 36, 38]. A shear zone with a high level of orientation is mainly responsible for shear-induced properties [35, 36]. Oriented crystals (i.e., shish-kebabs) can lead to significant improvement in tensile strength [69], modulus and stiffness [70]. However, the improvement in performances of polymers seems to be available only in the oriented direction [34-36]. In the perpendicular direction, the performances such as impact strength are often more or less reduced.

This work aims at improving the toughness of injection molded iPP specimens by controlling their crystal structure. This is done by three successive steps as depicted in Figure 3.1. The first step consists in controlling the degree of orientation of the crystal structure in the shear zone by tuning injection molding conditions (Figure 3.1a). Highly oriented crystals can significantly improve the tensile strength of the iPP samples. In the second step, the injection molded iPP specimens are subjected to re-crystallization in the solid state under sc-CO_2 (Figure 3.1b). Additional fine lamellae can be formed in the shear zone (see Figure 3.1b). They can improve the toughness of iPP samples while retaining the high tensile strength. The third step is to further tune the crystal structure by controlling the cooling rate of the sc-CO_2 treated injection molded iPP specimens. Non-isothermal crystallization of iPP at a fast cooling rate may yield nodular mesomorphic crystals in nano-size (see Figure 3.1c) [71]. These nano-size mesomorphic crystals in the shear zone would further improve the toughness of the sc-CO_2 treated injection molded iPP specimens. The originality of this work lies on these two last steps.

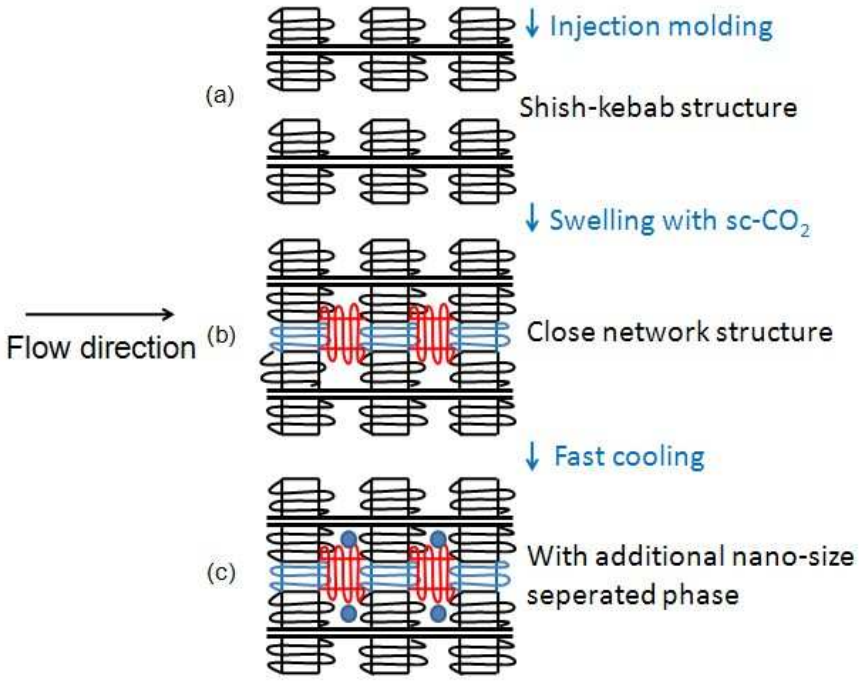

Figure 3.1 Schematic of crystal morphology development.

3.2 Effect of CO_2 treatment on the mechanical properties of iPP

Table 3.1 shows the iPP specimens used in this work. Compared with PP1 and PP2, the iPP samples after CO_2 treatment, namely, PP3 to PP6, exhibit superior toughness, as shown in Fig. 3.2a. The impact strength of PP2 is 6.1±0.2 KJ/m^2, which is slightly lower than that of PP1, 7.2±0.1 KJ/m^2, due to the higher orientation level of PP2 than that of PP1 along the flow direction. The impact strength of PP3 (10±0.1 KJ/m^2) and PP5 (43.6±0.1 KJ/m^2) is about 1.4 and 6 times that of PP1, respectively, while that of PP4 (18.5±0.2 KJ/m^2) and PP6 (75.7±0.2 KJ/m^2) is 3 and 12 times that of PP2, respectively. These results indicated that CO_2 treatment indeed toughened the iPP samples.

Table 3.1 iPP specimens used in this work

Sample	Preparation technique
PP1	Injection molded at the melt temperature of 200 ^{o}C, mold temperature of 100 ^{o}C and injection speed of 70%, and then annealed at the temperature of 110 ^{o}C for 5 h
PP2	Injection molded at the melt temperature of 180 ^{o}C, mold temperature of 40 ^{o}C and injection speed of 30%, and then annealed at the temperature of 110 ^{o}C for 5 h
PP3	PP1 annealed under $scCO_2$ (100 ^{o}C, 15 MPa, 5 h) followed by quenching in ambient water
PP4	PP2 annealed under $scCO_2$ (100 ^{o}C, 15 MPa, 5 h) followed by quenching in ambient water
PP5	PP1 annealed under $scCO_2$ (100 ^{o}C, 15 MPa, 5 h) followed by quenching in ice-water
PP6	PP2 annealed under $scCO_2$ (100 ^{o}C, 15 MPa, 5 h) followed by quenching in ice-water

Moreover, when subjected to the same annealing and subsequent quenching conditions, an iPP sample with more highly oriented crystals (PP2) exhibits a significantly higher toughness compared with an iPP sample with less oriented crystals (PP1). On the other hand, quenching in ice-water after annealing resulted in much higher toughness than in water. This is true for both highly and weakly oriented crystal samples. Therefore, the key process parameters to enhancing toughness are a high degree of orientation of crystals, adequate $scCO_2$ induced recrystallization in the solid state and fast cooling of $scCO_2$ treated samples. Fig. 3.2b compares PP6 with PP1 and PP2 in terms of tensile strength, elongation at break and tensile modulus. Because of higher crystal orientation, PP2 has higher tensile strength and modulus and a lower elongation at break than PP1. The elongation at break of PP2 after the CO_2 treatment (PP6) is significantly higher than that of PP2 while its tensile strength and modulus remain unchanged. This indicated that highly oriented iPP could be significantly toughened without loss in tensile strength and modulus by $scCO_2$ induced recrystallization and subsequent fast cooling in ice-water. Additionally, the elongation of the samples all leads to necking. Hereinafter, the morphology and structures of PP1-PP6 were investigated by using DSC, POM，FTIR, SEM, SAXS, and WAXD to better understand the structure-property relationship.

It should be noted that the volume of the iPP samples does not change much after the CO_2 swelling. As such, changes in geometry and density of the samples will be ignored in the subsequent discussion.

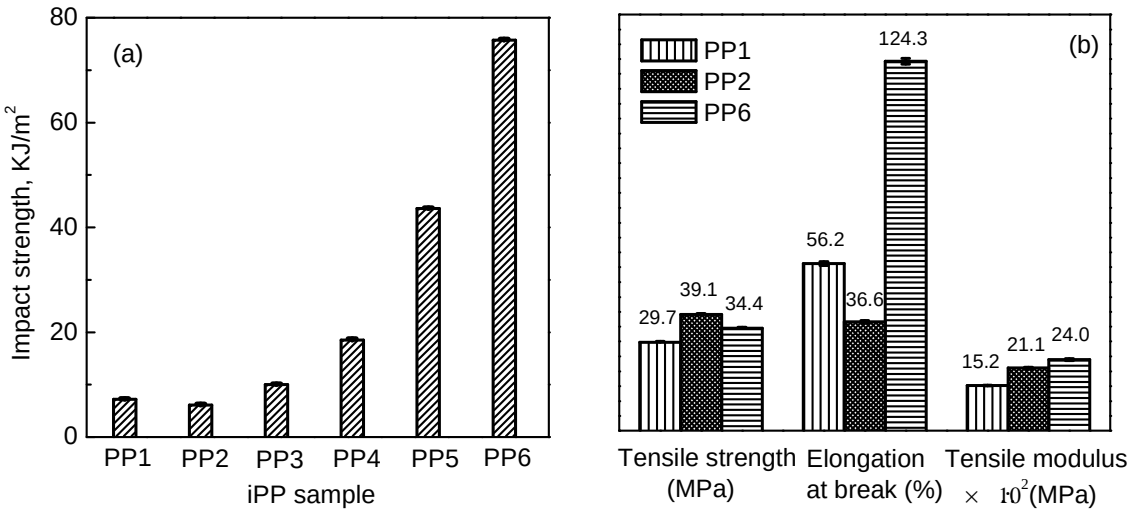

Fig.3.2 Comparison between iPP samples in terms of impact strength, tensile strength, elongation at break and tensile modulus.

3.3 Distribution of molecular orientation

Fig. 3.3 and Fig.3.4 show the polarized optical micrographs of the cross-sections of PP1 and PP2. Fig. 3.3 reveals a typical morphological pattern of an injection molded semi-crystalline sample, i.e., a skin layer, an intermediate layer and a core layer. Fig. 3.4 shows the morphologies of different zones (zones A, B and C) in Fig. 3.3 at higher magnification. The obvious striped birefringence and colorful interference in zone A indicated the oriented and closely crystalline structure. In zone B, the interference color of PP1 becomes light while that of PP2 is still deep. It indicated that the higher orientation and more closely crystalline structure of PP2 were than those of PP1. Especially in zone C, PP2 still exhibits the slight orientation while PP1 is isotropic spherulites. Thus, the orientation level of PP2 at all positions (from zone A to zone C) was significantly higher than that of PP1, and PP2 had more closely structure. The orientation degree of PP1-PP6, in both flow direction and perpendicular direction, would be discussed in detail in the following section.

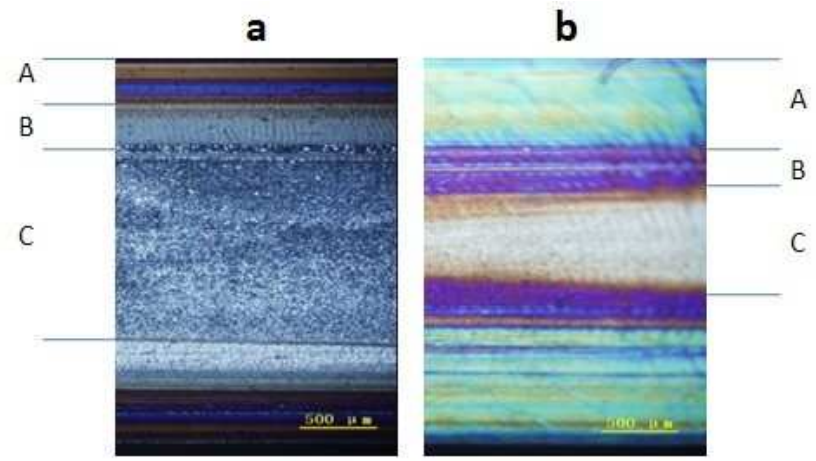

Fig. 3.3 Polarized optical micrographs of the cross-sections of the injection molded iPP samples at lower magnification: (a) PP1; (b) PP2. Distinct layers are: A: skin layer; B: intermediate layer and C: core layer.

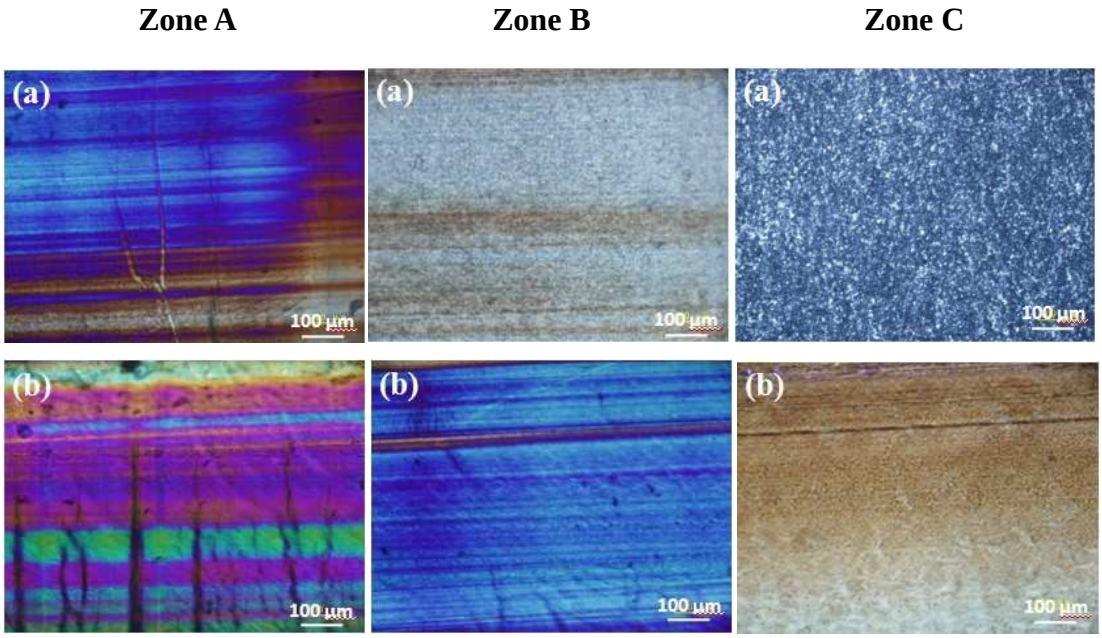

Fig. 3.4 Polarized optical micrographs of the cross-sections of the injection molded iPP samples at higher magnification: (a) PP1 and (b) PP2. The images were obtained from the different zones as shown in Fig.3.4.

Fig. 3.5 shows the degree of orientation in both flow and perpendicular directions for PP1-PP6 at different positions from the skin to the core. The degree of orientation was indeed higher for PP2 than that for PP1 in all layers. The highest degree of orientation was, as expected, in the skin layer. Fig. 3.5a-b also shows that the CO_2 treatment alters slightly the orientation of the iPP in flow direction. However, the change is obvious in perpendicular direction after CO_2 treatment as shown in Fig. 3.5c-d. Moreover, compared PP1 with PP3 and PP5, it was found that the increase of orientation degree in perpendicular

direction was slight from the distance of about 800 μm to the core, both for the crystalline phase and the amorphous phase. There was a similar phenomenon compared PP2 with PP4 and PP6. It seemed that the orientation degree in perpendicular direction after CO_2-induced recrystallization would increase only when the highly oriented crystal existed. The slight change of orientation in flow direction might be due to the existence of the highly oriented crystalline phase. It was consistent with our assumption in Fig. 3.1b. However, it did not mean that the CO_2 treatment had no effect on the isotropic zone.

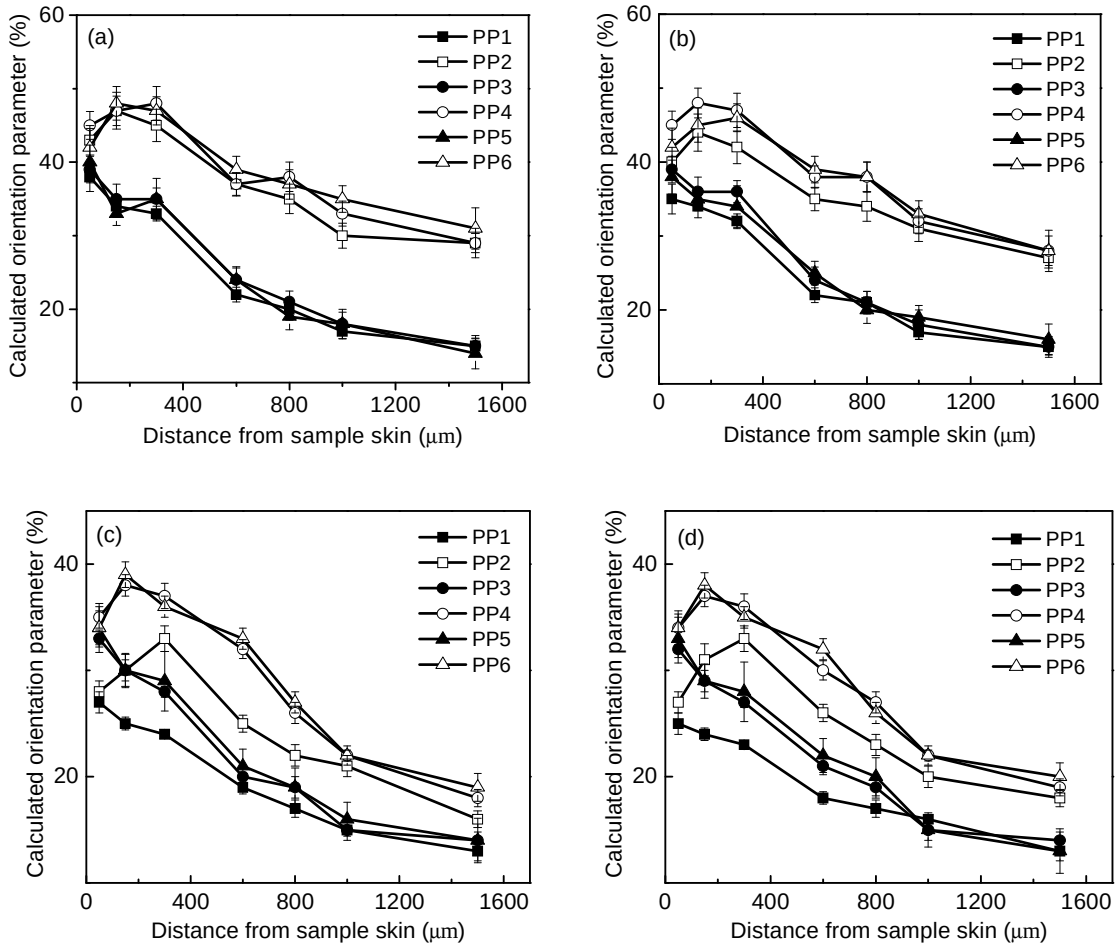

Fig.3.5 Orientation distribution along the thickness determined by IR spectra for iPP. (a) crystalline phase in flow direction, (b) amorphous phase in flow direction, (c) crystalline phase in perpendicular direction and (d) amorphous phase in perpendicular direction, respectively. The lines only indicate the trend.

3.3.1 Thermal properties

It is stated above that a highly oriented crystal structure is a prerequisite for the formation of an interconnected network structure. The result of the POM confirmed the formation of such an oriented structure in the skin layer of the iPP samples, and the result of FTIR

revealed the change of both crystal and amorphous phases after CO_2 treatment. Fig. 3.6a-c shows the DSC thermograms of PP1-PP6 samples in the skin layer, the intermediate layer and the core layer, respectively. The percentages of crystallinity are also shown in the patterns. Comparing Fig. 3.6a with Fig. 3.6b-c, the DSC traces of PP1 and PP2 in skin layer show two obvious endothermic peaks corresponding to lamellar and stretched crystals, respectively. Even after CO_2 treatment, the two endothermic peaks still exist as shown in Fig. 3.6a. On the other hand, after the CO_2 treatment the corresponding samples (PP3-PP6) show higher degrees of crystallinity and their main melting peaks are higher and broader than those of PP1 or PP2. Moreover, a very broad endotherm peak has appeared between 100 and 130^{o}C. It is well-known that a broad melting peak is attributed to a broad distribution of the lamellar thickness due to crosshatched structures consisting of thick primary lamellae with a higher melting temperature and thin subsidiary lamellae with a lower melting temperature [72-74]. Therefore, an increase in the number of lamellae, especially for the subsidiary lamellae perpendicular to the primary lamellae, was supposed to be the reason of the broader peak. In other words, $scCO_2$ induced recrystallization might allow developing a crystalline network like the one depicted in Fig. 3.1 as a result of an increase in the number of the primary lamellae and that of the crosshatched subsidiary lamellae. In addition, there is not much difference in terms of the DSC traces between PP4 and PP6 (or PP3 and PP5). Nevertheless the difference is big in terms of the impact strength between them as a result of the difference in the cooling rate.

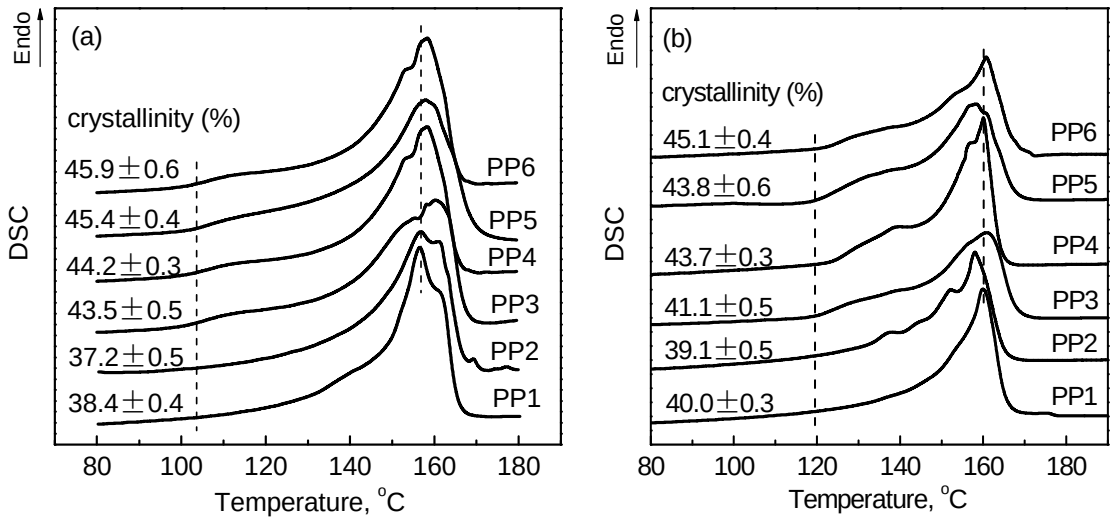

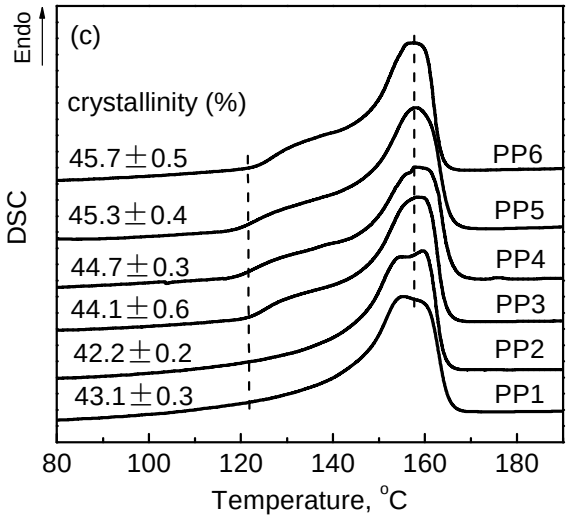

Fig. 3.6 DSC thermograms of PP1-PP6 in (a) the skin layer, (b) the intermediate layer and (c) the core layer, respectively.

3.3.2 Crystalline phase morphology in the Skin layer

Fig. 3.7 shows SAXS patterns of both PP1 and PP2 before and after annealing under CO_2. The flow direction of samples is shown in Fig. 3.7, and the measurement direction is vertical. Typically, the equatorial streak in SAXS pattern is attributed to the formation of an oriented structure or shish parallel to the flow direction. The meridional maxima are attributed to the layer-like oriented structure or kebab perpendicular to the flow direction.[42] Compared with Fig. 3.7c, Fig. 3.7a had stronger reflections along the equator which indicates the higher orientation of PP2 than PP1. The significant increase in the meridional maxima of PP2 after CO_2 treatment indicated that the CO_2 treatment had brought about a significant increase in the kebab (perpendicular to the flow direction). On the other hand, the change in meridional maxima of PP1 was not obvious, compared with PP2. It was consistent with the FTIR results that the orientation degree in perpendicular direction after CO_2-induced recrystallization would increase only when the highly oriented crystal existed. In addition, the strong scattered intensity of Fig. 3.7b due to the increase in crystallinity further corroborated the above statement that the annealing under CO_2 induced iPP to recrystallize. As a result, the initially formed oriented and un-oriented crystals grew in size and went to perfection. Moreover, Fig. 3.7b shows strong diffused scattering indicative of the un-oriented crystals, which corroborates the foregoing DSC result that a broad endotherm between 100 and 130 ^{o}C represents the kebabs or the perpendicular direction oriented components, in addition to the main skeleton of the shish-kebab structure that is generated during the CO_2 annealing.

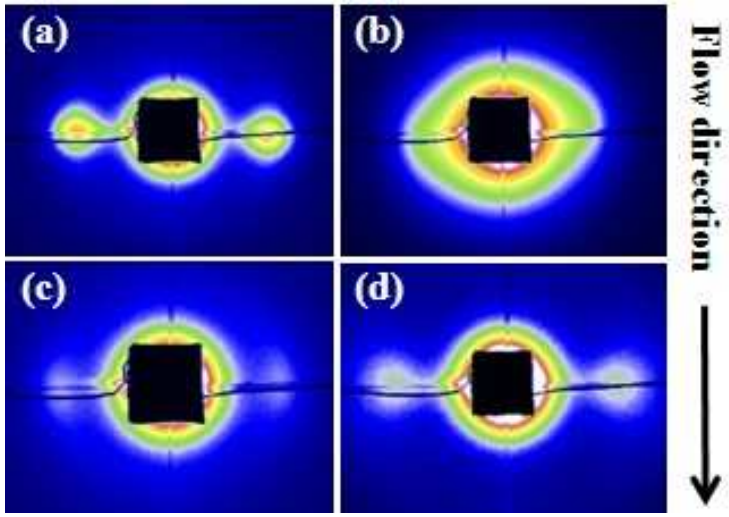

Fig. 3.7 2D SAXS images of (a) PP2 before CO_2 treatment, (b) PP2 after CO_2 treatment, (c) PP1 before CO_2 treatment and (d) PP1 after CO_2 treatment.

It is common practice to observe crystal structures of polyolefins such as iPP by etching or pigmentation. However it is not always easy to obtain distinct images. A previous work showed that foaming in the solid state could be a good alternative to observe the crystal structure of a semi-crystalline polymer in an indirect manner. The amorphous regions would foam while the crystalline ones would remain intact [42]. To observe the crystal morphology of PP2 and PP6, the samples were foamed at 145^{o}C and a CO_2 saturation pressure of 15 MPa. A certain proportion of crystals can be molten under these conditions. Fig. 3.8 shows the SEM photographs of PP2 and PP6 foams in the skin layer. It confirmed the formation of the crystal network structure as a result of the CO_2 induced crystallization in which the ‘shishes’ and ‘kebabs’ were connected with each other. The closely connected shish-kebab lamellar crystals improved the strength perpendicular to the orientation direction. Moreover, the existence of crosshatched subsidiary crystals among the primary lamellae led to more uniform distribution of the rigid crystalline phase domains in the soft amorphous phase ones. These unique nano-size structures could promote the absorption of the impact energy perpendicular to the orientation direction and hence enhance the toughness of the samples.

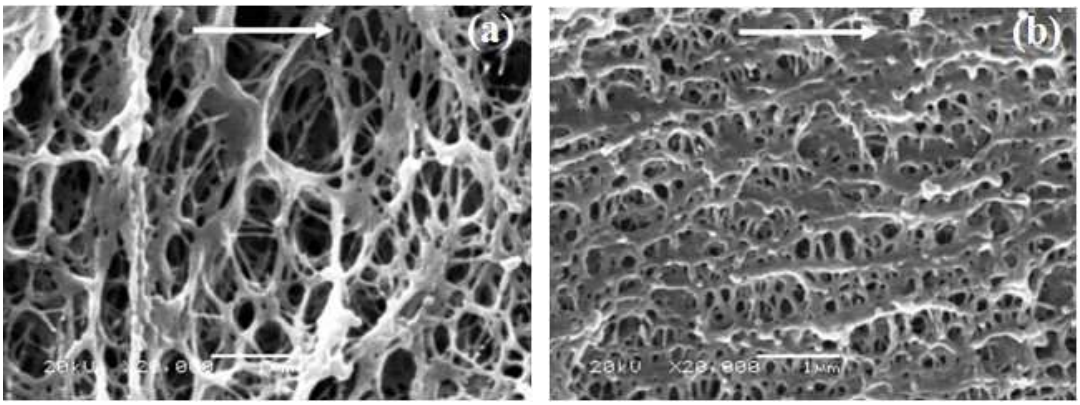

Fig. 3.8 SEM photographs of iPP samples in the shear zone foamed at 145 ^{o}C and a CO_2 saturation pressure of 15 MPa. (a): PP2; (b): PP6. White bars in (a) and (b) are 1 μm. The arrows indicate the flow direction.

3.3.3 Impact-fractured surface morphologies

Study on the impact-fractured surface morphology is favorable to understanding the toughening mechanism of PP samples. Fig. 3.9 and Fig. 3.10 show the representative impact-fractured surface morphologies of PP1-PP6. It is well known that the fracture process of the specimen under the load of impact includes at least two steps, i.e., crack initiation and crack propagation processed. Thus, to provide more detail information about the impact fracture process of the specimen, the overall impact-fractured surface is sub-classified as crack initiation zone (zone A), the early stage of crack propagation zone (zone B) and the later stage of crack propagation zone (zone C) as shown in Figure 10a according to the methodology developed by Misra and coworkers [75, 76]. An interesting characteristic feature of the fracture surface of PP before CO_2 treatment (PP1 and PP2) is that a rough surface observed in crack initiation zone (zone A) following with a flat and smooth surface in crack propagation zone (zones B and C). It indicated that the strain energy absorption mainly occurred in the crack initiation zone, leading to the rapid breakdown of the crack propagation zone. Furthermore, one can observe a small zone with a parabolic ridge or a thin curved band at relatively lower magnification (Fig. 3.9a), relating to the change in the stress state. For PP3-PP4, the typical morphology of brittle-fracture mode is observed without any considerable plastic deformation of matrix. Moreover, the fractured surface in crack propagation zone (zones B and C) becomes coarser and some microvoids (see Fig. 3.10c-d) can be observed from the impact-fractured surface due to the interconnected network crystalline structure after CO_2 treatment. This observation agreed well with the enhancement of the impact strength as shown in Fig. 3.2. Especially, for PP5-PP6, completely different surface morphologies were observed in comparison with

those of PP1-PP4. First, an obvious plastic deformation appeared in the later crack propagation zone (zone C in Fig. 3.19e-f). Second, one can notice that the samples are not fractured completely due to the relatively higher fracture resistance as shown in Fig. 3.2. PP6 exhibits a larger non-fractured part (see the rectangular zone in dash lines in Fig. 3.9) compared with PP5, suggesting the higher fracture resistance of PP6. In the later stage of the crack propagation process (zone C in Fig. 3.10e-f), one can observe the local deformation of the matrix and the formation of a large amount of striations which perpendicular to the crack propagation direction. These plastic deformation zones absorbed large impact energy during the fracture process and made sample more ductile [77]. It was attributed to the more uniform distribution of the rigid crystalline phase domains in the soft amorphous phase ones after the third step as shown in Fig. 3.2c. In other words, the crack propagation resistance was dramatically improved with the interconnected network crystalline structure and the uniform distribution of crystal and amorphous phases after CO_2 treatment of oriented iPP specimen.

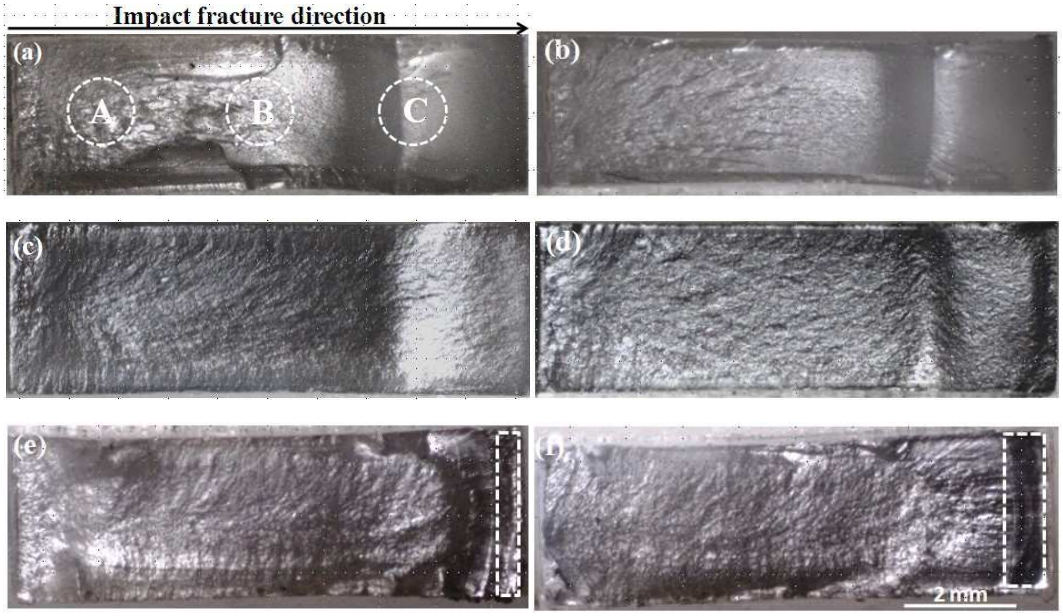

Fig.3.9 SEM images of the impact-fractured surface of PP1-PP6 at lower magnification. (a) PP1, (b) PP2, (c) PP3, (d) PP4, (e) PP5 and (f) PP6. A, B and C indicate the crack initiation zone, the crack propagation zone and the later stage of the crack propagation, respectively. The rectangular zone shown by dash lines represents the non-fractured part of the specimen during the impact fracture process.

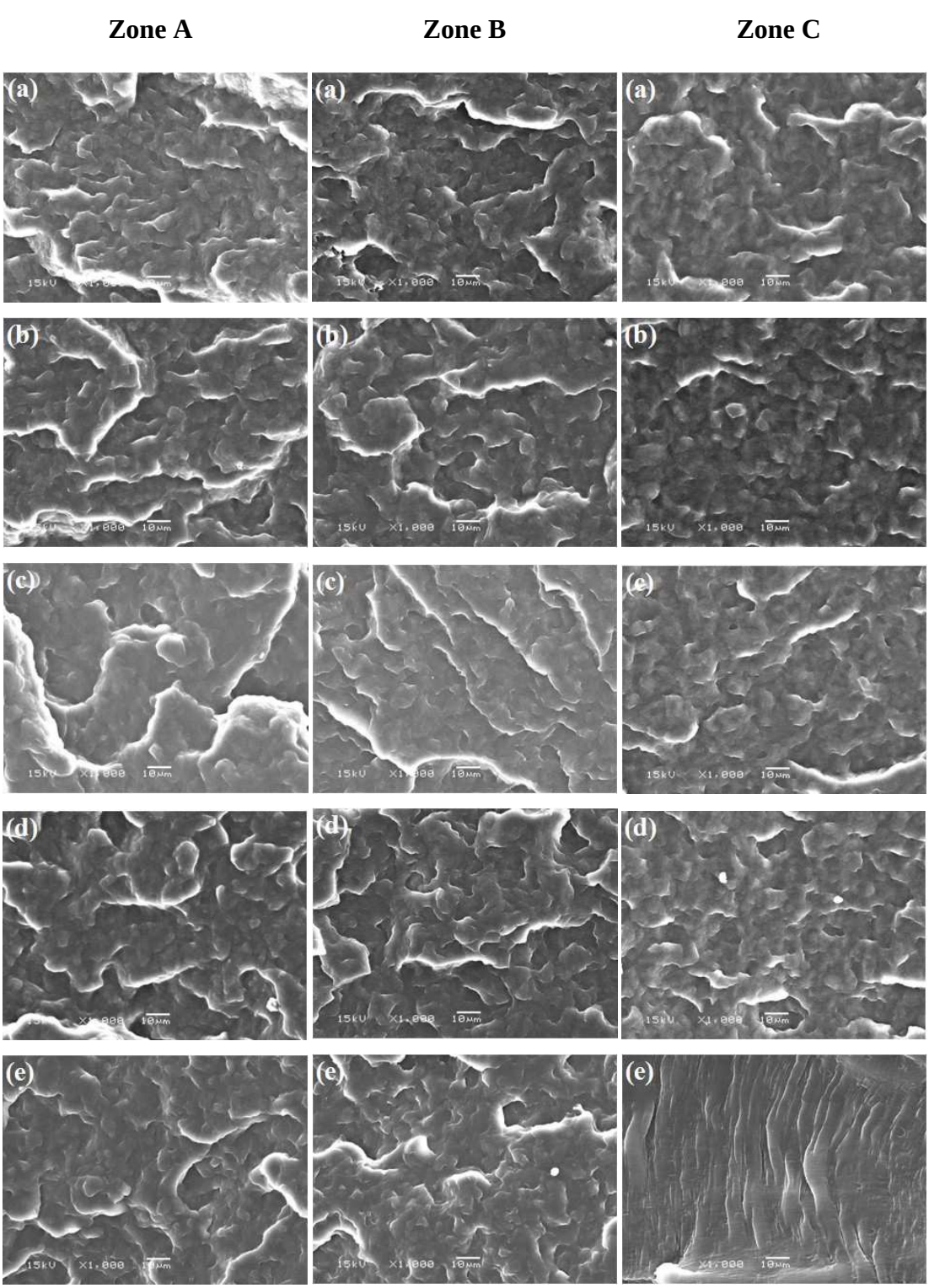
Zone A
Zone B
Zone C
(a)
(b)
(c)
(d)
(e)

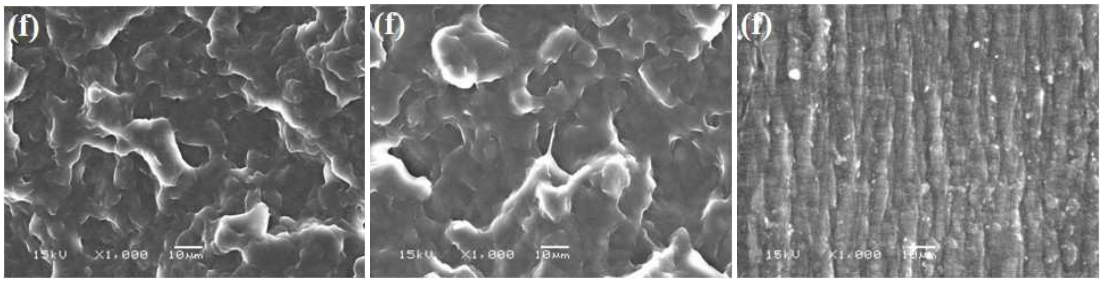

Fig.3.10 SEM images of the impact-fractured surface of PP1-PP6 at higher magnification. The images were obtained from the different zones as shown in Figure 10. (a) PP1, (b) PP2, (c) PP3, (d) PP4, (e) PP5 and (f) PP6.

3.4 Effect of quench on the crystal structure

It was stated above that the increased number of lamellar crystals as a result of $scCO_2$ induced recrystallization was a reason for improved toughness of the iPP samples (PP2 versus PP4). The cooling stage that follows the $scCO_2$ treatment is another important reason for the improvement in toughness (PP4 versus PP6). What structural changes have occurred during the cooling stage? Fig. 3.11 depicts the WAXD patterns of PP1- PP6 in skin layer as shown in fig. 3.3. The WAXD patterns of PP1 and PP2 exhibit five major peaks. They are located at 14.1, 16.1, 16.9, 18.6 and 20.3^o, corresponding to the diffraction of crystal reflections from planes α(110), β(300), α(040), α(130) and γ(117), respectively. The percentages of crystallinity are shown in the patterns. For PP1 and PP2, there is no obvious peak at the region from 20 to 22^o, due possibly to the high degree of orientation in the skin layer. It is interesting that the amounts of β-crystals and γ-crystals in PP1 are significantly higher than those in PP2. Normally, shear can induce crystallization leading to β and γ crystals [78, 79]. However, very high shear may prevent β and γ crystals from forming [34]. This is because shear accelerates the nucleation and growth of α-row nuclei which tend to induce the formation of α-crystals rather than β and γ crystals. In other words, the shear rate for PP1 in the injection molding process would be able to promote the formation of β and γ crystals whereas it would be too high in the case of PP2.

On the other hand, the WAXD pattern of PP3 or PP4 is not different from that of PP1 or PP2. That of PP6 shows that the crystallinity of the β-form crystal has decreased, the γ-form peak has disappeared and a new peak at 21.8^o has appeared. This indicated that under the $scCO_2$ then quenching in ice-water, β and γ-form crystals were transformed to α-form ones while a new type of crystal might be formed. It has been reported that when iPP is quenched from melt to low temperature, an intermediate phase named mesomorphic phase can be formed [80-82]. The WAXD pattern of the mesomorphic phase exhibits only two peaks

at about 14.8 and 21.8°. Thus, during the cooling process in an ice-water bath, the iPP that has already been subjected to $scCO_2$ treatment might produce mesomorphic phase domains of several dozens of nanometers in size. The nano-size phase domains distributed in the existing crystalline network structure significantly enhances the impact strength.

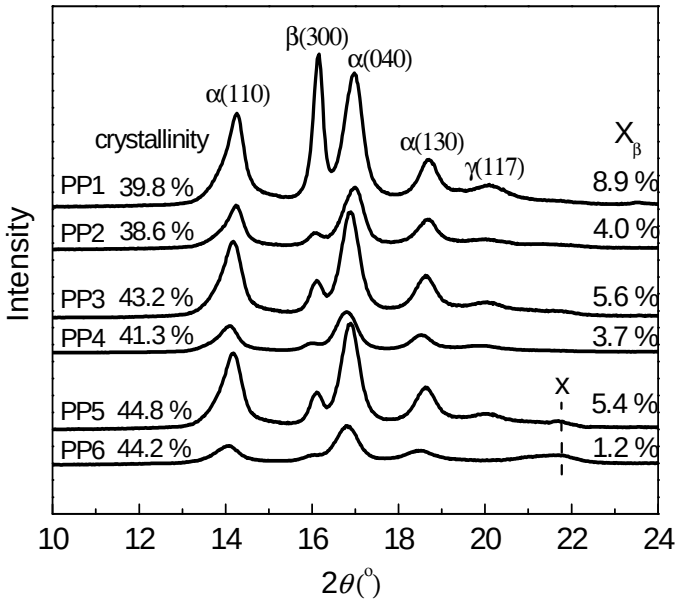

Fig.3.11 WAXD profiles of iPP samples.

3.4.1 Effect of the instability of nano-size mesomorphic phase

It is well-known that the mesomorphic phase is unstable. Chains in the mesomorphic phase domains may re-organize or 'melt' at an elevated temperature and are transformed to α-monoclinic phase [82]. PP6 was re-annealed in a vacuum oven for 5 hours at 30, 40, 50, or 80°C. Fig. 3.12a and b show the effect of this re-annealing on the impact strength and WAXD pattern, respectively. From Fig. 3.12b, the areas of all the reflection peaks normalized by the one at 21.8 ° decrease with increasing re-annealing temperature. The impact strength decreases accordingly. The impact strength of PP6 is 75.7 kJ/m^2 and is reduced to 18 kJ/m^2 when it is re-annealed at 80°C for 5 hours during which the mesomorphic phase domains have almost completely disappeared (no reflection peak at 21.8°). This value is close to that of PP4, as expected. The above results further confirm the formation of the mesomorphic phase of the $scCO_2$ treated iPP during quenching in ice-water.

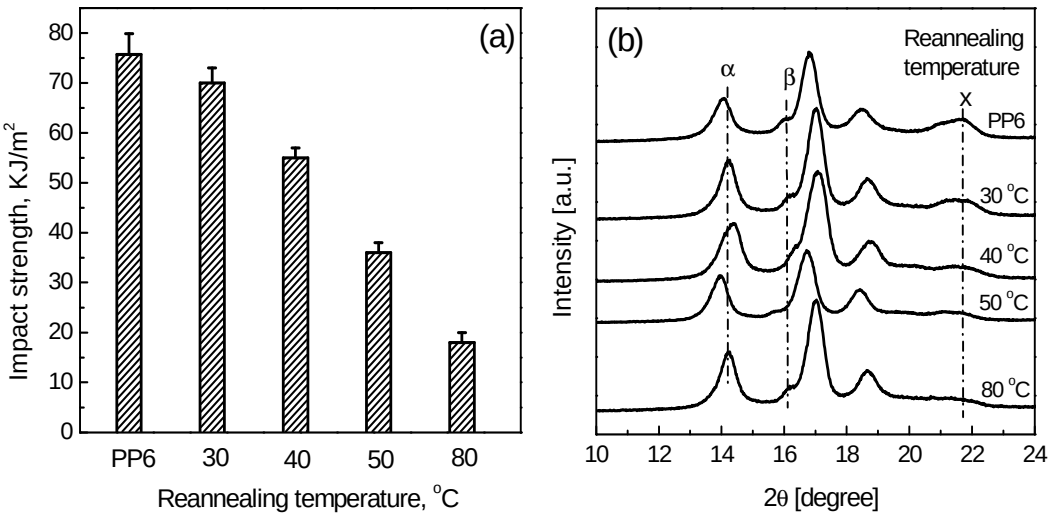

Fig.3.12 Impact strength (a) and WAXD pattern (b) of PP6 after re-annealing for 5 hours at various temperatures: 30, 40, 50, and 80 °C, respectively.

3.5 Effect of CO_2 pressure and temperature

According to the above statement, the toughness of injection molded iPP specimens can be significantly improved by controlled shearing, CO_2 induced re-crystallization and adequate cooling without loss of strength. Under shear, a high degree of orientation can be obtained with "shish-kebab" crystals formed in the shear zone. During the subsequent CO_2 treatment, a crystal network morphology may be formed as a result of an increase in the number of the primary lamellae and that of crosshatched subsidiary lamellae, which leads to an increase in the toughness. In addition, quenching in ice-water of $scCO_2$ treated iPP promotes the formation of nano-sized mesomorphic phase domains in the shear zone, which further toughens the iPP. However, the mesomorphic phase generated by quenching in ice-water is unstable. When re-annealed at 80°C for 5 hours, the impact strength of PP6 is reduced to 18 kJ/m^2, which is close to that of PP4. In other words, the second step of toughening is more available for application. In this section, we systematically study the effect of CO_2 pressure and temperature on the final crystalline structure and the corresponding mechanical properties during the second step.

Fig. 3.13a shows the impact strength of PP2 treated under 100°C and various CO_2 pressures. It indicates that the impact strength of the treated samples increases with the pressure increasing from 10 to 15MPa when saturation temperature is 100°C. However, when the CO_2 pressure is higher than 15MPa, the impact strength of PP2 treated samples is unchanged. Fig. 3.14 shows the DSC thermograms of these treated samples. The crystallinities of iPP samples increase with the CO_2 pressure increase until 15MPa, which is consistent with the change of impact strength. As we stated above that during the CO_2

treatment, a crystal network morphology may be formed as a result of an increase in the number of the primary lamellae and that of crosshatched subsidiary lamellae, which leads to an increase in the toughness. It is well-known that the dissolution of CO_2 in the polymer increases the free volume between molecular chains and chain mobility, and consequently affects its crystallization behavior. In addition, the solubility of CO_2 in iPP matrix increases with CO_2 pressure increase. Therefore, it indicates that the CO_2 induced-crystallization is promoted by the increase of CO_2 pressure until 15MPa.

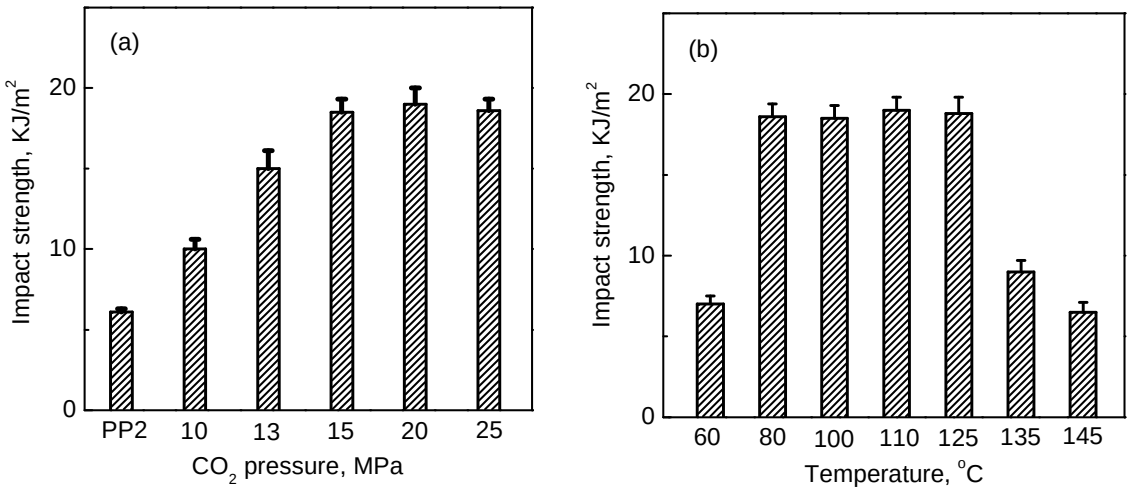

Fig. 3.13 Impact strength of PP2 treated under (a) 100°C and various CO_2 pressures; and (b) 15MPa and various temperatures.

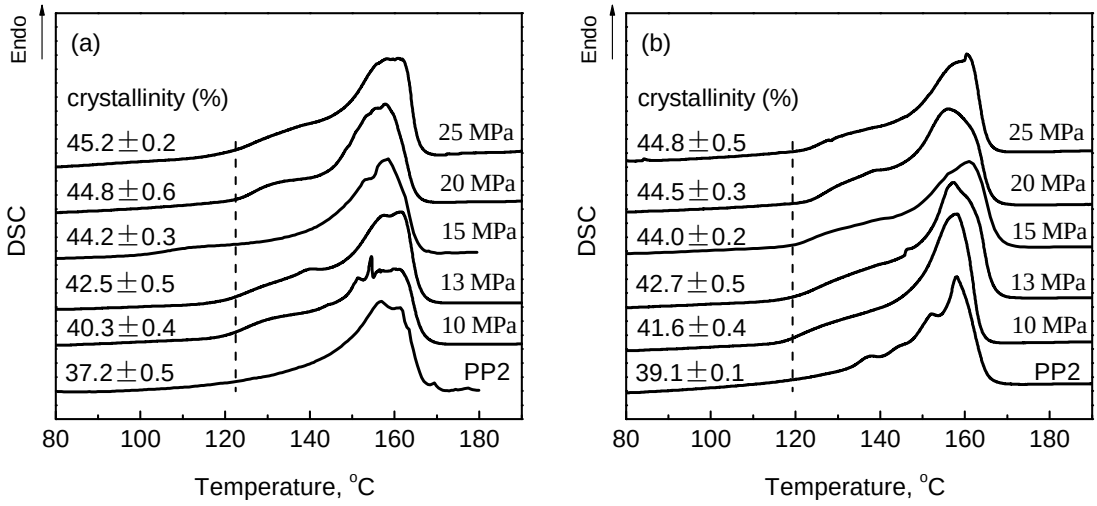

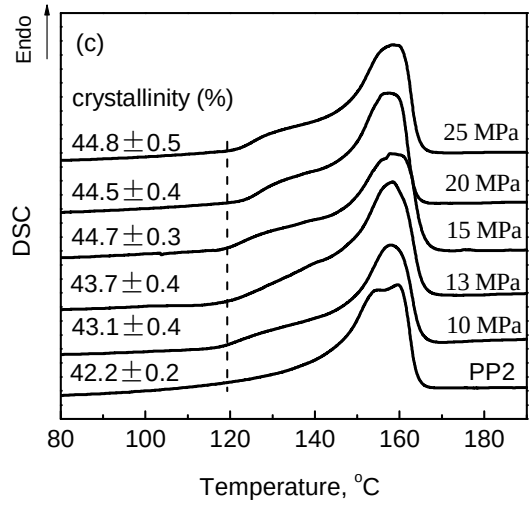

Fig. 3.14 DSC thermograms of PP2 treated under 100°C and various CO_2 pressures (0, 10, 13, 15, 20, 25MPa), in (a) the skin layer, (b) the intermediate layer and (c) the core layer, respectively.

Fig. 3.13b shows the impact strength of PP2 treated under 15MPa and various temperatures and Fig. 3.15 shows the DSC thermograms of these treated samples. When the saturation temperature is 60°C, the CO_2 induced crystallization is not obvious, and the corresponding impact strength of the treated sample is slightly higher than original one. When the saturation temperature is in the range of 80 to 125°C, the impact strength of the treated samples is three times the original one. With the saturation temperature further increasing (135°C), the impact strength suddenly decreases. Especially for the temperature of 145°C, the impact strength of the treated sample is similar with the original one. From Fig. 3.15, the melting peaks of samples treated at 135 and 145°C are both shifted to higher temperatures. The starting melting temperatures increase with saturation temperature increasing from 135 to 145°C, as demarcated by the arrows. The large increase in the melting temperature shows that after the annealing with $scCO_2$, the primary lamellae are significantly thickened. Meanwhile, the increase in the starting melting temperature and the decrease in the crystallinity indicate that part of the thin lamellae melt during the annealing process. That is why the impact strength of the treated samples decrease with saturation temperature increasing from 135 to 145°C.

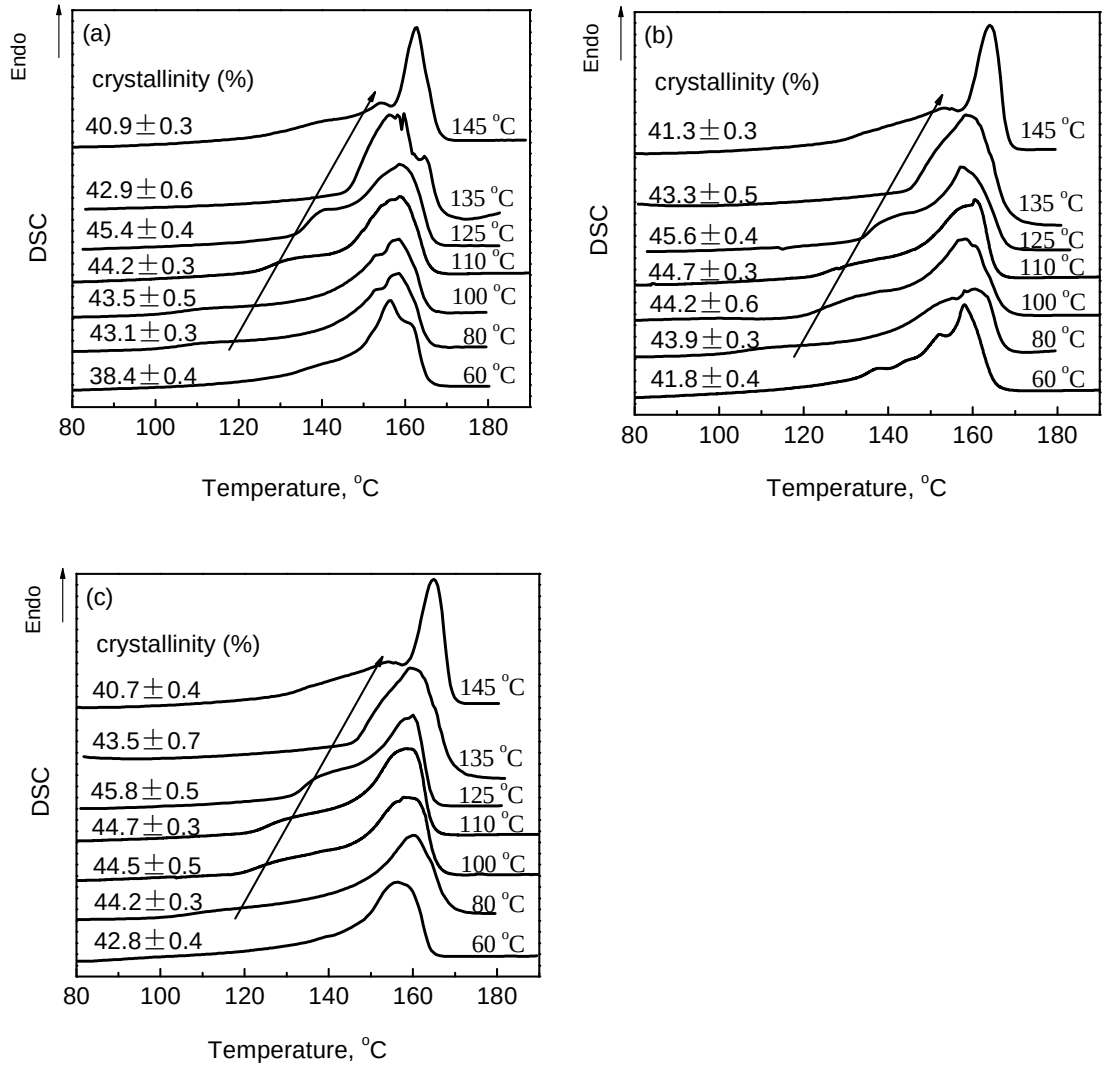

Fig. 3.15 DSC thermograms of PP2 treated under 15MPa CO_2 pressure and various temperature (60, 80, 100, 110, 125, 135, 145^oC), in (a) the skin layer, (b) the intermediate layer and (c) the core layer, respectively.

According to the above statement, when the temperature is in the range of 80 to 125^oC and the CO_2 pressure is higher than 15MPa, the iPP samples will be toughening completely by scCO_2 annealing. When the temperature is higher than 125^oC, part of the existed crystals are molten, leading to the poor performance. On the other hand, when the temperature is lower than 80^oC, and the CO_2 pressure is less than 15MPa, the CO_2 induced-crystallization is not complete. Fig. 3.16 shows the solubility of CO_2 in solid-state PP at various temperatures and pressures. The solubility increases with the pressure increase, and decreases with the temperature increase. The dissolution of CO_2 in the polymer increases the free volume between molecular chains and chain mobility. To a certain extent, the chain mobility increases with the solubility increase. In addition, the chain mobility increases with the temperature. This can explain why the temperature should be in the range of 80 to

125°C, and the CO_2 pressure should be higher than 15MPa, for the completely toughening of iPP by $scCO_2$.

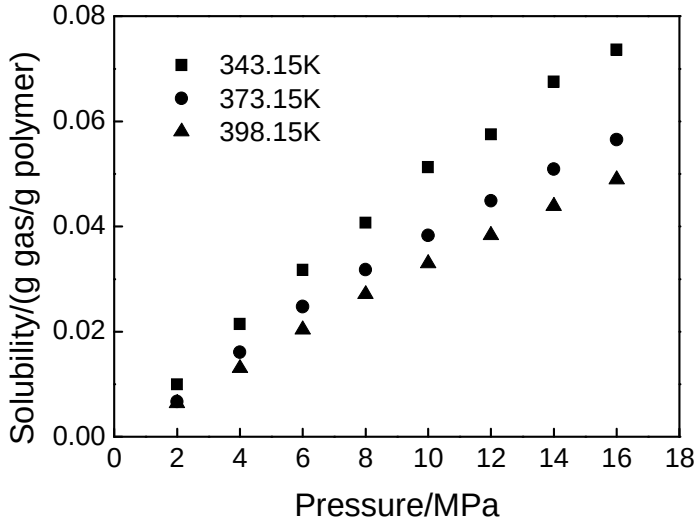

Fig. 3.16 Solubility of CO_2 in solid-state PP at various temperatures and pressures.

3.6 Conclusion

This study proposes a novel process for significantly toughening isotactic polypropylene by finely tuning and controlling the structure and morphology of iPP. More specifically, the toughness of injection molded iPP specimens can be significantly improved by controlled shearing, CO_2 induced recrystallization and adequate cooling without loss of strength. Under shear, a high degree of orientation can be obtained with “shish-kebab” crystals formed in the shear zone. During the subsequent CO_2 treatment, a crystal network morphology may be formed as a result of an increase in the number of the primary lamellae and that of crosshatched subsidiary lamellae. The 2D SAXS images and the SEM micrographs of the iPP foamed in the solid state confirm the formation of the crystal network structure in the shear zone in which the ‘shishes’ and ‘kebabs’ may be connected with each other. WAXD patterns indicate that quenching in ice-water of $scCO_2$ treated iPP promotes the formation of nano-sized mesomorphic phase domains in the shear zone, which further toughens the iPP. The impact strength of the best toughened iPP is over 12 times that of the original one without loss in tensile strength and modulus.

Chapter 4 Carbon Dioxide Induced Foaming of Highly Oriented Isotactic Polypropylene

4.1 Introduction

In a conventional supercrical carbon dioxide ($scCO_2$) batch foaming process, CO_2 is dissolved in a polymer matrix and is depressurized quickly to induce foaming in the polymer matrix. This type of process normally produces microcellular foams with average cell sizes of about 10 μm and a cell density of more than 10^9 cells/cm^3 [83-85]. In the past decade, efforts have been made to investigate the influence of processing conditions and the nature of polymers on the final cell morphologies of polymer foams. Many studies have focused on creating high-performance polymer foams by increasing the number of cells and decreasing cell size [86-88].

Recently, Li et al., [50] Yokoyama et al., [48] and Taki et al. [92] reported on the preparation of a CO_2 foamed thin film with nano size cells using a diblock copolymer as a tamplating material. The basic concept of their nanocellular foaming was to use the block copolymer possessing nano-scale and ordered spherical morphology as a template for bubble nucleation and growth. In other words, during the foaming process, cell nucleation and growth only occurred in the confined soft nano-scale domains while the surrounding un-foamed rigid domains did not foam.

This work aims at preparing a nanocellular foam with a highly oriented isotactic polypropylene (iPP). In the case of a solid-state foaming process, the crystal structure of the iPP may have a great effect on the cell formation and cell morphology, as cell nucleation and growth only occur in amorphous regions where CO_2 is dissolved [42]. It is well-known that the so-called shish-kebab structure consists of a long central fiber core (shish) surrounded by lamellar crystalline structure (kebab) periodically attached along the shish, is formed when iPP is crystallized under flow [40, 43, 44]. In other words, the amorphous domains among the crystal domains are confined in nanometer scale by the shish-kebab crystalline structure. On the other hand, according to the conclusion of chapter 3, CO_2 induced crystallization leads to the formation of crystal network structure in the shear zone as a result of an increase in the number of the primary lamellae and that of crosshatched subsidiary lamellae, in which the ‘shishes’ and ‘kebabs’ may be connected with each other. Therefore, it is expected that the use of a highly oriented iPP with a shish-kebab crystalline structure as a template may lead to nanocellular morphology by CO_2 foaming. Furthermore, with the formation of the nanocellular bubbles surrounded by

amorphous among the crystal network structure is expected to further toughen the iPP samples.

This is done by the following successive steps, as depicted in Fig. 4.1. The first one consists in preparing the shish-kebab crystalline structure in the shear zone by tuning injection molding conditions (Fig. 4.1a). In the second step, the highly oriented iPP specimens with the nanoscale shish-kekab crystalline structure are foamed with sc-CO_2 under the temperature and CO_2 pressure that they remain in the solid state. Constrained by the surrounding crystal domains which cannot foam, the cell nucleation and growth only proceed in the nanoscale amorphous domains (Fig. 4.1b).

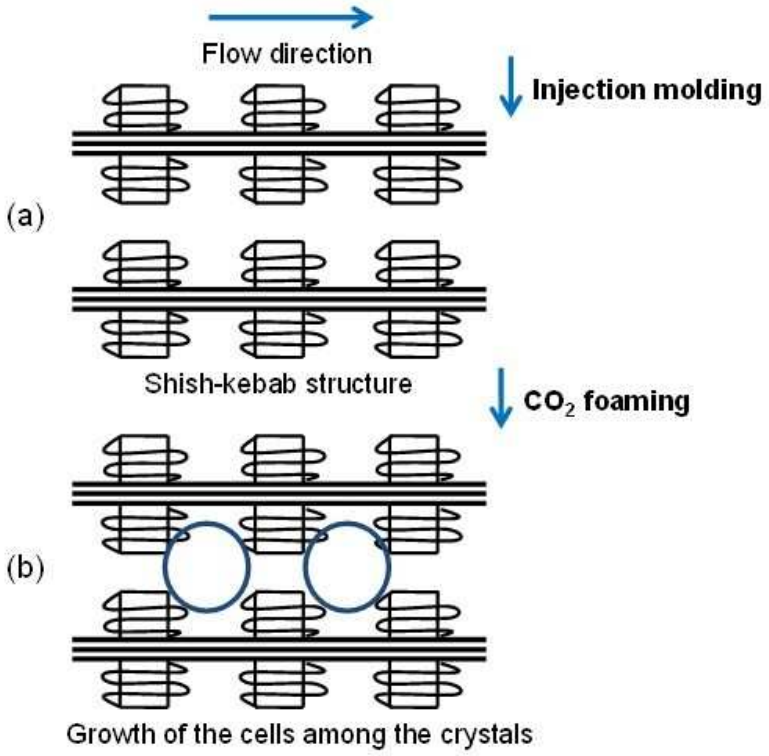

Fig. 4.1 Schematic of the cell nucleation and growth in amorphous domains constrained by the shish-kebab crystalline structure.

4.2 Crystalline structure of injection molded iPP

Fig. 4.2a shows the optical micrographs of the cross-section of an injection-molded iPP sample before foaming. They reveal a typical morphological pattern of an injection molded semi-crystalline sample, i.e., a shear layer, an intermediate layer and a core layer, as expected. Fig. 4.2b-d shows the morphologies of three different zones (A, B and C) in Figure 4.2a at higher magnifications. The obvious birefringence strips and interference colors in zone A (Fig. 4.2b) correspond to an oriented and closely packed crystalline

structure. The morphologies in zones A, B and C (Fig. 4.2b-d) show that the degree of orientation gradually decreases with the distance from the skin to the core.

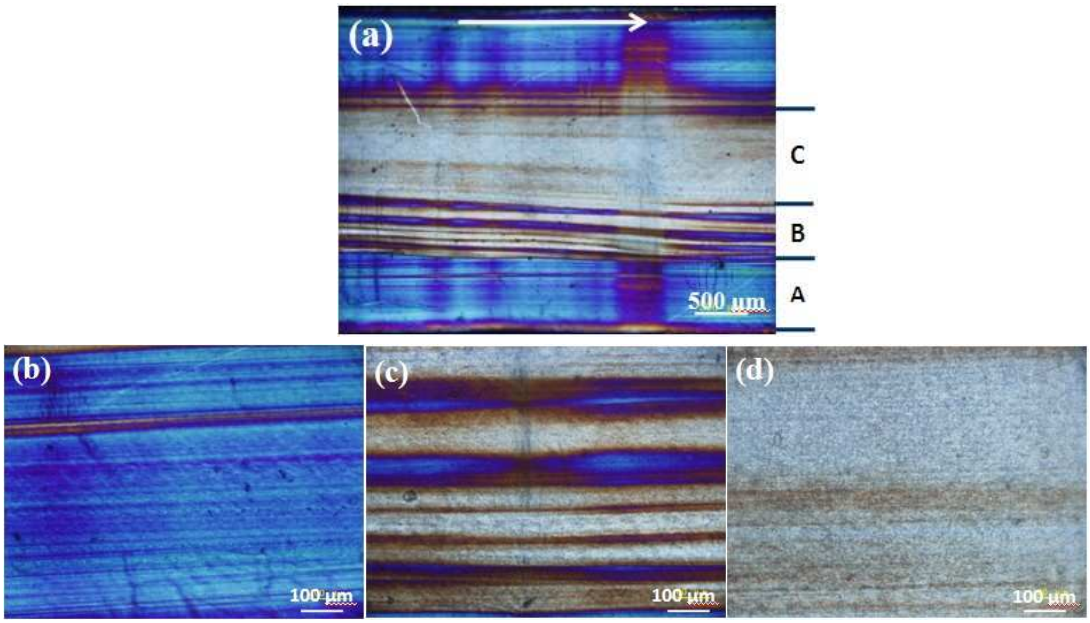

Fig. 4.2 (a): Polarized optical micrograph of a cross-section of the injection-molded iPP sample; (b): zone A zone in (a) at higher magnification; (c): zone B in (a) at higher magnification, (d): zone C in (a) at higher magnification. The white arrow indicates the flow direction.

Fig. 4.3 shows the degree of orientation in the directions parallel and perpendicular to the flow direction for the injection-molded iPP at different positions from the skin to the core. The results corroborate the above conclusion that the degree of orientation of the injection-molded iPP sample gradually decreases with increasing distance from skin to core. The highest degree of orientation is found in the skin layer, as expected. The degree of orientation in the crystalline and amorphous phases in the flow direction is higher than that in the direction perpendicular to the flow. The change in the degree of orientation of the amorphous phase follows the same trend as that of the crystalline one, indicating that the amorphous phases are spatially constrained by the crystalline ones. Moreover, the degree of orientation of the amorphous phase in the flow direction is significantly lower than that of the crystalline phase. However, the degree of orientation of the amorphous phase in the direction perpendicular to the flow direction is close to that of the crystalline one, indicating that spatial restriction the crystalline phase imparts to the amorphous phase in perpendicular direction is weaker than that in the flow direction.

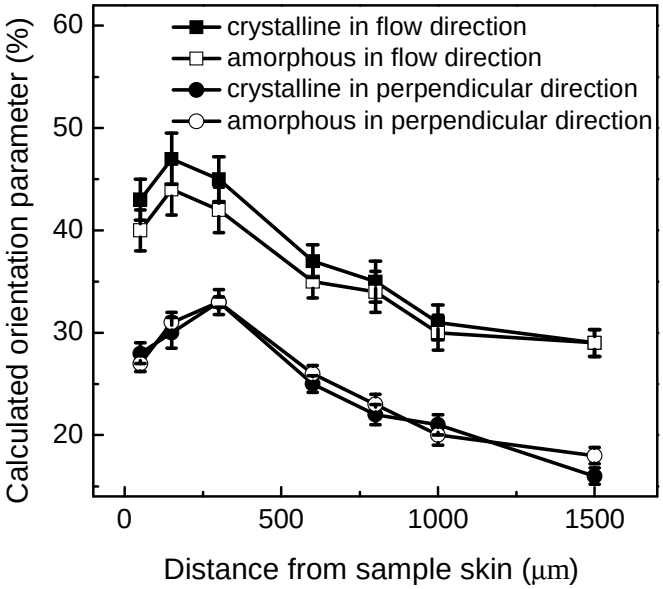

Fig. 4.3 Degree of orientation of the crystalline phase and amorphous phase along the thickness determined by IR for the injection-molded iPP in both the flow and perpendicular directions.

Fig. 4.4 shows the SAXS patterns of zones A, B and C in Fig.4.3a. The flow direction of samples is shown in Fig. 4.4, and the measurement direction is vertical. Typically, the equatorial streak in an SAXS pattern is attributed to the formation of an oriented structure or shish parallel to the flow direction. The meridional maxima are attributed to the layer-like oriented structure or kebab perpendicular to the flow direction [93]. Therefore, the obvious equatorial streak in Fig. 4.4a-b indicates the presence of shish-like crystalline structure from the skin layer to the intermediate layer. The strong reflection along the equator and the significant increase in the meridional maxima in Fig. 4.4a indicate the presence of shish-kebab crystal structure. The isotropic scattering pattern in Fig. 4.4c indicates the presence of spherulites in the core layer.

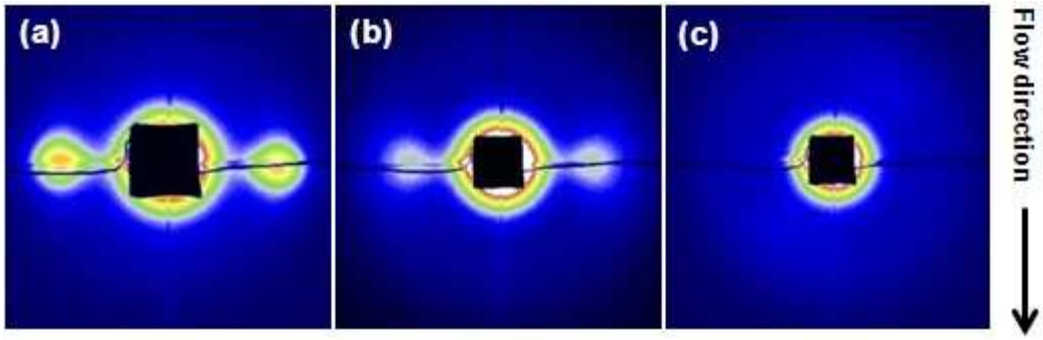

Fig. 4.4 2D SAXS images of zone A (a), zone B (b), and zone C (c) in Figure 3a.

Fig. 4.5 shows the crystalline phase morphology of the injection-molded iPP sample in skin layer and core layer. In the skin layer (Fig. 4.5a), it displays oriented crystals, i.e.,

shish-kebabs. Typical spherulites are observed in the core layer. They are composed of a crosshatched center, radial lamellae and the boundaries (Fig. 4.5b).

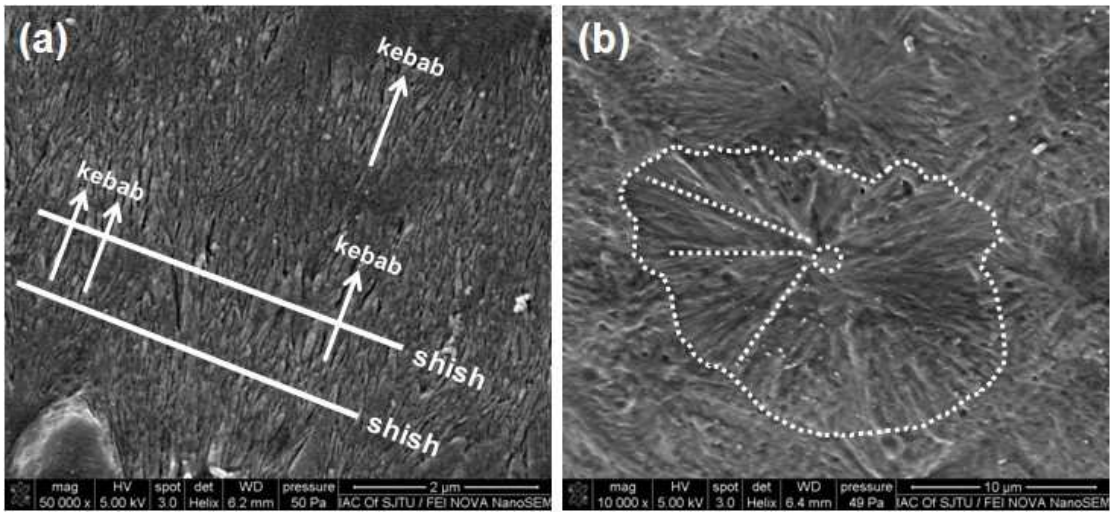

Fig. 4.5 SEM photographs of the injection-molded iPP samples after etching. (a) skin layer, and (b) core layer.

4.3 Thermal behavior of the injection-molded iPP under CO_2

Fig. 4.6 shows the melting behavior of the skin and core of the injection-molded iPP at the heating rate of 10 ^{o}C/min and under N_2 at ambient pressure or CO_2 at various pressures. The melting temperature of the iPP decreases with increasing CO_2 pressure. This is ascribed to the plasticization effect of CO_2 on the polymers [36]. Fig. 4.6a and b show that the melting behavior of the skin layer of the injection-molded iPP sample is different from that of the core layer. The DSC curves in the skin layer (Fig. 4.6a) show two obvious endothermic melting peaks, corresponding to the presence of shish-kebab structures in the skin layer [45]. Furthermore, the melting curves of both skin and core layers are very broad. Its starting and ending points are denoted the starting (T_{ms}) and ending (T_{me}) melting temperatures, respectively [42]. The temperature corresponding to the maximum of the DSC curve is taken as the melting temperature (T_m). Fig. 4.7 shows the T_{ms}, T_m and T_{me} of the injection-molded iPP as a function of the CO_2 saturation pressure corresponding to Fig. 4.6. The T_{ms}, T_m and T_{me} of the skin and the core of the iPP all decrease almost linearly with increasing CO_2 pressure. Their slopes are calculated and shown in Fig. 4.7. Moreover, the values of T_m and T_{me}, in the range of CO_2 pressure from 0 to 8 MPa, are always higher in the core layer than in the skin layer because the crystallization in the former is more complete.

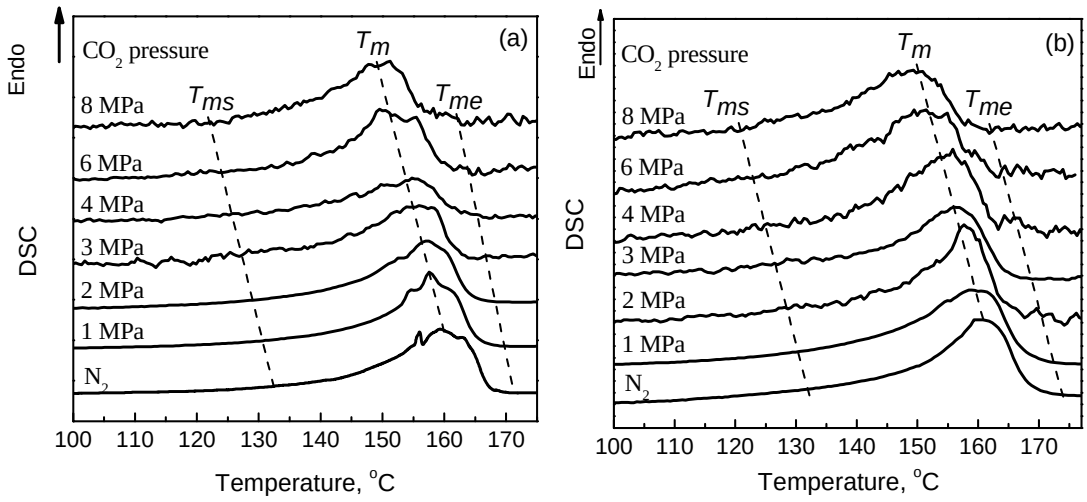

Fig. 4.6 High pressure DSC diagrams of the injection-molded iPP under N_2 at the ambient pressure or CO_2 at various pressures. (a) skin layer, and (b) core layer.

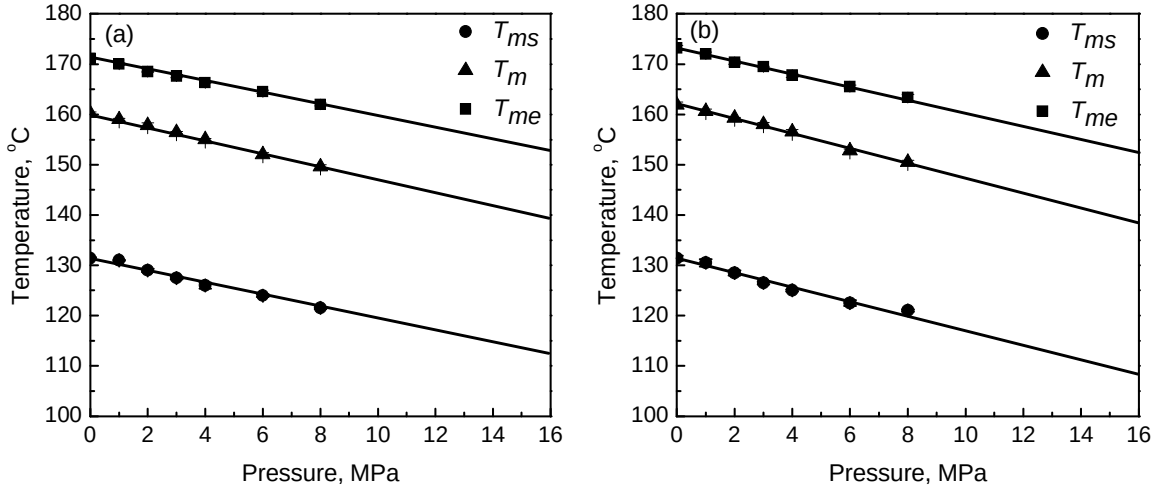

Fig. 4.7 Evolution of the starting melting temperature (T_{ms}), melting temperature (T_m) and ending melting temperature (T_{me}) of the injection-molded iPP as a function of CO_2 pressure. (a) skin layer, T_{ms}=131.8-1.33P (MPa); T_m=160.2-1.34P; T_{me}=171.1-1.15P, and (b) core layer, T_{ms}=131.4-1.42P; T_m=161.9-1.44P; T_{me}=173.2-1.27P.

4.4 Foaming of highly oriented iPP with scCO$_2$

4.4.1 Cell morphologies with foaming temperature increase

In the case of a solid-state foaming process, cell nucleation and growth only occur in amorphous regions where CO_2 is dissolved. During the foaming process, enough amorphous space is needed to accommodate cell nucleation and growth [52]. Furthermore, more crystals melt with foaming temperature increase. On the other hand, the starting melting temperature (T_{ms}) of PP2 sample is about 115 °C, while the CO_2 pressure is 15MPa

(see Fig. 4.7). Therefore, in order to study the effects of crystal structure on the foam cell morphologies, a broad range of foaming temperatures (115-145^{o}C) was used in the experiments while the CO_2 pressure is 15MPa. Fig. 4.8 shows the SEM photographs of the skin layer foamed at (a) 115^{o}C and (b) 125^{o}C with a CO_2 saturation pressure of 15 MPa. Cells started to form under the above foaming conditions. For the core layer, there is no bubbles can be found. It is because that the crystals in the core layer are more complete than those in the skin layer.

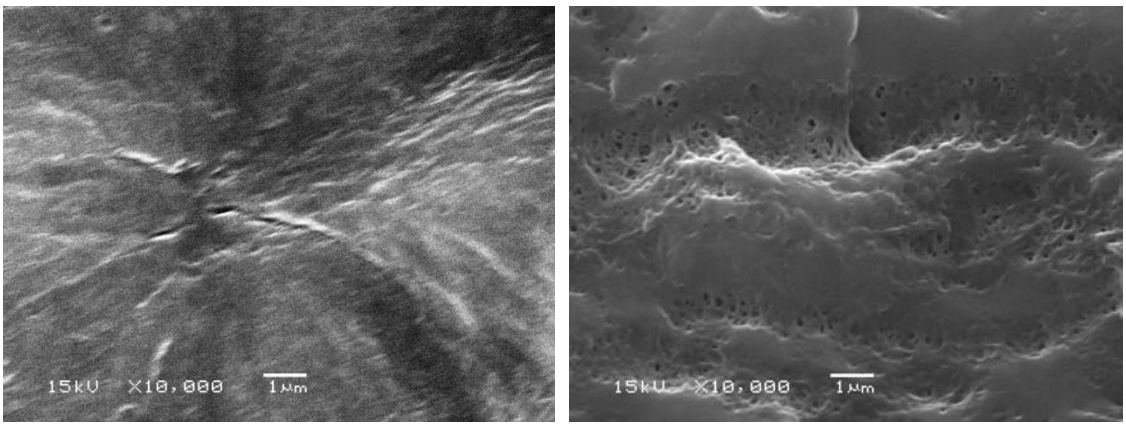

(a) (b)

Fig. 4.8 SEM photographs of the skin layer foamed at (a) 115^{o}C and (b) 125^{o}C with a CO_2 saturation pressure of 15 MPa.

Fig. 4.9 shows the cell morphologies of the skin and core after foaming at 135 ^{o}C and CO_2 saturation pressure of 15 MPa. From Fig. 4.9a, cells are formed along the orientation direction, as indicated by the arrow. The cell size is less than 1 μm (Fig. 4.9b). Fig.4.9c-d shows the cell morphologies of the core layer after foaming. A higher magnification allows observing a number of submicron cells generated (Fig. 4.9d). However, the amount of the cells of both the skin and core is not very large. There are large areas which are un-foamed.

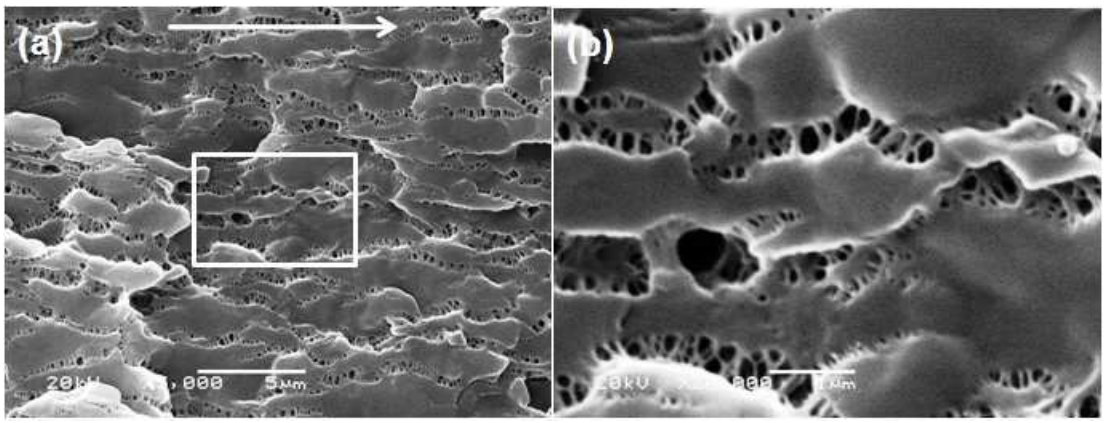

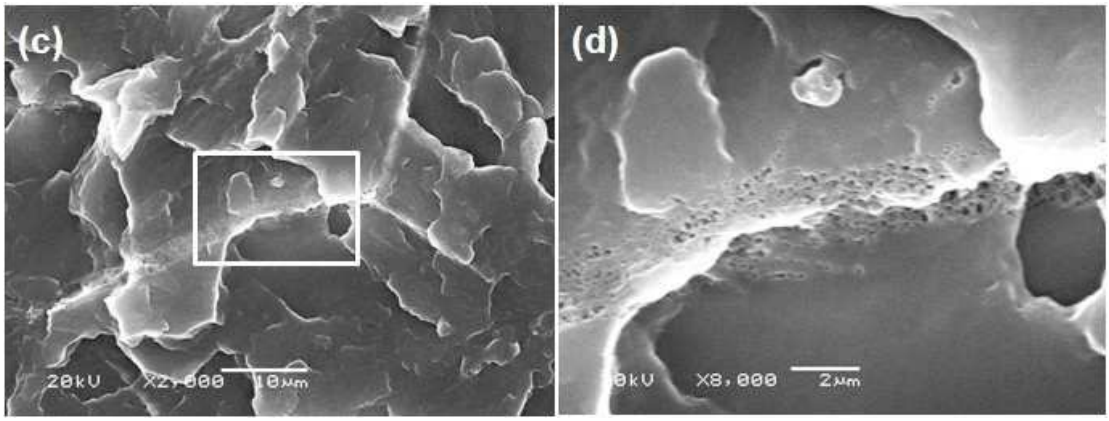

Fig. 4.9 SEM photographs of the skin and core layers foamed at 135 ^{o}C and a CO_2 saturation pressure of 15 MPa. (a) skin (the white arrow indicates the flow direction); (b) magnification of the white rectangle in part (a) and the white bar is 1 μm; (c) core; and (d) magnification of the white rectangle in part (c).

As stated above during the foaming process of a semicrystalline polymer such as iPP in the solid state, cell nucleation and growth only occur in amorphous regions where CO_2 are dissolved. However, it does not mean that the un-foam regions are all crystals phases. During the foaming process, enough amorphous space is needed to accommodate cell nucleation and growth [52]. In other words, the un-foamed regions in Fig. 4.9 consist of not only crystal domains but also amorphous ones in which crystals are finely connected together. These inter-connected crystals may constrain cell nucleation. On the other hand, the cell morphology in Fig. 4.9 indicates that only the weakest crystalline regions are molten at 135^{o}C and 15 MPa saturation pressure.

Fig. 4.10 shows the cell morphologies of the skin and core layers foamed at 140^{o}C and a CO_2 saturation pressure of 15MPa. They are more uniform than those obtained at 135^{o}C (see Fig. 4.9). This is expected because at a higher foaming temperature, more crystals are molten, providing more space for cell nucleation and growth. On the other hand, Fig. 4.10a-b show that cells are still aligned along the initial orientation of the shish-kebab crystal structures. This implies that only a small portion of these shish-kebab crystal structures are molten. From Fig. 4.10c-d, numerous submicron cells around a microcell are observed. The texture around the microcell, characterized by the radially distributed submicron cells (see the dotted lines in Fig. 4.10c), reveals the architecture of the corresponding spherulite [42]. It also infers that microcells are formed from the centers of the spherulites of the iPP. It is because that the crosshatched center of a spherulite is a highly disordered crystalline domain with low crystallinity and can melt at a temperature lower than that for the dominant radial lamellae [42].

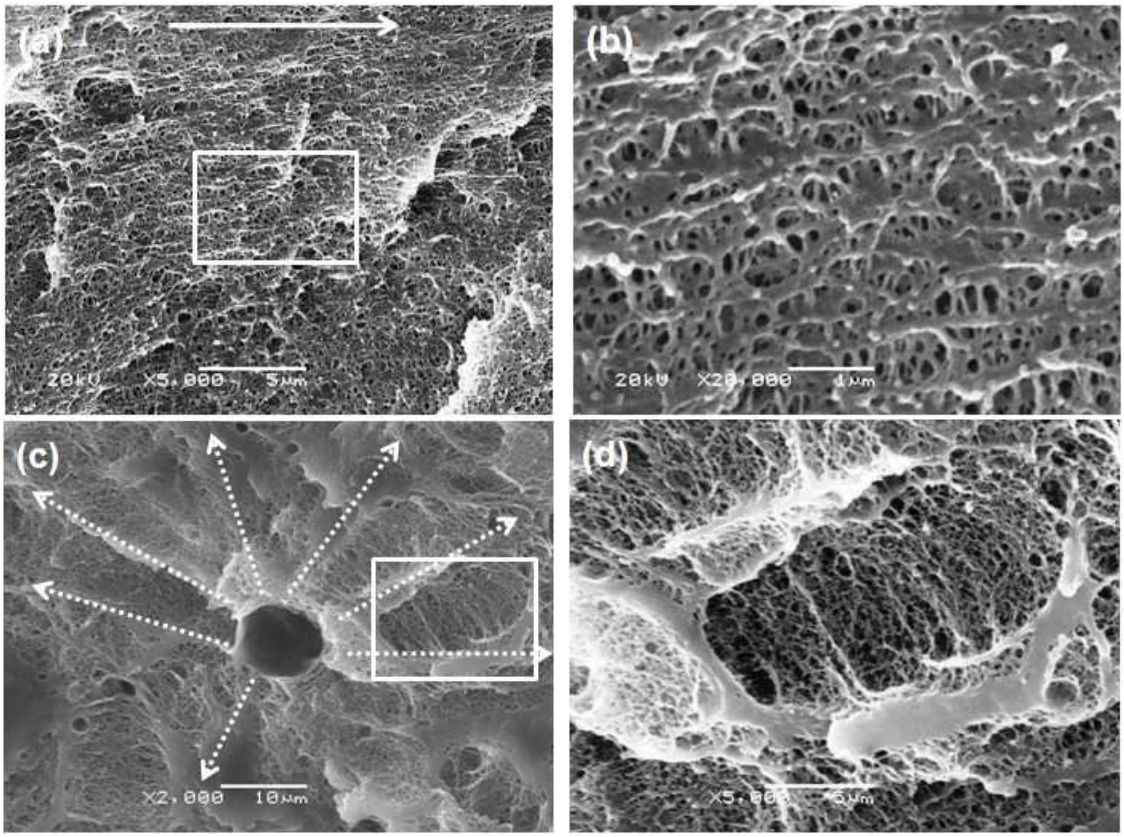

Fig. 4.10 SEM photographs of the skin and core layers foamed at 140 ^{o}C and a CO_2 saturation pressure of 15 MPa. (a) skin foam (the white arrow indicates the flow direction); (b) magnification of the white rectangle in part (a) (the white bar is 1 μm); (c) core foam; and (d) magnification of the white rectangle in part (c) (The white bar is 5μm).

Fig. 4.11 shows the cell morphologies of the skin and core layers foamed at 143^{o}C and a CO_2 pressure of 15 MPa. The orientation of the cell morphology observed in the skin layer (Fig.4.11a-b) has disappeared and an open nanocellular structure is obtained. On the other hand, the cell morphology of the core layer in Fig. 4.11c and 12d is similar to that in Fig.4.9c-d, in which a microcell is surrounded by a number of submicron cells. Nevertheless, the microcell in Fig.4.11c is larger in size than that in Fig. 4.10c.

Moreover, unlike the cells in Fig. 4.10d which are closed, those in Fig. 4.11d in the interlamellar regions become open. This is because at a given foaming pressure, more crystals can be molten when increasing foaming temperature. A larger portion of the center of spherulite is molten, leading to larger expansion of the microcell. Interlamellar amorphous materials and thin crystal lamellae may also be molten. In general, in addition to tie fibrils which consist of tie molecules passing through several lamellae and amorphous interlayers, interlamellar amorphous materials are mainly composed of chains of low molar mass or stereo-irregular chains that do not exhibit the required symmetry for crystallization and consequently are rejected out of lamellae during crystallization [42]. Accordingly, the

elongational viscosity of the interlamellar materials would be very low when they are molten. Thus cell rupture would occur during cell growth and cells generated in the interlamellar regions would become open because the interlamellar materials were in the molten state.

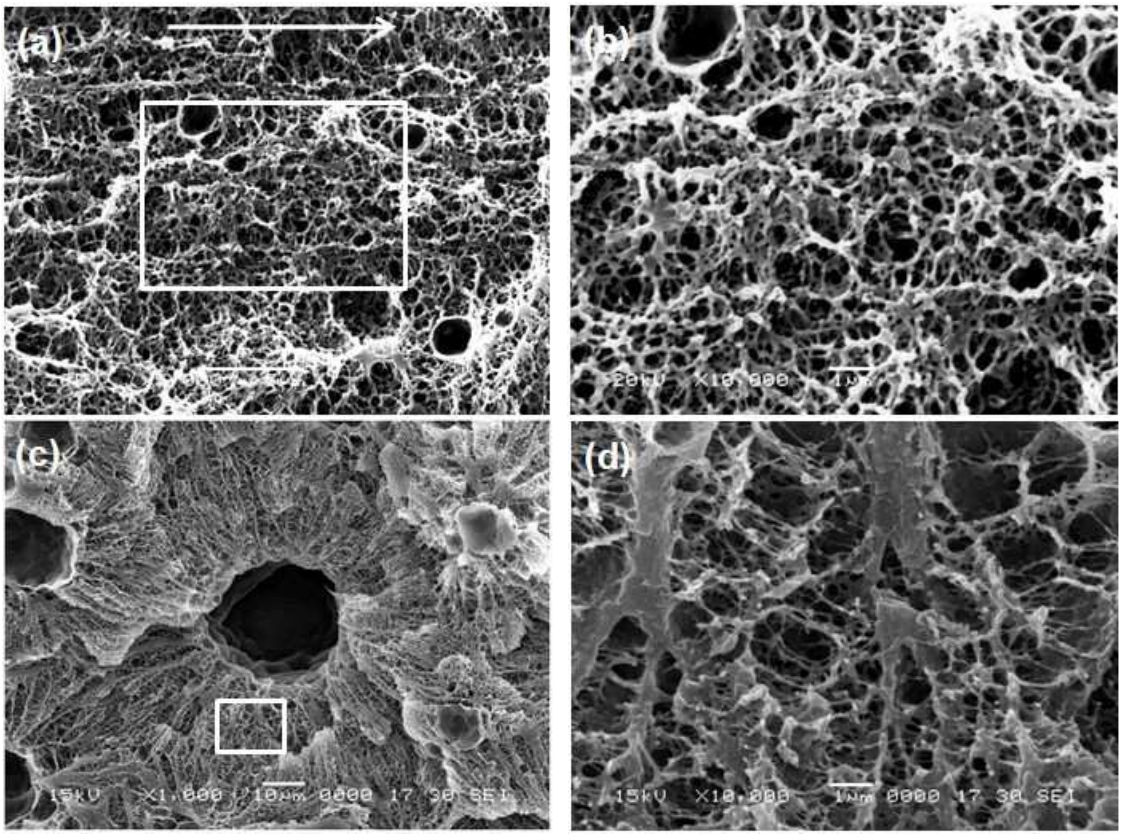

Fig. 4.11 SEM photographs of the skin and core layers foamed at 143 ^{o}C and a CO_2 pressure of 15 MPa. (a) skin foam (The white bar is 5 μm and the white arrow indicates the flow direction); (b) magnification of the white rectangle in part (a) (The white bar is 1 μm); (c) core foam; (d) magnification of the white rectangle in part (c).

Fig. 4.12 shows the effect of the foaming temperature (from 125 to 143^{o}C) on the final cell structure of the skin foam in terms of the average cell diameter and cell density. By the way, the cell morphology of iPP sample foamed at 115^{o}C is difficult for analysis (see Fig. 4.8a). From Fig. 4.12, the cell size increases with increasing foaming temperature. However, unlike conventional scCO_2 foaming for which the cell density often decreases with increasing foaming temperature when the CO_2 pressure remains constant [17, 85]. It is remarkable that in this work, the cell density increases with increasing foaming temperature from 135 to 143^{o}C. This is because more crystalline domains are molten with increasing foaming temperature, resulting in more space available for cell nucleation and growth. Meanwhile, the remaining crystals prevent neighboring cells from collapsing into larger ones. Therefore, the cell density increases with increasing temperature from 125 to 143^{o}C.

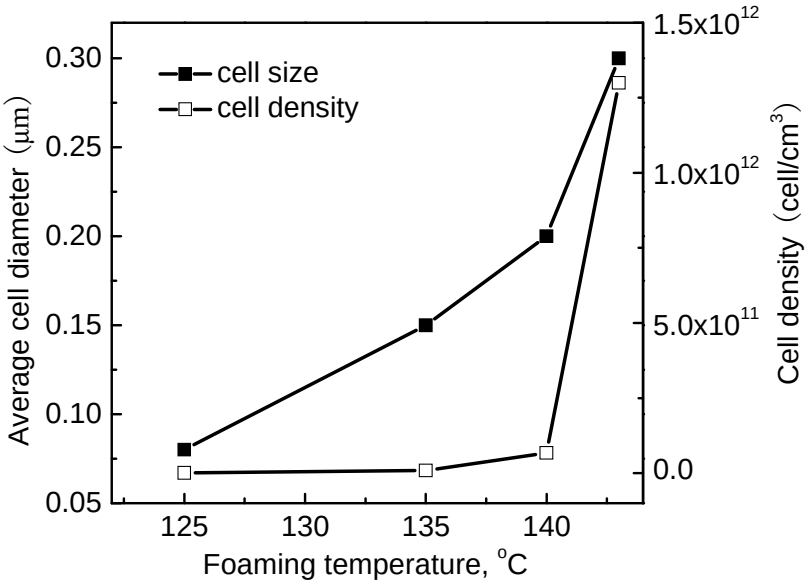

Fig. 4.12 Effect of the foaming temperature on the average cell diameter and cell density of the skin foam. The saturation pressure is 15MPa. Data for the core are unavailable because of the poorly defined cells (see Fig. 4.9c-d and Fig. 4.10c-d).

However, if more crystals were molten and the restriction of crystal phase disappeared, cells would collapse into larger ones with a concomitant decrease in cell density. That is the reason that when the foaming temperature is increased from 143 to 146°C, the cell size of the skin foam abruptly increases to about 68 μm and the corresponding cell density decreases to 5.3×10^6 cell/cm^3 (Fig. 4.13a). Moreover, compared with Figure 4.13a, the cell size in Figure 4.13b is smaller and the cell morphology is less uniform. It indicates that, under the foaming conditions of 146°C and 15MPa, cell growth in the core is more constrained than in the skin. It is evident in Figure 4.14, which shows that the peak temperatures of the core specimen foamed under the conditions of 146°C and 15MPa are higher than those from the skin.

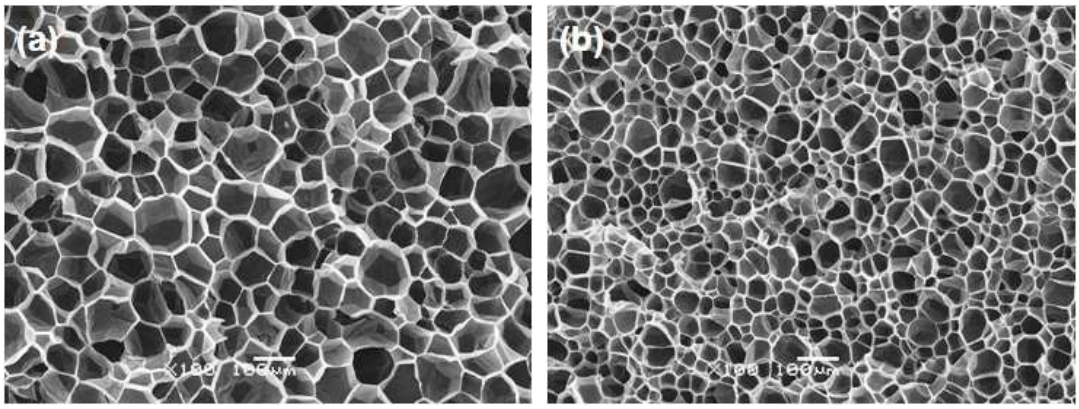

Fig. 4.13 SEM photographs of the skin and core layers foamed at 146 ^{o}C and a CO_2 pressure of 15MPa. (a) skin foam; and (b) core foam.

4.4.2 Impact strength of foamed PP2

According to the conclusion of chapter 3, the impact strengths of PP2 samples are constant, while treated under 15MPa CO_2 pressure and temperature from 80-125^{o}C. Fig. 4.14 shows the impact strengths of PP2 and PP4 compared with those of PP2 foamed under CO_2 pressure of 15MPa and various temperatures. When PP2 samples were foamed under 115 and 125^{o}C, the impact strengths of PP2 foams were higher than that of PP4. When the foaming temperature increased to 135, the impact strength of PP2 foam suddenly decreased to about 9.2 KJ/m^2 (lower than that of PP4). With the foaming temperature further increase, the impact strength of PP2 foams decreased. As the foregoing statement, more crystals melt with foaming temperature increase and the starting melting temperature (T_{ms}) of PP2 sample is about 115 ^{o}C, while the CO_2 pressure is 15MPa (see Fig. 4.7). As the mechanical properties of iPP are dictated by its crystallinity and crystalline morphology. It indicates that when the foaming temperature is lower than 125^{o}C, the crystals are barely molten. The nanocellular bubbles among the network crystals structure can further toughening the PP2 foams. When the foaming temperature further increased, more crystals melt which leads to the decrease of impact strength.

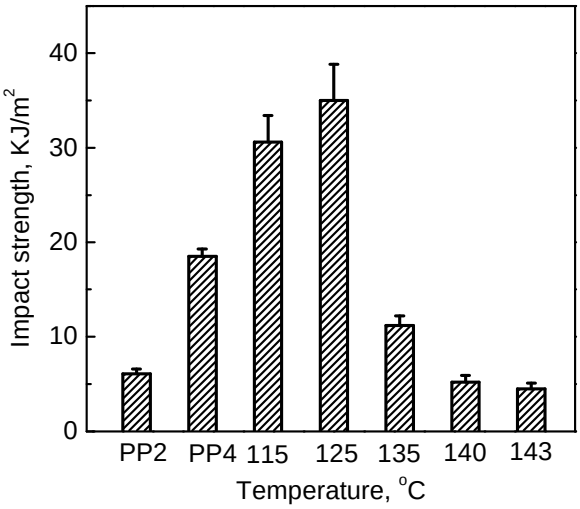

Fig. 4.14 Comparison of the impact strength of PP2 and PP4 with those of PP2 foamed under CO_2 pressure of 15MPa and various temperatures.

4.5 Thermal properties of the iPP before and after foaming

Fig. 4.15 shows the DSC thermograms of skin and core layers and their foams obtained at 115, 125, 135, 140, 143 and 146^{o}C, respectively. The saturation CO_2 pressure is 15MPa. From Fig. 4.15, the melting peaks of skin and core foams of 135, 140, 143, and 146^{o}C are all shifted to higher temperatures and a new shoulder peak is formed at lower temperatures, and the starting melting temperatures of skin

and core foams increase with foaming temperature increase, as demarcated by the arrows. A broad melting peak is attributed to a broad distribution of the lamellar thickness due to crosshatched structures consisting of thick primary lamellae with a higher melting temperature and thin subsidiary lamellae with a lower melting temperature [94]. The large increase in the melting temperature in Fig. 4.15 shows that after the annealing with $scCO_2$, the primary lamellae are significantly thickened. Meanwhile, a new shoulder peak is formed at lower temperatures, implying that the thickness of the thin subsidiary lamellae has not changed much during the $scCO_2$ saturation process [42]. On the other hand, the DSC traces of the skin and core foams obtained at 115 and 125°C show the higher ending melting temperature and lower starting melting temperature, compared with that of unfoamed one, which confirms the foregoing statement that the crystal structure is almost unbroken under these foaming conditions. Moreover, the DSC traces of the skin and its foams obtained at 135 and 140°C all show two obvious melting peaks, corresponding to primary lamellae crystals (shish-like crystals) and secondary crystals (kebab-like crystals), respectively [45]. This indicates the presence of shish-kebab crystals, in spite of the partial melting of crystals at high temperature and high CO_2 pressure. This is the reason that the cell structure in Fig. 4.9 and Fig. 4.10 still reveals the orientation of crystals. Then, more crystals are molten at a higher foaming temperature. This may result in complete disappearance of the orientation when the amount of the remaining solid crystals is low enough. This is the reason that cells in Fig. 4.11 are uniform and without any orientation. In the case of the foam obtained at 146°C, almost all thin crystals are molten, facilitating the cell growth in the interlamellar regions. Consequently, the cells generated in the interlamellar regions could grow into micron ones.

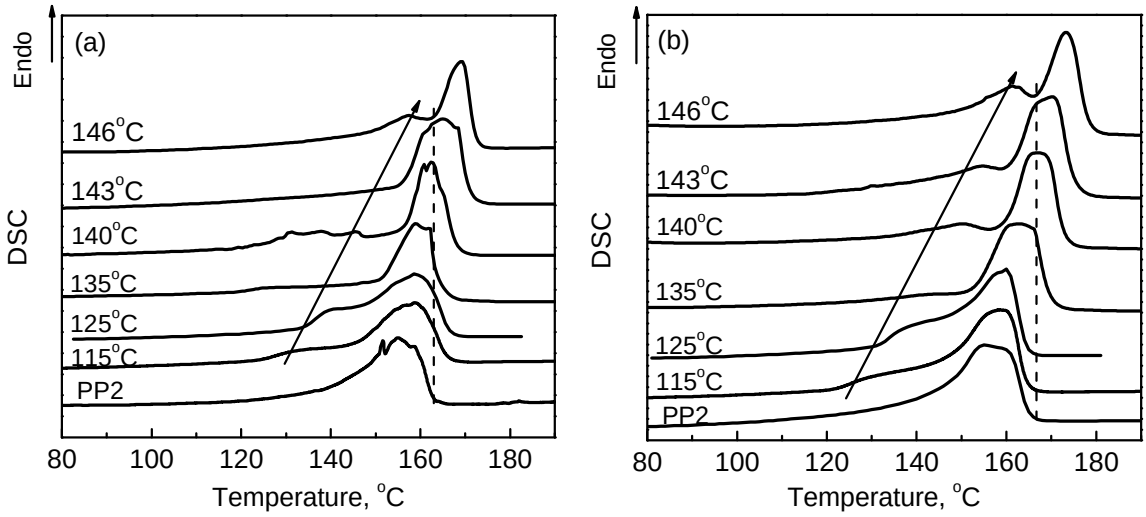

Fig.4.15 DSC thermograms of the skin and core and their foams obtained at 115, 125, 135, 140, 143 and 146 °C, respectively. The saturation CO_2 pressure is 15 MPa. (a) skin, and (b) core.

4.6 Conclusion

The use of a highly oriented isotactic polypropylene (iPP) with a shish-kebab crystalline structure obtained by injection molding as a template allows obtaining nanocellular foams by CO_2 foaming in the solid state under appropriate foaming temperatures and CO_2 pressures. The underlying principle is localized cell nucleation and growth in amorphous domains confined by the shish-kebab crystalline domains. At a chosen CO_2 pressure, the cell morphology depends very much on the foaming temperature. For example, when the CO_2 pressure is 15 MPa and the foaming temperatures are 115, 125 and 135^{o}C, only part of weak crystals is molten. When the temperature is increased to 140^{o}C, more crystals are molten including most of subsidiary lamellae or kebab and part of primary lamellae or shish. Thus oriented cells in submicron in size are generated and the un-foamed regions reveal the rest of the crystal structures. When the temperature is further increased to 143 ^{o}C, an open nanocellular morphology (See Fig. 4.10a-b) is successfully obtained with more crystals molten. However, when the temperature is increased to 146^{o}C, nearly all thin crystals are molten. As a result, cells in micrometer in size with smooth walls are formed due to weak restrictions of rigid crystals to cell nucleation, growth and coalescence. Moreover, the impact tests indicate that the nanocellular bubbles among the network crystals structure can toughening the scCO_2 treated iPP samples.

Chapter 5 Oriented Foaming of Polystyrene for Toughening

5.1 Introduction

The use of substantial volume fraction of extremely small rubber particles blended in polymer matrix is a well known technique for toughening of polymers. Since the toughening mechanisms start with rubber particle cavitation in order to relieve the triaxial stress state, the question has been raised many times of whether microbubbles could be substituted for the rubber particles. This idea of using microbubbles in order to toughen plastics was first implemented by Martini *et. al.*[15, 16] and the resulting structure was called microcellular foam.

In the past decade, efforts have been made to investigate the influence of processing conditions and the nature of polymers on the final cell morphologies of microcellular foams [51-54]. In addition, many researchers have investigated the relationship between the mechanical properties and the cell structures [59-63]. Results have shown that unlike conventional foams, with typically large variations in properties, microcellular foams exhibit consistent and improved tensile properties in systems such as polycarbonate (PC), polyethylene terephthalate (PET), and polyvinyl chloride (PVC) [60-62]. For instance, the tensile properties of microcellular PC foams reduce proportionally with the relative density, where relative density refers to the ratio of the density of the foam relative to that of the unfoamed one. On the other hand, the effect of cell morphologies on impact strength of microcellular foams has been studied in several polymer systems and the results have been mixed. Waldman [63] studied the impact strength of microcellular PS foams and found a greater impact strength for microcellular foams compared with that of unfoamed one. Collias and Baird [64] investigated the impact behavior of microcellular PS foams, and found no improvement in the impact strength of foamed samples compared to neat polymers. Moreover, Barlow et al. [65] studied the PC foams and found that the impact toughness of foams is improved within the microcellular range by increasing the average cell size. Doroudiani et al. [66] studied the cell size effects in PS and fould no change in impact strength by varying cell size with the microcellular range.

Besides, many unique cell structures were achieved for unique mechanical properties. Kelyn et al. prepared PS foams with oriented, bimodal cell structures and investigated the corresponding compressive behavior [95]. Miller and Kumar compared the tensile and impact behaviors of microcellular and nanocellular polyetherimide (PEI) foams with various relative densities, to that of unfoamed one, and found that nanofoams showed a

significantly higher strain to failure, resulting in an improvement in the modulus of toughness by up to 350% compared to microcellular foams [96].

In this study, an amorphous rigid polymer, polystyrene (PS), was employed to systematically study the effect of the foaming conditions and the cell structure parameters of microcellular foams on the mechanical properties. Thereafter, the oriented, anisotropic cell morphologies were prepared to investigate the relationship between the directions of cell oriented and the corresponding tensile and impact strength. The results indicated that the oriented cells perpendicular to the impact direction could significantly improve the toughness of PS foams, compared with those of isotropy foams.

5.2 The isotropic cell structure and mechanical properties

It is well known that polymers can be plasticized by dissolved gases and the glass transition temperatures T_g were significantly lower than those of the pure polymers [97, 98]. As a result, the cells could nucleate and grow at temperatures well below the T_g of the pure polymers. Therefore, a broad range of foaming temperatures (50-110^{o}C) was used in the experiments in order to study the effects of foaming temperature on the foam relative densities and cell morphologies. Fig. 5.1 shows the cell morphologies of PS samples foamed at 20 MPa CO_2 saturation pressure and various saturation temperatures (50-110^{o}C). With the foaming temperature increase, the thickness of cellular wall decreases and the cell size increases. Fig. 5a shows the effect of foaming temperature on cell morphology in terms of average cell size and cell density of Fig. 5.1. The average cell size increases with the foaming temperature, while the cell density decreases. As the temperature increases, the viscosity of the polymer decreases and the force that resists to the cell growth decreases and the diffusivity of CO_2 within the polymer increases. On the other hand, the solubility of CO_2 in polymers decreases upon increasing temperature [99]. Therefore, with the foaming temperature increasing, cell nucleation decreases and the nucleated cells tend to further grow into large ones, leading to the lower cell density and larger cell size. Fig. 5.2b shows the relative densities of PS foams as a function of foaming temperature. (As is done here, properties will generally be reported as values relative to those of the unfoamed ones.) From Fig. 5.2b, one can see the relative foam densities decreases significantly with increase in foaming temperature from 50 to 110^{o}C.

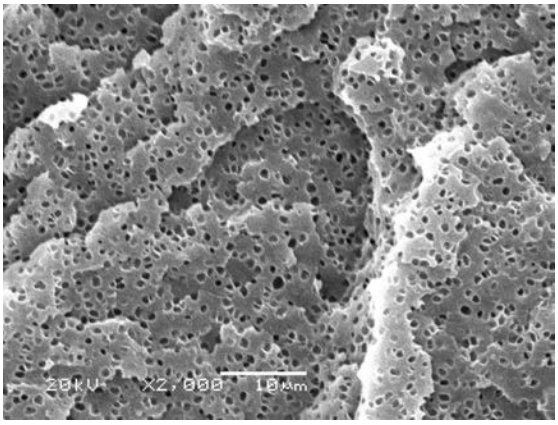
20kV X2,000 10μm

(a)

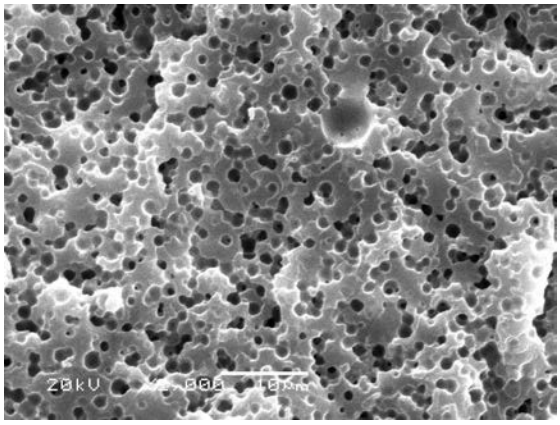
20kV

(b)

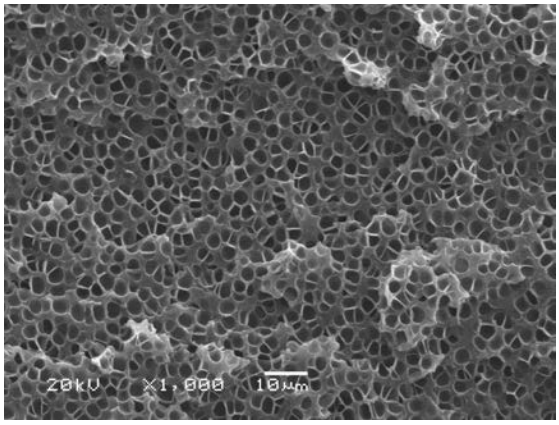
20kV X1,000 10μm

(c)

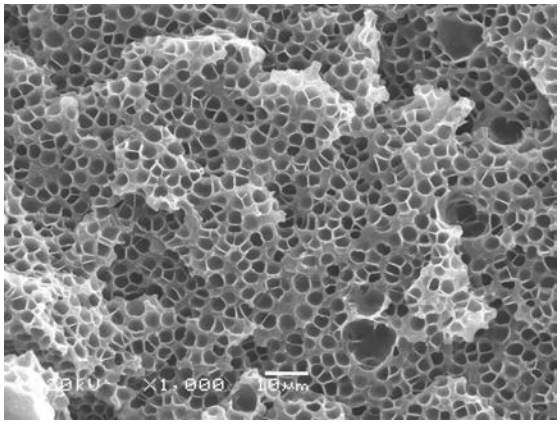
X1,000 10μm

(d)

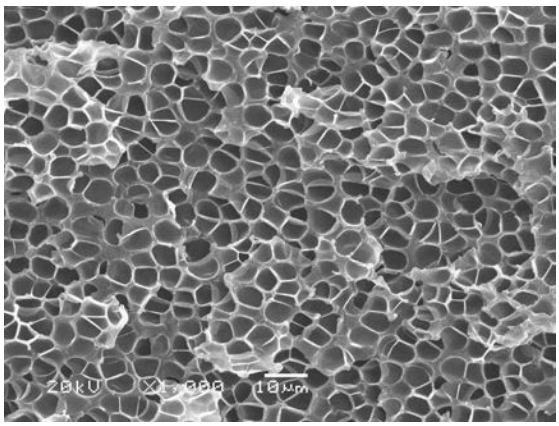
20kV 10μm

(e)

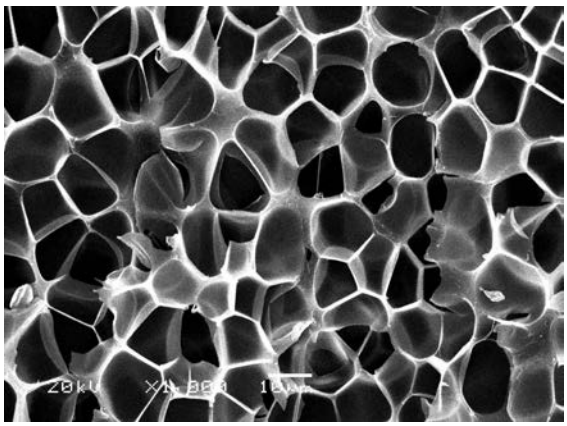
20kV

(f)

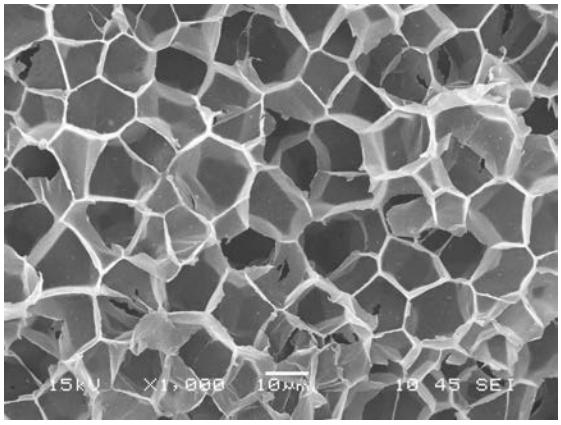

(g)

Fig. 5.1 SEM images of PS samples foamed at 20MPa CO_2 saturation pressure and various saturation temperatures: (a) 50°C, (b) 60°C, (c) 70°C, (d) 80°C, (e) 90°C, (f) 100°C and (g) 110°C. The white bar is 10 μm.

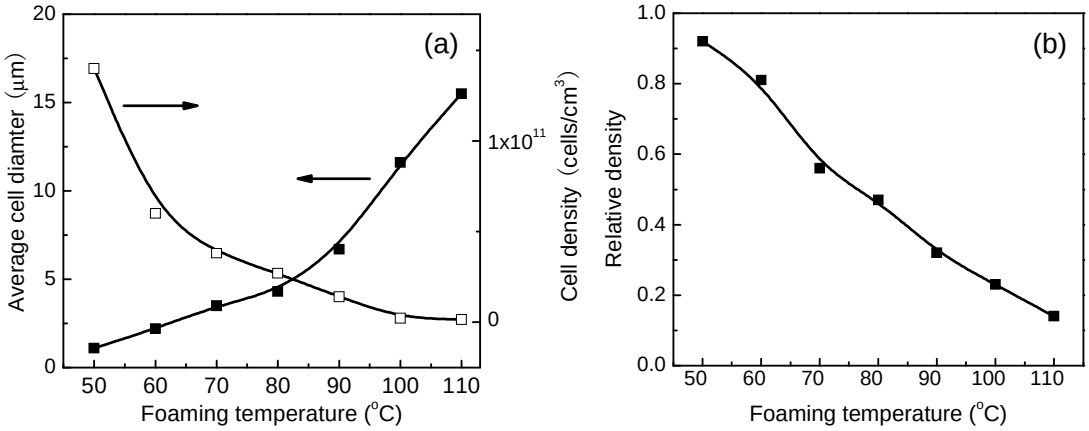

Fig. 5.2 (a) Effect of foaming temperature on cell morphology in terms of average cell size and cell density; (b) relative densities of PS foams as a function of foaming temperature.

In this study, the PS foams with the uniform cell morphologies as shown in Fig. 5.1 were cut into specimens for tensile and impact tests closely according to ASTM D-638 and D-256, respectively. Fig. 5.3 presents the tensile stress-strain curves of the PS foams with various foaming temperatures, and Table 5.1 summarizes these experimental data. It can be seen that, with a increase in the foaming temperature, the tensile strengths and the tensile modulus both decrease. It is because that, with the foaming temperature increasing, the cell size increases and the foam density decreases, which leads to the poor performance as expected [58, 66]. Moreover, most of the tensile tests show the brittle fracture except that the samples foamed at foaming temperature of 50 and 60°C show the higher elongation than that of unfoamed one. It may be because that the samples foamed at 50 and 60°C have higher relative density and smaller cell size than those foamed under high foaming temperatures (see Fig. 5.2).

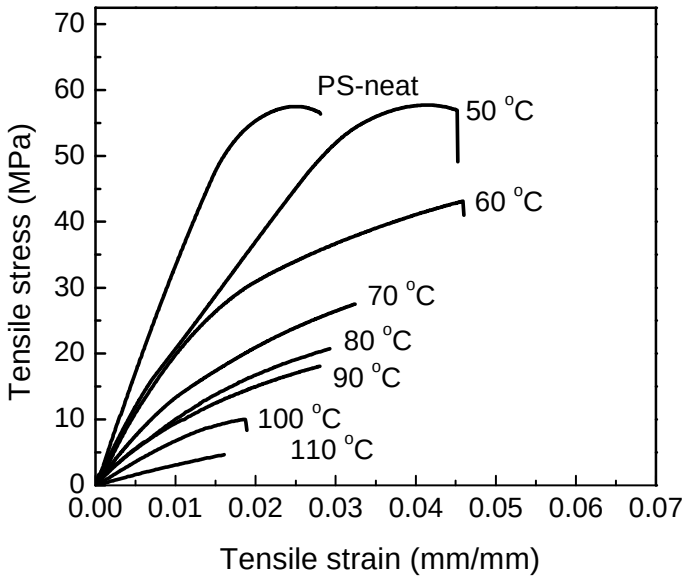

Fig. 5.3 Stress-strain curves for PS foams with various foaming temperatures.

Table 5.1 Summary of tensile test data.

Foaming temperature	Mean stress at break (MPa)	Standad deviation	Mean strain at break (mm/mm)	Standard deviation	Modulus of elasticity (MPa)	Standard deviation
unfoamed	57.4	2.1	0.025	0.003	4385	320
50 °C	56	1.8	0.043	0.006	3893	150
60 °C	43	2.2	0.045	0.004	3587	238
70 °C	27.5	2.4	0.032	0.007	1750	226
80 °C	20.7	1.6	0.029	0.005	743	165
90 °C	18	1.8	0.028	0.008	522	87
100 °C	10	1.1	0.019	0.004	157	45
110 °C	4.6	0.7	0.016	0.003	71	18

According to the predictions of the current theory for conventional foams, the tensile modulus of most closed-cell foams can be related to the foam relative density by the formula: [100]

$$E_f / E_m = \left(\rho_f / \rho_m\right)^2 \tag{5.1}$$

Where E_f is the Young's modulus of the foamed PS (MPa); E_m is the Young's modulus of the unfoamed PS (MPa); E_f / E_m is relative Young's modulus; ρ_f is the foam density (g/cm^3); ρ_m is the unfoamed PS density (g/cm^3); and ρ_f / ρ_m is the relative density.

In the case of tensile strength, the simple rule of mixtures gives the formula: [60]

$$\sigma_f / \sigma_m = \rho_f / \rho_m \tag{5.2}$$

Where σ_f and σ_m are the tensile stress at break of the foamed and unfoamed polymers, respectively. The experimental results of the relative tensile modulus (E_f / E_m) and the relative tensile strength (ρ_f / ρ_m) are plotted together with the theoretically predicted values as a function of the relative density in Fig. 5.4 The results show that the relative Young's modulus are in good agreement with the theoretical values, but the tensile strengths are a little lower than the values calculated from Eq. (5.2) except the one foamed at 50°C with the relative density of 0.92.

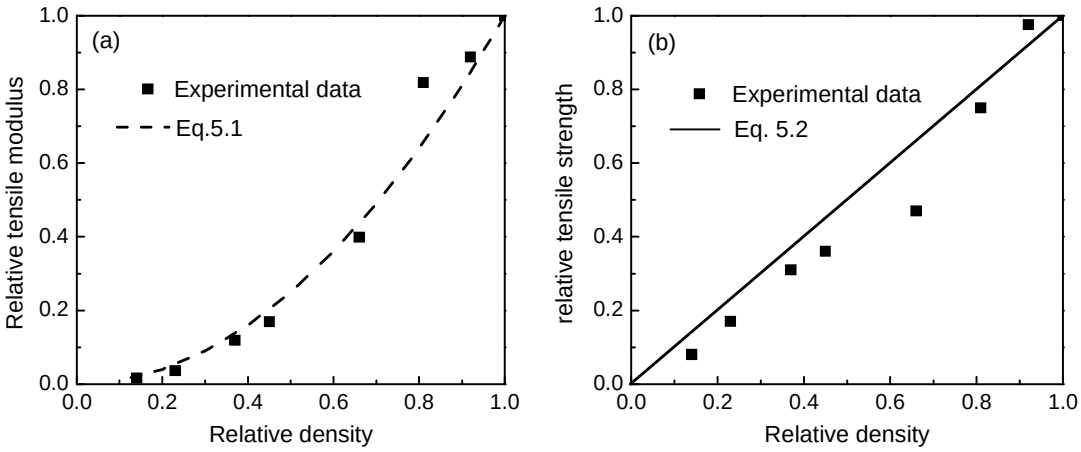

Fig. 5.4 Comparisons of the tensile values of the relative Young's modulus (a) and relative tensile strength (b) for PS foams with those predicated by Eqs. (5.1) and (5.2).

Fig. 5.5 shows the relative impact strength of non-notched and notched PS specimens as a function of relative density. With the relative density increase, the relative impact strength of non-notched and notched samples both increases. On the other hand, the values of relative impact strength of notched PS samples are always higher than those of non-notched ones. It is well known that the fracture energy of the notched samples mainly corresponds to the crack propagation energy and the fracture energy of the non-notched samples consists both of the crack initiation and propagation energies. Therefore, it is indicated that the bubbles in the PS matrix could increase the crack propagation energy during the impact tests.

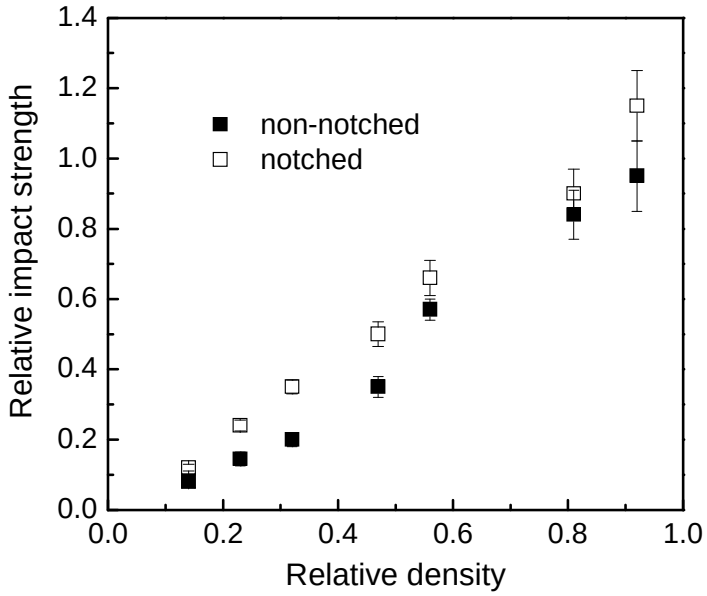

Fig. 5.5 Comparison of the relative impact strength obtained by non-notched and notched impact tests as a function of relative density.

According to the foregoing discussion, the tensile modulus, the tensile strength and the impact strength of PS foams all increase with the increase of relative density. However, it should be noted that the specimens used for both tensile and impact tests were various in the cell size. In other words, the cell size in the specimens for tests increased with the relative density decrease (see Fig. 5.2a). Therefore, it is very necessary to isolate the effect of cell size and relative density.

5.2.1 The effect of cell size on the mechanical properties

It is well known that in the process of batch foaming by depressurization, the foaming temperature, saturation pressure and the depressurization rate are the main parameters which affect the cell morphologies [17, 20]. Generally, the cell size increases and the cell density decreases with the foaming temperature increase (see Fig. 5.1 and 5.2). Moreover, a higher depressurization rate can generate a higher cell density and a smaller cell size. For a given temperature, the solubility of CO_2 in the PS is approximately a linear function of the saturation pressure for low and moderate pressures [101, 102]. It reaches a plateau for high pressures [99]. Therefore, a higher degree of depressurization results in a higher degree of super-saturation leading to the larger amount of nucleated cells.

In this study, to obtain the PS foams in similar relative density with various cell sizes, the foaming temperature, the saturation pressure and the depressurization rate were adjusted to control the final cell morphologies. Fig. 5.6 shows the cell morphologies of the obtained PS foams in similar relative density of 0.3±0.02 with the average cell size in the range of

6.7-22.5 μm. Then, the samples were taken for tensile and impact tests and the results were shown in Fig. 5.7. It indicates that over this range of cell sizes (6.7- 22.5 μm), cell size does not affect the tensile strength and modulus but has a weakly effect on the impact strength. The relative impact strength increases with the cell size decrease when the relative density is constant. To verify this, another series of PS foams with relative density of 0.56±0.03 and average cell size of 3.5-15.8 μm are achieved with the cell morphologies shown in Fig. 5.8. The results shown in Fig. 5.9 confirm that the cell size has the effect on the impact strength of foams.

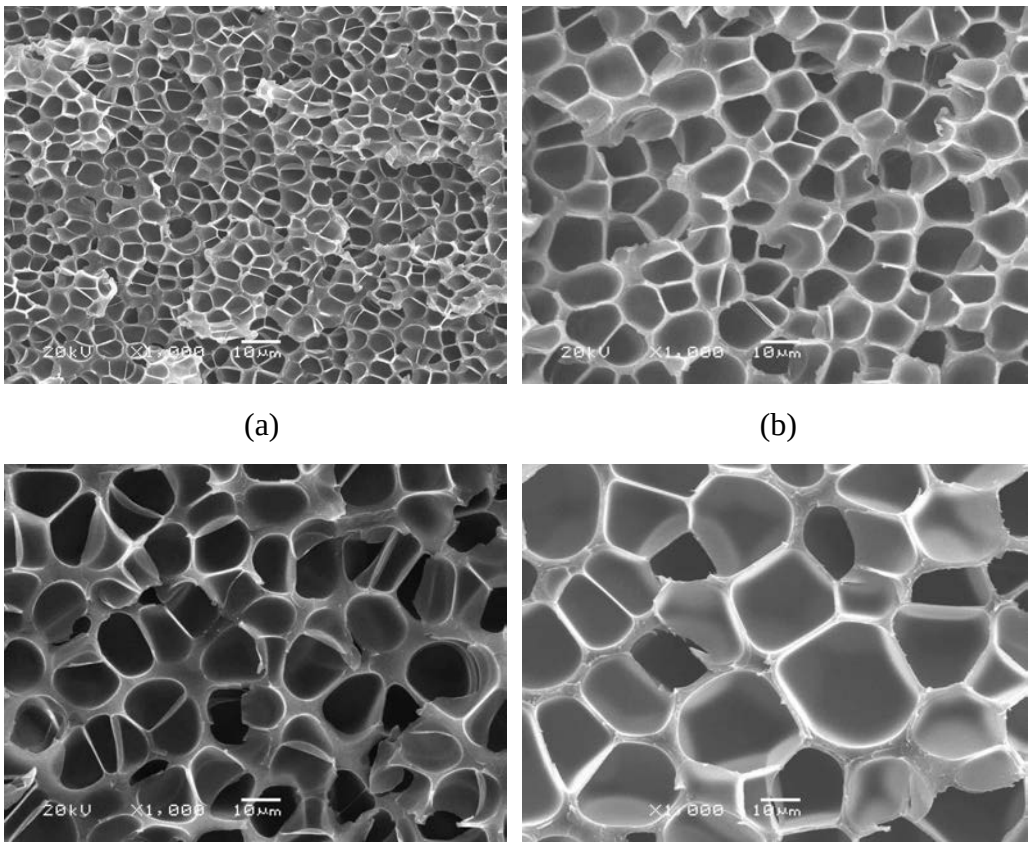

(a) (b)

(c) (d)

Fig. 5.6 SEM images of cell morphologies of PS foamed in the similar relative density of 0.3±0.02 with various average cell size: (a) 6.7 μm, (b) 10 μm, (c) 14.5 μm and (d) 22.5 μm. The white bar is 10 μm.

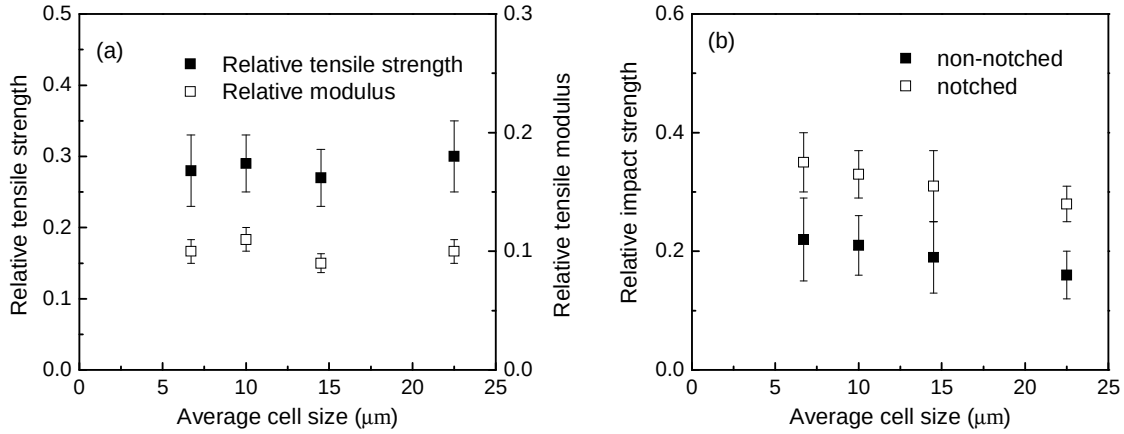

Fig. 5.7 Effect of cell size on mechanical properties in terms of (a) relative tensile strength and relative tensile modulus, and (b) non-notched impact strength and notched impact strength. The relative density is 0.3±0.02.

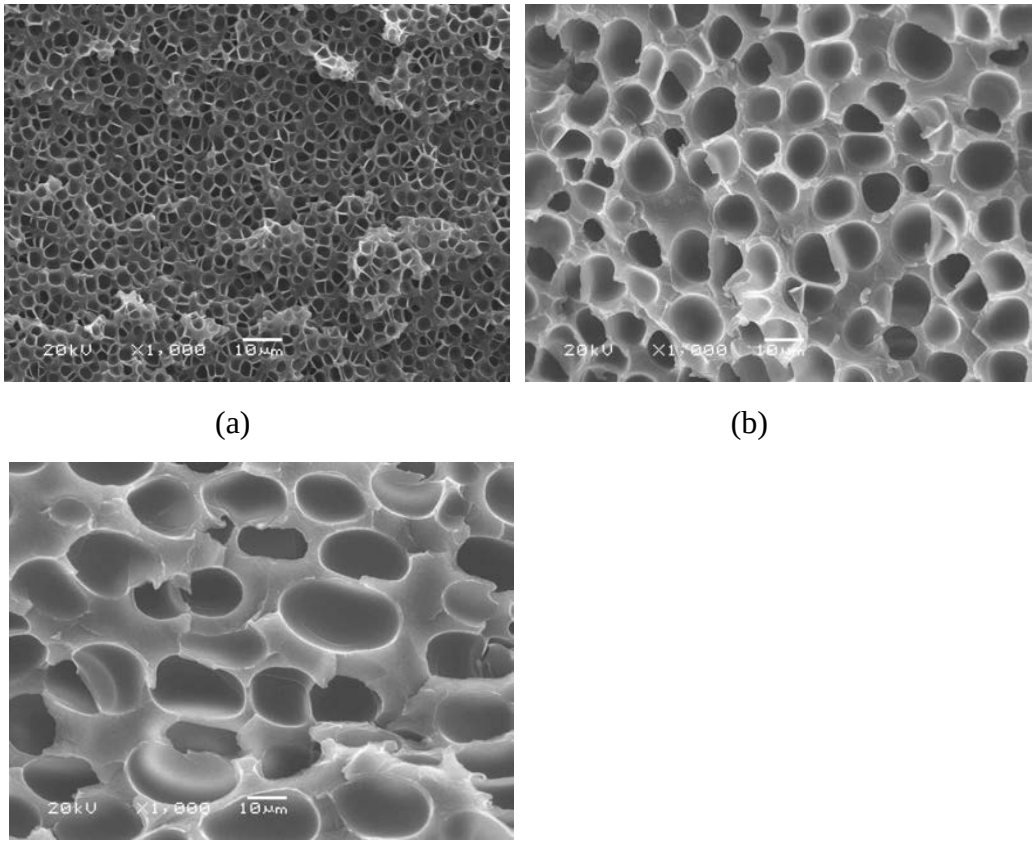

(a) (b)

(c)

Fig. 5.8 SEM images of cell morphologies of PS foamed in the similar relative density of 0.56±0.04 with various average cell size: (a) 3.5 μm, (b) 9.2 μm, and (c) 15.8 μm. The white bar is 10 μm.

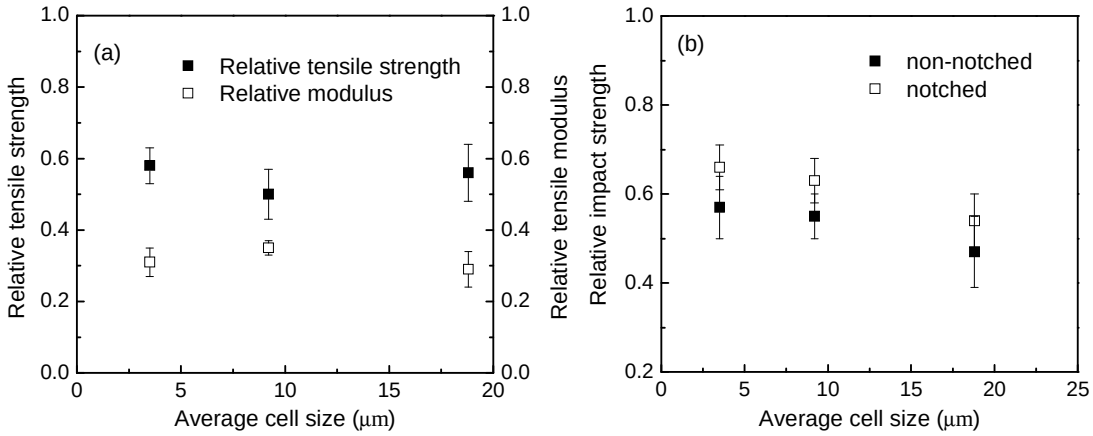

Fig. 5.9 Effect of cell size on mechanical properties in terms of (a) relative tensile strength and relative tensile modulus, and (b) non-notched impact strength and notched impact strength. The relative density is 0.56±0.04.

Fig. 5.10 shows the schematic of the propagation of a crack through bubbles. The fractures in the bubbles may perform by two types as shown in Fig. 5.10: trans-cell fracture or cell-boundary fracture. The deformation of cells at the crack tip as a result of bending extension and even buckling of cell walls and all of these mechanisms can contribute to the overall energy absorption in an impact test. Plastic deformation of the cell walls is an important source of energy dissipation and toughness [66]. Polymers will yield at some stress level, and this deformation is irreversible and leads to energy dissipation. Yield at the tip of a crack in a thick material is constrained by “plane strain” conditions that exist, and this reduces the energy needed to drive the crack and, hence, reduces the measured toughness [103]. In a foamed polymer, the material is distributed in relatively thin membranes, in which yield is facilitated due to the absence of constraint from the surrounding material. Therefore, to some extent, the cells in the polymer matrix can be considered as fillers in a multiphase system, in which the cell is one phase and the cell wall is another phase. In this way, the theories established for other multiphase systems can be applied to foamed polymers, where the cell is treated as a filler of zero modulus. In other words, the cell walls segregated by bubbles play a main role for the mechanical properties. That is why the impact strength of foams increases with the cell size decreases when the relative density is constant. With the same relative density, the cell density must increase with the cell size decrease according to the equations shown in the section of “foam characterization”. Thus, with higher cell density, the cell walls among the cells could be segregated better than those of lower cell density.

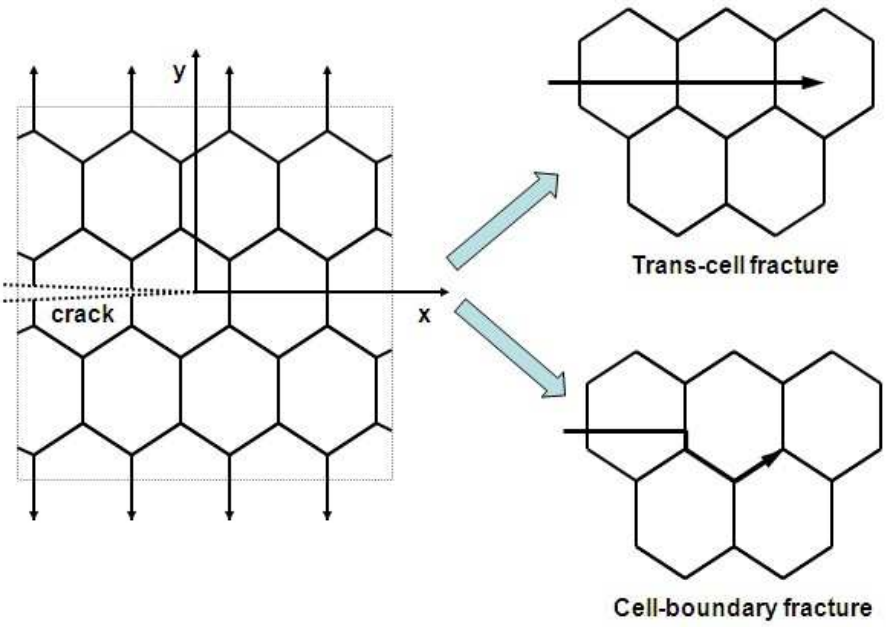

Fig.5.10 Schematic of crack propagation through the bubbles.

5.3 The oriented cell structure and mechanical properties

According to the statement above, plastic deformation of the cell walls is an important source of energy dissipation and the finely dispersed cell walls by bubbles play another main role for the mechanical properties. Therefore, an effective method for toughening foams is increasing the solid area (cell walls) on the plane of disruption and meanwhile finely segregating the solid with the small cells. In other words, the better mechanical properties must be achieved with the smaller cell size, the higher cell density and the higher relative density. Nevertheless, as the microcellular foams, low density is one of the most important factors for its application. It there any better method for toughening the PS foam while still keeping its low density? Let us take a look at Fig. 2.3, using the confined foaming, the cells can be controlled to grow along the three dimensions (a-axis, b-axis and c-axis). If the cells oriented perpendicular to the impact direction, the corresponding dispersion of cell walls on the fracture surface must be better than that of the isotropy cell morphologies with the similar relative density and average cell size (see Fig. 2.3).

Therefore, with the cells oriented perpendicular to the impact direction (c-axis direction), a foam with high area fraction of cell walls on fracture surface and low relative density is possibly achieved. On the other hand, the oriented bubble is not spherical but be similar to cylindrical. The cell morphology viewed along the oriented direction is similar to ellipse and the one viewed perpendicular to the oriented direction must be round (see Fig. 5.11).

Then, the orientation degree of the oriented bubble can be defined as

$$f = (a-b)/a \tag{13}$$

Where, a is the long axis of the ellipse and b is the diameter of the round (see Fig. 5.11).Then the foams with various cell morphologies (a-axis oriented, b-axis oriented and c-axis oriented) are all cut into standard specimens for tensile and impact tests, respectively. The tensile direction is parallel to c-axis, and the impact direction is perpendicular to c-axis. In the following section, a-oriented, b-oriented and c-oriented are used for the representation of the cells oriented along a-axis, b-axis and c-axis, respectively.

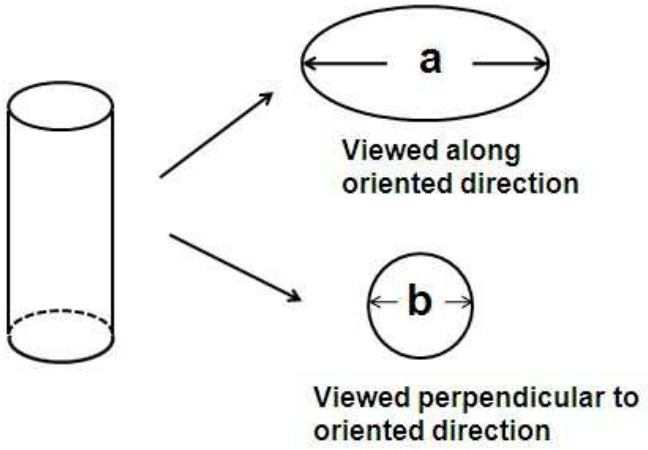

Fig. 5.11 Schematic of the oriented cells viewed along and perpendicular to oriented direction, respectively.

5.3.1 C-oriented cell morphologies and the mechanical properties

Fig. 5.12 shows the cell morphologies of c-oriented foams with different orientation degree (0.3 and 0.5), viewed along and perpendicular to c-axis, respectively. The foaming conditions are the same with that of Fig. 5.6b, and the relative densities of foamed samples are also similar to that of Fig. 5.6b (0.3±0.02). As expected, the cell morphologies viewed along and perpendicular to the oriented direction are similar to the ellipse and the round, respectively. Moreover, the average cell size of the cell morphologies viewed perpendicular to c-axis is smaller than that of the cell morphologies viewed along c-axis (see Fig. 5.12b and d, or Fig. 5.12a and c). Especially for Fig. 5.12b and d, with the highly oriented cells along c-axis, the solid area (cell walls) on the impact section is finely segregated by the small cells (Fig. 5.12d). Fig. 5.13 shows the change of the solid area fraction on fracture surface of the c-oriented foams as the function of orientation degree. The samples of Fig. 5.6b are used as the reference of isotropy one (orientation degree is 0). It is indicated that

with the oriented foaming along c-axis, the solid area fraction on fracture surface significantly increases with the orientation degree increase. On the other hand, the relative densities of those samples are nearly the same (0.3±0.02). Therefore, a foam with high solid area fraction on fracture surface and low relative density is achieved by c-axis oriented foaming.

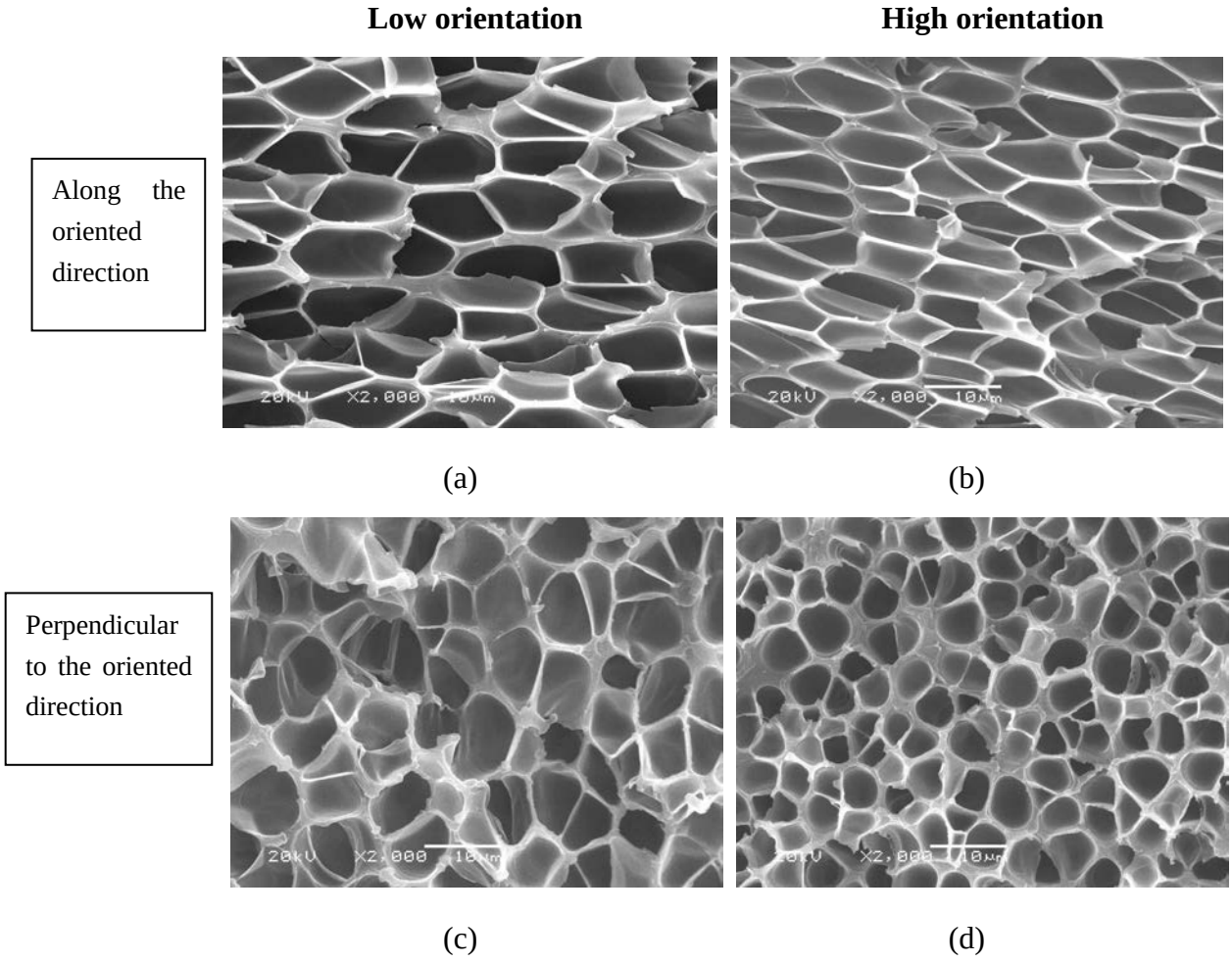

Fig. 5.12 SEM images of cell morphologies with different orientation degrees viewed long different directions. (a) Orientation degree is 0.3, viewed along c-axis; (b) orientation degree is 0.5, viewed along c-axis; (c) part (a) viewed perpendicular to c-axis; and (d) part (b) viewed perpendicular to c-axis. The white bar is 10 μm.

Fig. 5.14 shows the mechanical properties of the c-oriented samples with different orientation degrees, compared with that of non-oriented foams. Here, the sample of Fig. 5.6b is chosen as reference (orientation degree is 0). From Fig. 5.14a, the relative tensile strength increases slightly with the orientation of cells increase, while the relative tensile modulus has no change. It is indicated that the oriented cells perpendicular to the impact direction may play a role as fillers of zero modulus which could reinforce the tensile

strength more or less. On the other hand, from Fig. 5.14b, both the notched and non-notched relative impact strengths significantly increase with the orientation of cells increase. The results confirm the foregoing assumption that the oriented cell morphologies perpendicular to the impact direction with high solid area fraction on fracture surface, could successfully toughen the PS foam while still keeping its low density. Moreover, the notched relative impact strengths are always higher than those of non-notched ones, which further verifies the foregoing conclusion that the bubbles in the PS matrix could increase the crack propagation energy during the impact process.

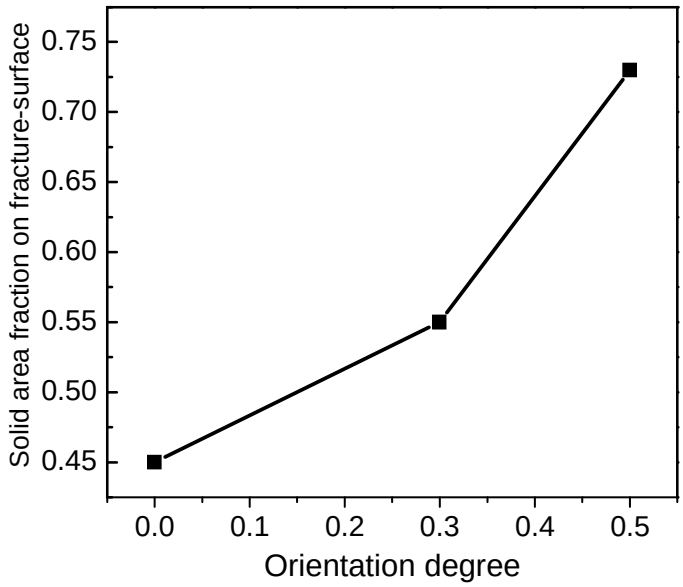

Fig. 5.13 The change of solid area fraction on fracture-surface of the c-oriented foams as the function of orientation degree. The sample of Fig. 5.9b is chosen as the reference of isotropy one (orientation degree is 0).

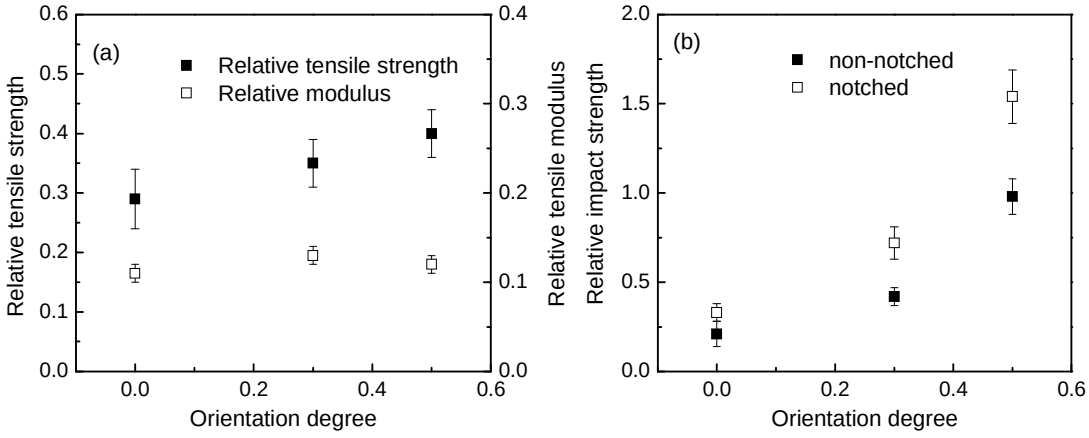

Fig. 5.14 Comparison of the mechanical properties of the c-oriented foams with different orientation degrees. The relative densities of the samples are all about 0.3±0.02.

It should be noted that the impact strength of the c-oriented PS foams with the oriented degree 0.5 is higher than that of isotropy foam whose relative density is 0.92 (see Fig. 5.1a and Fig. 5.5). Compared Fig. 5.1a with Fig. 5.12d, it is obvious that the solid area fraction on fracture-surface (A_s) of Fig. 5.14a is higher than that of Fig. 5.12d, and the cell size of Fig. 5.1a is smaller than that of Fig. 5.12d. Therefore, besides the foregoing two reseasons for toughening, the highly oriented bubbles in the foams must be another important reason. Study on the impact-fractured surface morphology is favorable to understanding the toughening mechanism. It is well known that the fracture process of the specimen under the load of impact includes at least two steps, i.e., crack initiation and crack propagation processed [76]. For unfoamed PS specimen, it has the typical brittle-fracture behavior. Fig. 5.15 depicts the SEM photographs of impact-fractured surface in the later stage of the crack propagation of PS foams with various orientation degrees. Fig. 5.15a shows the typical morphology of brittle-fracture mode with a flat and smooth surface. It indicates that, for the isotropy PS foams (orientation degree is 0), the strain energy absorption mainly occurs in the crack initiation zone, leading to the rapid breakdown of the crack propagation zone. In other words, the existed bubbles in the isotropy PS foams did not absorb the crack propagation energy efficiently. For Fig. 5.15b (orientation degree is 0.3), a rough surface is observed in the crack propagation zone which indicates that the c-oriented bubbles could absorb the crack propagation energy better than the isotropy ones. Especially, for Fig. 5.15c (orientation degree is 0.5), an obvious plastic deformation is observed in the later crack propagation zone. The cell walls were significantly stretched along the crack propagation direction (see Fig. 5.15d), suggesting the high fracture resistance. These plastic deformation zones absorbed large impact energy during the fracture process and made sample more ductile. It is attributed to the high solid area fraction on the fracture-surface and the finely segregated cell walls by the oriented bubbles. Furthermore, the highly oriented cells perpendicular to the impact direction play a role as fillers which could significantly increase the crack propagation energy during the fracture process.

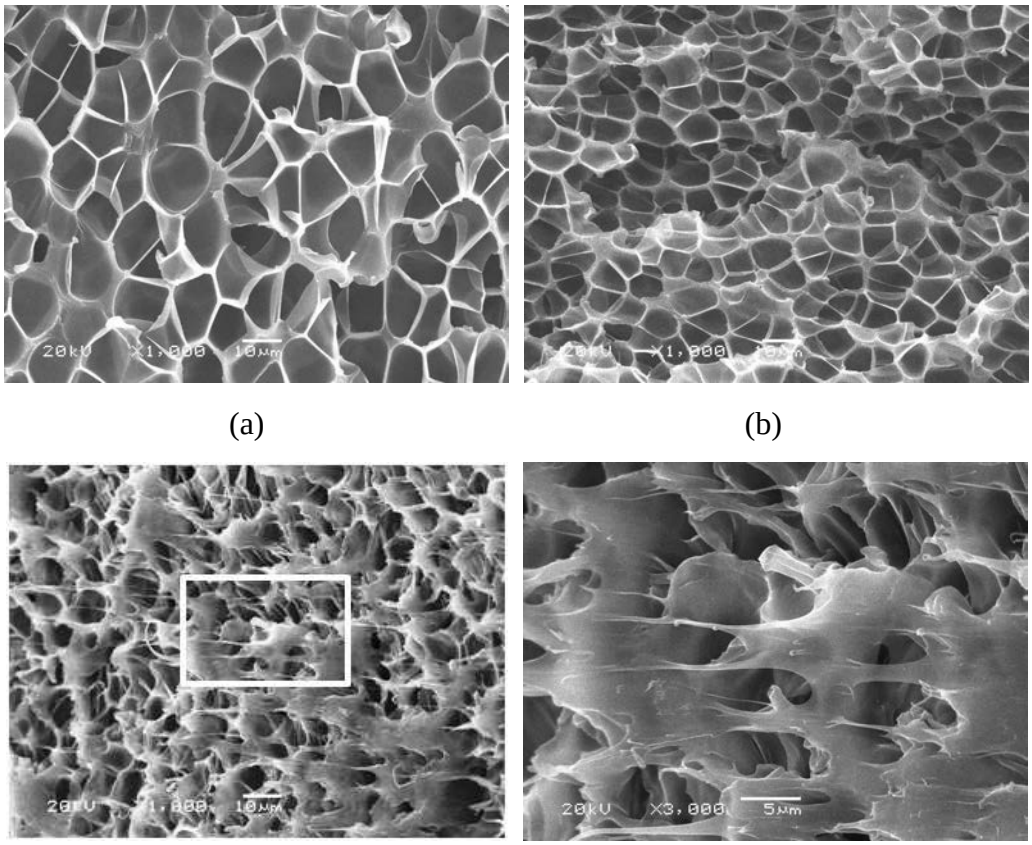

Fig. 5.15 SEM images of impact-fracture surface in the later stage of the crack propagation of PS foams with various c-axis orientation degree: (a) Orientation degree is 0, the white bar is 10 μm; (b) orientation degree is 0.3, the white bar is 10 μm; (c) orientation degree is 0.5, the white bar is 10 μm; and (d) magnification of the white rectangle in part (c), the white bar is 5 μm. The relative densities of the samples are all about 0.3±0.02. The white bar is 10 μm.

It is attributed to the high solid area fraction on the fracture-surface and the finely segregated cell walls by the oriented bubbles. In addition, the highly oriented cells perpendicular to the impact direction must be another important factor for toughening. As we discussed above, the cells in the polymer matrix can be considered as fillers in a multiphase system, in which the cell is one phase and the cell wall is another phase. In this way, the theories established for other multiphase systems can be applied to foamed polymers, where the cell is treated as a filler of zero modulus. The relation between the bubbles orientation and the fracture direction is schematically shown in Fig. 5.16. For c-oriented foams, the fracture propagation direction is perpendicular to the orientation direction of bubbles and the polymer matrix. Much energy is expected to break down the sample in the direction perpendicular to the orientation of bubbles and the matrix. For isotropy foams (see Fig. 16b), yield at the tip of a crack may be constrained by “plane

strain" conditions that exist, and this reduces the energy needed to drive the crack and, hence, reduces the measured toughness. For the a or b oriented foams (see Fig. 16c), the bubbles and the cell walls are parallel to the impact direction. Therefore, it is much easier to break down the sample in the direction parallel to the orientation of bubbles and the matrix. This will be discussed in detail in the next section.

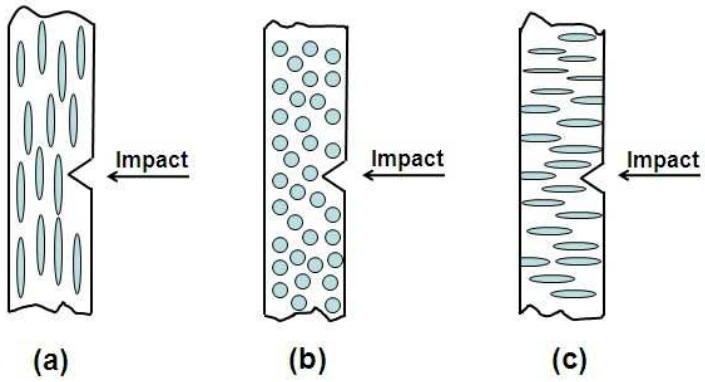

Fig. 5.16 The schematic representation of the relation between the bubbles orientation and the fracture propagation direction. (a) c-oriented bubbles, (b) isotropy bubbles, (c) a or b-oriented bubbles.

Fig. 5.17 shows SAXS patterns of PS foams with various c-axis orientation degrees. The cell oriented direction of samples is shown in Fig. 5.17, and the measurement direction is vertical. Typically, the equatorial streak in SAXS pattern is attributed to the formation of an oriented structure in nano size parallel to the oriented direction. The meridional maxima are attributed to the oriented structure perpendicular to the oriented direction. The isotropy scattering pattern of Fig. 5.17a indicates the no obvious orientation in PS foam matrix with the isotropy cells. On the other hand, with the oriented foaming, an obvious increase of reflections along the equator is observed (Fig. 5.17b-c) which indicates the oriented structure in nano size generated parallel to the oriented direction. As the bubbles are in micron size and the PS is amorphous, the reason for the oriented structure in nano size after oriented foaming must be the molecular chains sheared by the bubbles growing along the oriented direction. The schematic of molecular chains oriented by the shearing of bubbles is depicted in Fig. 5.18.

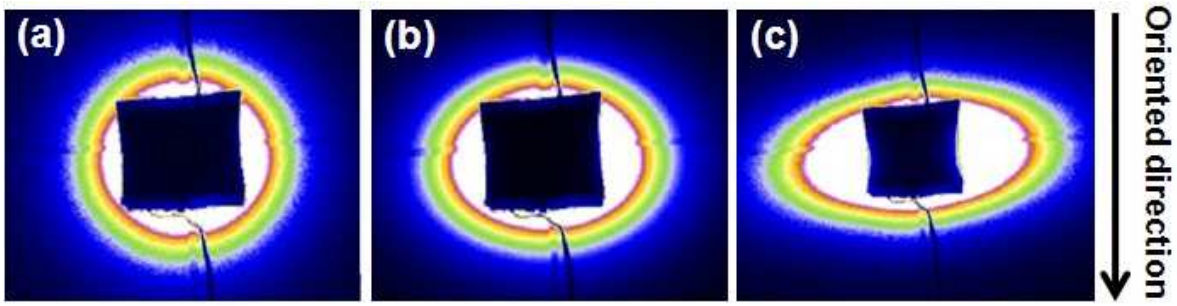

Fig. 5.17 2D SAXS images of PS foams with various c-axis orientation degree: (a) Orientation degree is 0; (b) orientation degree is 0.3; and (c) orientation degree is 0.5.

The network chains are entangled and in the random coil conformation with the saturation of $scCO_2$ before cell nucleation and growth, as shown in Fig. 5.18a. It is well known that the dissolution of CO_2 in the polymer increases the free volume between molecular chains and chain mobility [28, 29]. After the depressurization of gas, the supersaturated gas accumulates between molecular chains leading to cell nucleation and further growth (see Fig. 5.18b). As the cell growth is not isotropy but oriented, the molecular chains surrounding the bubbles will be sheared along the cell growth direction (see Fig. 5.18c). Therefore, part of the molecular chains is oriented along the cell growth direction after oriented foaming. It is well known that the oriented molecular chains may lead to the improvement of strength in oriented direction. This may be another reason for the increase of the relative tensile strength with the orientation degree increase (see Fig. 5.14a).

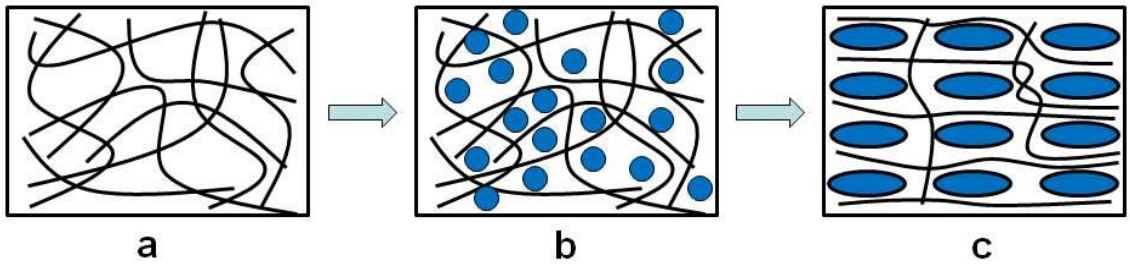

Fig. 5.18 Schematic of molecular chains oriented by the shearing of bubbles growth along the oriented direction: (a) the entangled network with the saturation of CO_2; (b) the cell nucleation and growth between the molecular chains after the gas depressurization; and (c) the molecular chains oriented by the shearing of the cell growth.

5.3.2 A-axis and b-axis oriented cell morphologies and the mechanical properties

According to the foregoing statement, the c-oriented cell morphologies perpendicular to the impact direction could significantly toughen the foams. Fig. 5.19 shows the relative notched impact strength of a-oriented and b-oriented foams with the function of orientation

degrees. The relative densities are all about 0.3±0.02. The impact strengths of both a-oriented and b-oriented foams decrease with the orientation degree increase, compared with that of non-oriented one (also the sample of Fig. 5.6b is chosen as reference). On the other hand, the impact strength of b-oriented foams is always higher than those of a-axis oriented ones.

Fig. 5.20 shows the typical cell morphologies of a-oriented and b-oriented foams viewed along the impact direction. The orientation degrees are both 0.5. As we discussed above, the larger of the solid area on the impact surface and the better dispersion of cell walls lead to the better mechanical properties (especially for the impact property). From Fig. 5.21, the solid area fraction (cell walls) on the fracture surface of non-oriented foam is larger than that of a-oriented and b-oriented foams. That's why the impact strengths of a-oriented and b-oriented foams are lower than that of non-oriented one. On the other hand, the solid area on the fracture surface of b-oriented foam is a little larger than that of a-oriented one (see Fig. 5.21). Moreover, comparing Fig. 5.20a with Fig. 5.20b, the restriction of cell walls on the fracture-surface along the impact direction of Fig. 5.20b is better than that of Fig. 5.20a. It's why the impact strength of b-oriented foam is higher than that of c-oriented one.

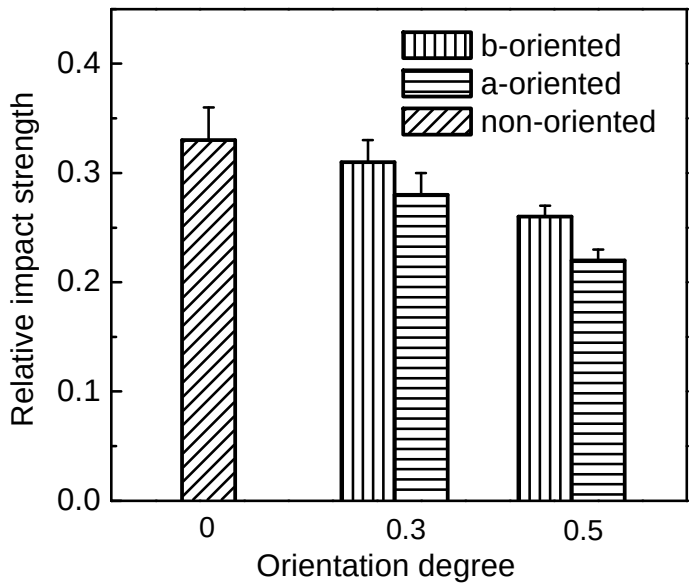

Fig. 5.19 The notched impact strength of a-axis and b-axis oriented foams with different orientation degree. The relative densities of the samples are all about 0.3±0.02.

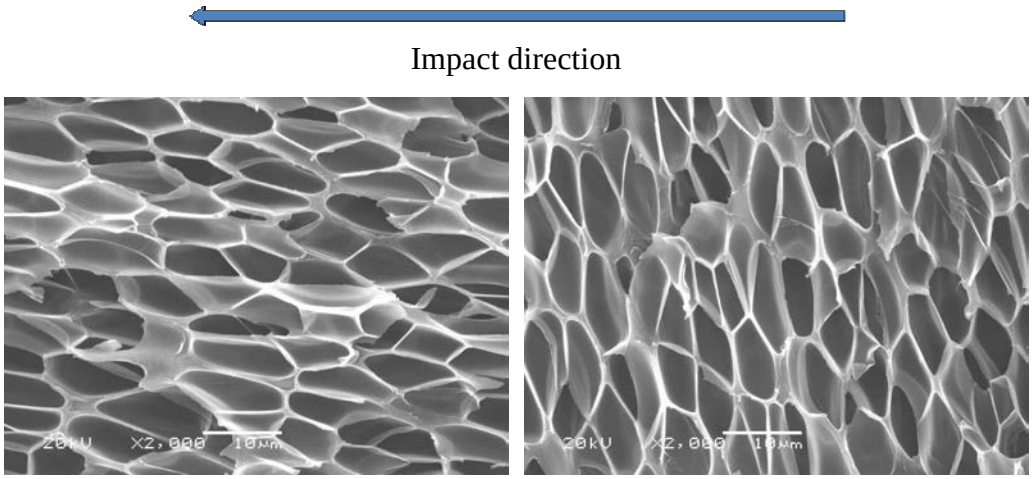

Fig. 5.20 SEM images of cell morphologies viewed along the impact direction with various oriented directions. (a) a-axis oriented, orientation degree is 0.5; (b) b-axis oriented, orientation degree is 0.5. The white bar is 10 μm.

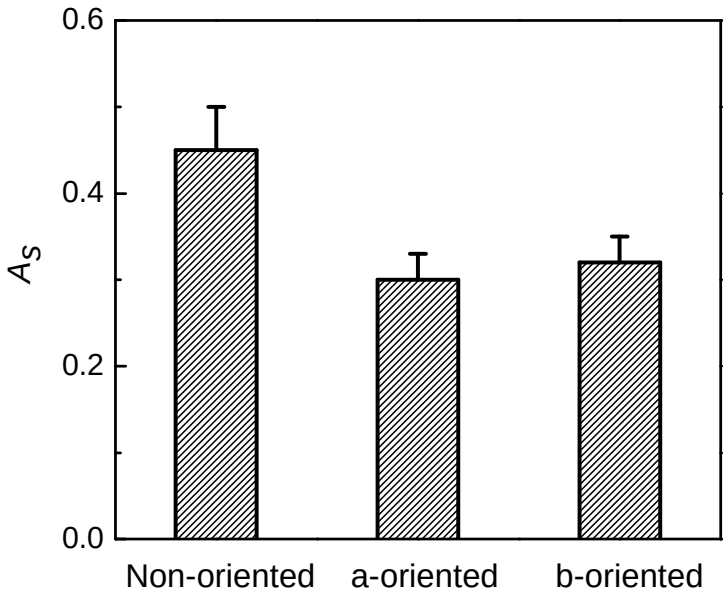

Fig. 5.21 Comparison of the ratio of solid area to impact section between the foams of non-oriented, a-oriented and b-oriented.

5.4 Conclusion

PS foams with isotropy cell morphology and oriented cell morphologies (a-oriented, b-oriented and c-oriented) were prepared. The tensile properties and the impact properties with and without notched were measured. For the isotropy cell morphologies, the mechanical properties of PS foams increase with the increase of relative density. When the relative density is constant, the cell size does not affect the tensile strength and modulus but has a weakly effect on the impact strength. The relative impact strength increases with the

cell size decrease. Besides, the values of relative impact strength of notched PS samples are always higher than those of non-notched ones, indicating that the bubbles could increase the crack propagation energy during the impact process. The solid area (cell walls) fraction on the fracture-surface and the cell walls finely dispersed by the bubbles are the main reasons for the toughening of PS foams.

For oriented foams, the cell morphologies oriented perpendicular to the impact direction could significantly enhance the mechanical properties of PF foams. The reasons for the toughening of c-axis oriented foams are as follows: a) the solid area fraction on the fracture-surface is higher than that of the isotropy foams with the same relative density (see Fig. 5.13); b) the cell walls on the fracture-surface are finely segregated by the cells, as the cells size is smaller than that of isotropic one (compare Fig. 5.12d with Fig. 5.6b); and c) the oriented cells perpendicular to the impact direction could increase the crack propagation energy during the fracture process (Fig. 5.15c-d). Moreover, the oriented cells along the tensile direction and the oriented molecular chains sheared by the bubbles may both lead to the improvement of strength in oriented direction. On the other hand, the cells oriented in the other two directions result in the poor impact properties, because their larger solid area fraction on the fracture-surface and the worse dispersion of cell walls by bubble compared with those of isotropy foams.

Chapter 6 Preparation of bi-modal cell structure polystyrene foams

6.1 Introduction

According to the investigation of chapter 5, to some extent, the cells in the polymer matrix can be considered as fillers of zero modulus in a multiphase system, in which the cell is one phase and the cell wall is another phase. The bubbles in the PS matrix could increase the crack propagation energy during the impact tests. The smaller bubbles could get the better toughness of foams while the relative density is constant. In addition, the finely segregated cell walls by bubbles play a important role for the mechanical properties.

Base on the above conclusion, the bimodal cell structure PS foams is raised as the following assumption: the small closed cells could act as a role of improving the mechanical properties of foam product, and on the other hand, large closed cells could be a role of reducing bulk density and lowing thermal conductivity of materials. This unique cell structure with both small and large cells homogenous distribution throughout the entire volume of the foam sample, which makes the cell walls non-uniform separation, may absorb the impact energy better than the uniform one. It is well-known that the mechanical properties and applications of polymeric foams are to a large extent determined by their cell morphologies [104-111]. For instance, polymer foams with big closed cells can be used in packaging, thermal insulation, cushioning and construction of low cost housing [112, 113]. On the other hand, polymer foams with open cells possess a wide range of applications in separation membranes [114], acoustic insulation [115], battery separators [116] and biomedical fields [117]. However, little research has been reported on preparing polymer foams with a bimodal distribution of cell sizes [21]. It is reported that this bi-modal cell structure has outstanding heat insulation property [118].

In this work, the bimodal cell structure was achieved by a two-step depressurization foaming process using $scCO_2$ as blowing agent. The influence of processing parameters and the nature of polymers on the final bimodal cell structure was first studied. Thereafter, the relationship between the cell structure and the impact property was investigated.

6.2 Formation of bi-modal cell structure

To create foams with a bi-modal distribution of cell sizes, the two-step depressurization batch foaming process conditions were as follows: the PS was first soaked at 20MPa and 100^{o}C till saturation and subsequently depressurized to an intermediate pressure (normally 15MPa in this work). The vessel was then maintained at that pressure for a certain period of

time (normally 1 h in this work) before the remaining pressure was released to the ambient one. Unless specified otherwise, the initial saturation pressure and temperature were 20MPa and 100^{o}C. Fig. 6.1 shows the typical changes in pressure and depressurization rate with time in the two-step depressurization process. Fig. 6.2 shows fracture cell morphologies of the PS foamed by two-step depressurization and one-step depressurization processes, respectively. It is seen clearly in Figure 6.2a-c that a bi-modal cell structure with both small and large cells is achieved successfully by the two-step depressurization process. This bimodal structure is evident throughout the entire volume of the foam sample. To study the mechanism of cell nucleation and growth in the two-step depressurization processes and to determine the effects of processing parameters on the morphology of bi-modal cells, a systematic study was carried out.

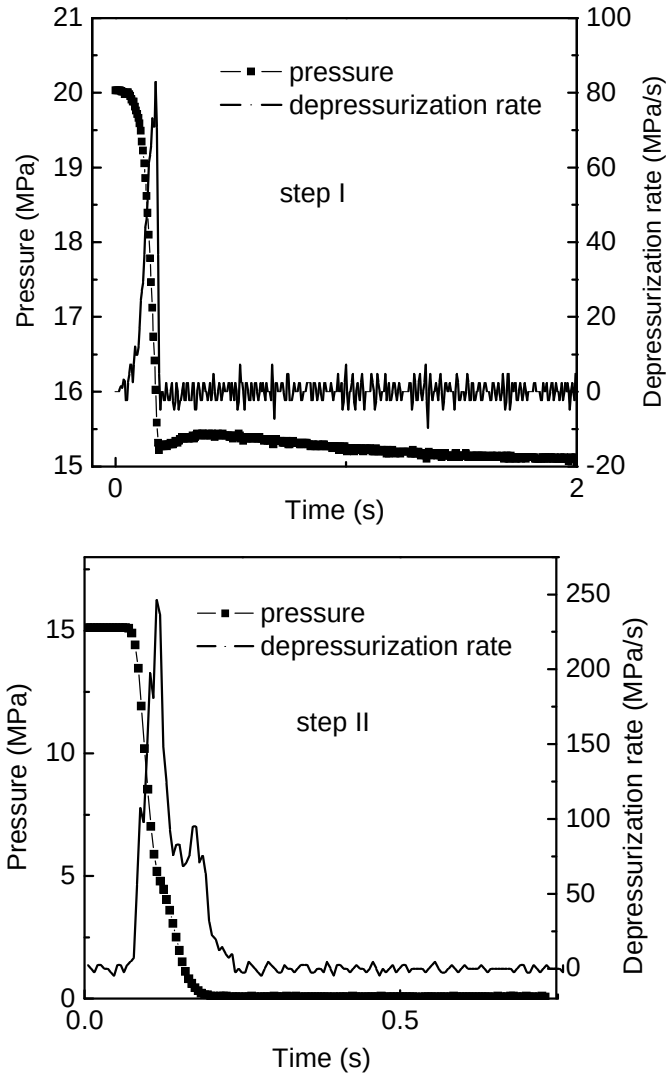

Fig. 6.1 Changes in pressure and depressurization rate with time during a typical two-step depressurization process.

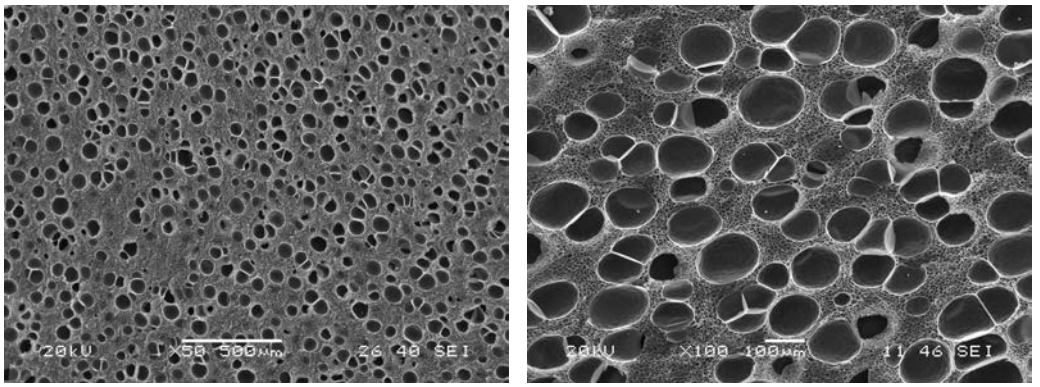

(a) (b)

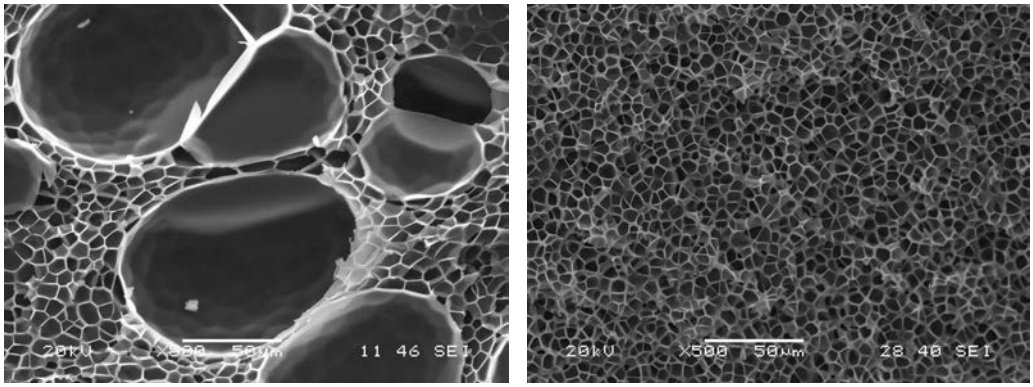

(c) (d)

Fig. 6.2 SEM images of the cell morphologies with bi-modal cell structure and uniform cell structure. (a) A two step-depressurization process: saturation at 20MPa and 100^{o}C. The pressure was released from 20 to 15MPa, was held at the latter pressure for 60min and then further depressurization to the ambient pressure. The scale bar is 500μm. (b) Image (a) at a higher magnification. The scale bar is 100μm. (c) Image (a) at an even higher magnification. The scale bar is 50μm. (d) A one-step depressurization process: saturation at 15MPa and 100^{o}C. The scale bar is 50μm.

6.3 Development of cell morphology in the two-step depressurization process

To observe the morphology development of cells in the two-step depressurization process and to determine which type of cell size (large or small one) was created in the first depressurization step, a series of experiments were carried out: (a) depressurization from 20 to 15MPa followed by immediate cooling operation from 100 to 0^{o}C. In other words, the high pressure vessel was immediately taken out of the oil bath and was put in an ice-water bath after the first stage. The temperature and pressure in the vessel were reduced to below 40^{o}C and the 10MPa in less than 2 min. (b) depressurization from 20 to 15MPa and holding for 60 min before cooling to 0^{o}C; (c) depressurization from 20 to 15MPa, holding at this pressure for 60 min and then further depressurization to the ambient pressure.

The SEM micrographs are shown in Fig. 6.3. From Fig. 6.3a and b, during the holding stage, the average cell size was increased from 4.3 to 23.0μm while the cell density was decreased from 7.9×10^8 to 7.0×10^6 cells/cm^3. This implies that in the holding stage after the first depressurization step, the majority of cells disappeared and a few of them grew larger. From Fig. 6.3b and c, the cell density of b and that of large cells in c were the same. This further corroborates the conclusion that the large cells in Fig. 6.3c were created during the holding stage after the first depressurization step.

Why did the majority of cells disappear in the holding stage after the first depressurization while the remaining ones kept growing larger? There were two reasons. First, cells in the polymer matrix were not stable during the holding stage because the holding temperature was above the T_g of the $scCO_2$ plasticized PS [119]. Neighboring cells tended to collapse into larger ones in order to reduce the total gas-polymer interfacial energy. Second, the gas concentration in the un-foamed regions surrounding the existing cells was higher than that inside the cells when the pressure was suddenly reduced to an intermediate value and was held at this latter value. During the holding stage, the supersaturated gas diffused into the existing cells and promoted their growth. In summary, in the holding stage, the majority of cells collapsed in favor of the growth of the remaining ones through the diffusion of gas from the unfoamed regions to existing cells and interactions among them.

In the second depressurization step, the supersaturated gas would either expand the existing cells by gas diffusion or nucleate additional microcells in the regions surrounding those cells. Since all the gas was released in 1 or 2 seconds, the temperature of the sample went below its T_g. As a result, its bi-modal cell structure was retained.

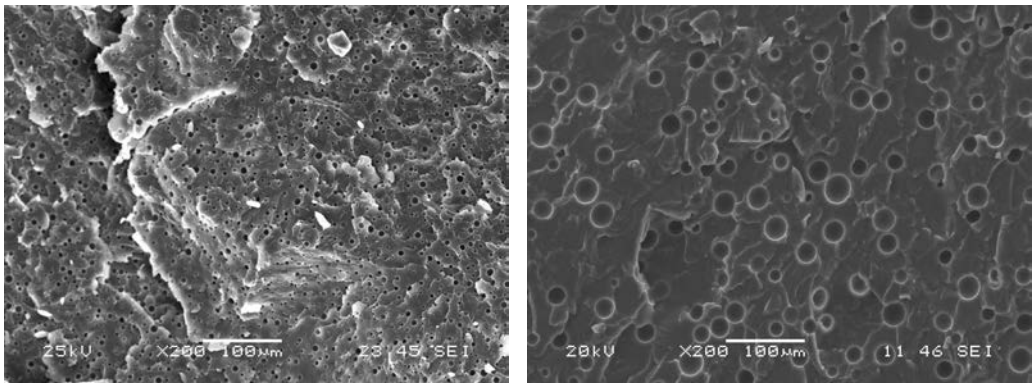

(a) (b)

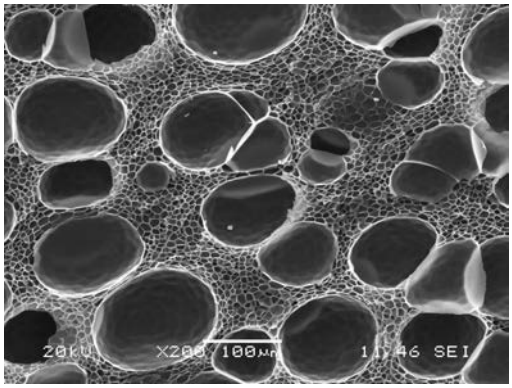

(c)

Fig. 6.3 SEM micrographs showing the development of cell morphologies in a two-step depressurization foaming process under the saturation conditions of 100^{o}C and 20MPa, (a) depressurization to 15MPa followed by immediate cooling to 0 ^{o}C. The average cell size and cell density were 4.3 μm and 7.9×10^{8}cells/cm^{3}, respectively; (b) depressurization to 15MPa and holding at this pressure for 60 min before cooling to 0^{o}C. The average cell size and cell density were 23.0μm and 7.0×10^{6}cells/cm^{3}, respectively; (c) depressurization to 15MPa, and holding at this pressure for 60min before further depressurization to the ambient pressure. The average cell size and cell density of large cells were 97.6μm and 6.7×10^{6}cells/cm^{3}, respectively. All the scale bars are 100μm.

6.4 Development of cell morphology during the holding stage

As discussed above, in the holding stage, the development of the cell morphology was mainly affected by the following two factors: (1) growth of existing cells by the diffusion of the supersaturated gas from the un-foamed regions to them; (2) collapse of neighboring cells resulting in large ones. This is corroborated by Fig. 6.4. In the holding stage, as the holding temperature was above the T_g of the scCO_2 plasticized PS, the super-saturation gas in the un-foamed regions tended to diffuse into existing surrounding cells. As a result, the latter grew in size. Moreover, neighboring cells tended to collapse into larger ones in order to reduce the total gas-polymer interfacial energy. Those two processes could occur simultaneously. Fig. 6.5 shows the cell size and cell density of Fig. 6.4. The cell size indeed increased while cell density indeed decreased with increasing holding time.

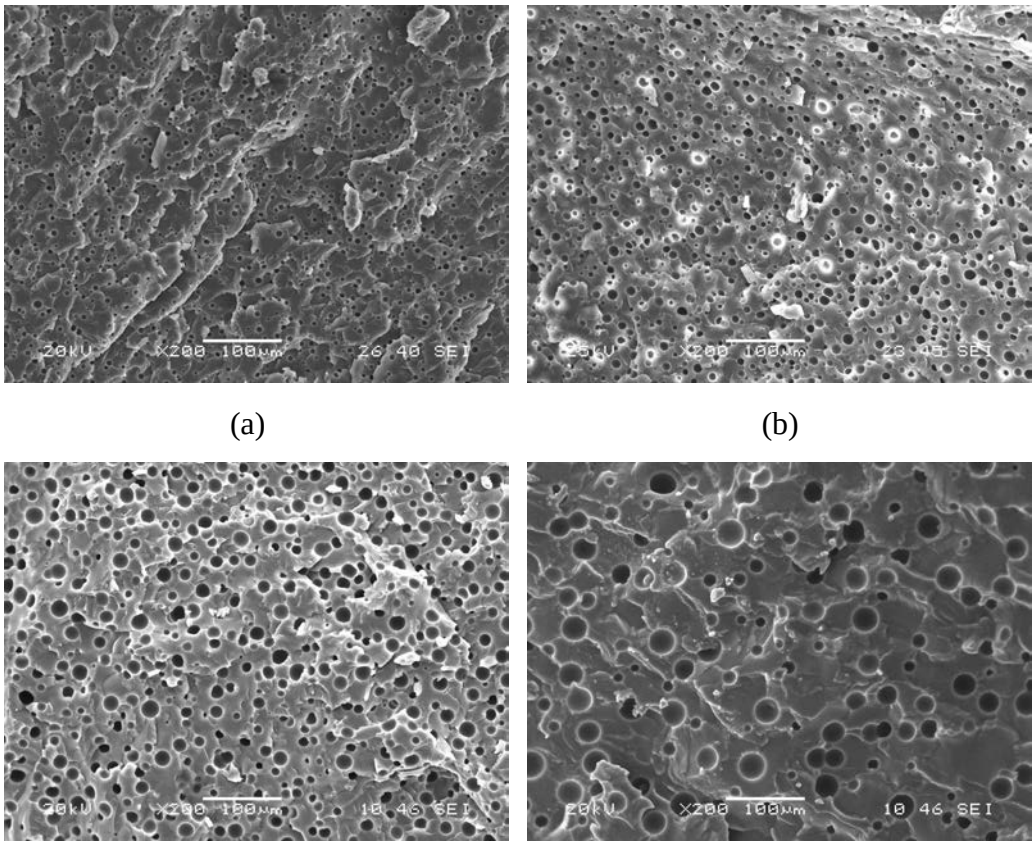

Fig. 6.4 Effect of the holding time on the cell morphology. Saturation at 100^{o}C and 20 MPa followed by depressurization to 15MPa, holding at this pressure for various time intervals before cooling to 0^{o}C: (a) 0min, (b) 10min, (c) 30min, (d) 60min. The scale bars are 100μm.

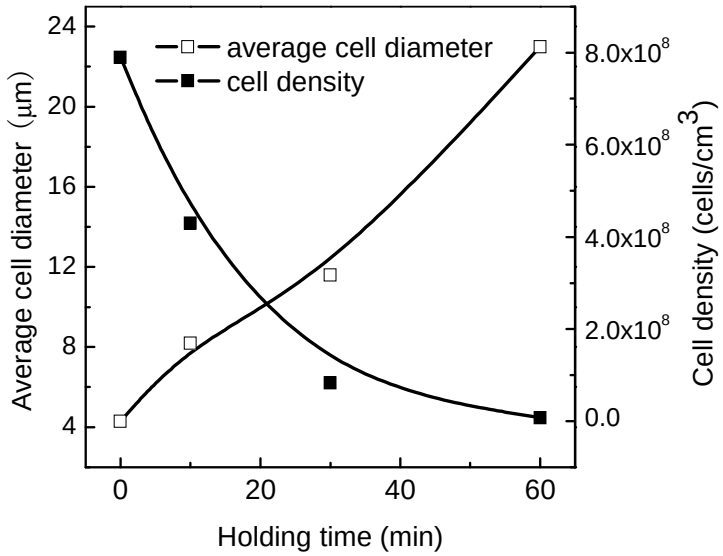

Fig. 6.5 Effects of the holding time on the average cell diameter and cell density of the PS foam. Saturation at 100^{o}C and 20MPa followed by depressurization to 15MPa, holding at this pressure for various time intervals before cooling to 0^{o}C.

6.4.1 Effect of gas super-saturation on cell growth during the holding stage

Since cell nucleation is a thermodynamic phenomenon and a kinetic process, there is an energy barrier for nucleation due to the interplay of the increased energy in the gas-polymer interphase, on the one hand, and the decrease in the Gibbs free energy of the system resulting from the phase separation, on the other hand [120, 121]. Thus, a certain amount of depressurization beyond the solubility pressure is needed to create a sufficient level of super-saturation to initiate cell nucleation. To validate this assumption the PS was saturated at 100^{o}C and 14.4MPa and then depressurized following Fig. 6.6a or b. Once the depressurization step ended, the sample was immediately cooled down to 0^{o}C.

Fig. 6.6a and Fig. 6.7a show that cell nucleation cannot occur when ΔP is equal to 1MPa (from 14.4 to 13.4 MPa, Figure 6.7a). However the supersaturated gas will cumulate in the polymer for a certain time before it diffuses out of it in the holding period. Therefore, the gas concentration increases with the following depressurization (Fig. 6.6b) till it reaches a sufficient level to initial cell nucleation (Fig. 6.7b).

The above results further corroborated the assumption that after the first-step depressurization, a certain amount of supersaturated gas accumulated in the un-foamed region surrounding the existing cells as they had not reached the level of super-saturation to initiate cell nucleation. Therefore, during the subsequent holding period, as the holding temperature was above the T_g of the $scCO_2$ plasticized PS, the cumulated gas would diffuse into the neighboring cells to promote their growth.

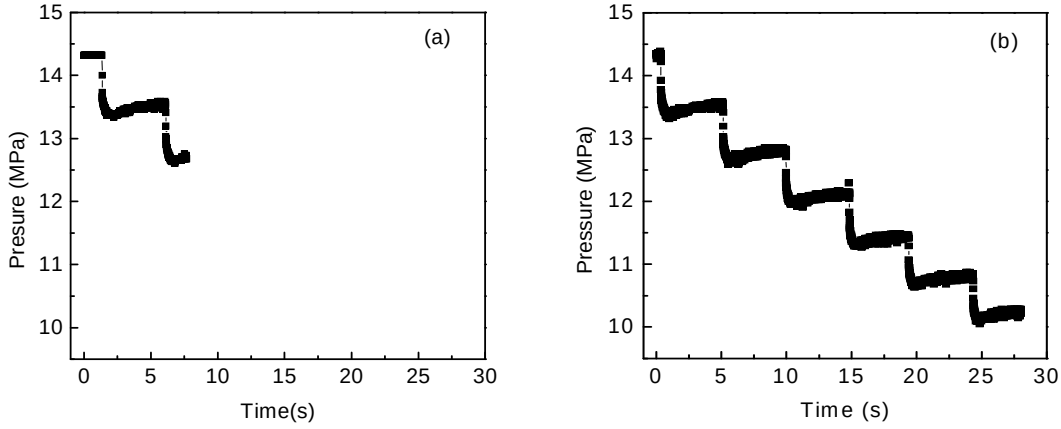

Fig. 6.6 Stepwise depressurization. The holding time between two adjacent steps is 5 seconds. (a) Depressurization from 14.4 to 12.5MPa, cooled to 0^{o}C before the samples were taken out. (b) Depressurization from 14.4 to 10MPa, cooled to 0^{o}C before the samples were taken out.

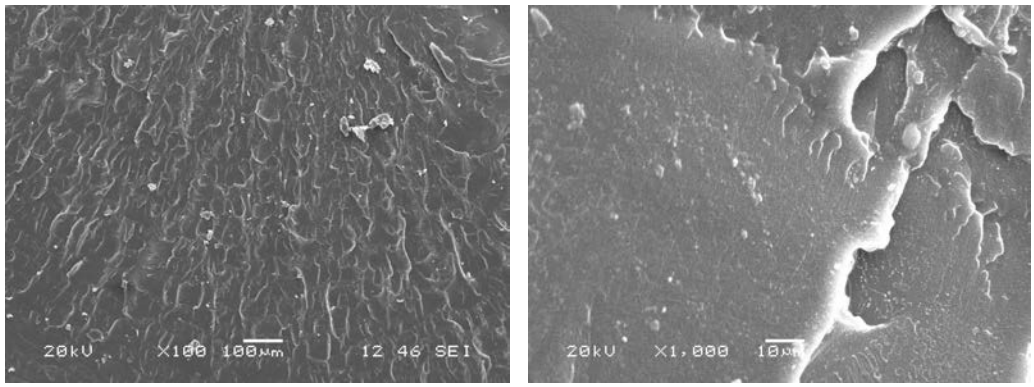

(a) (b)

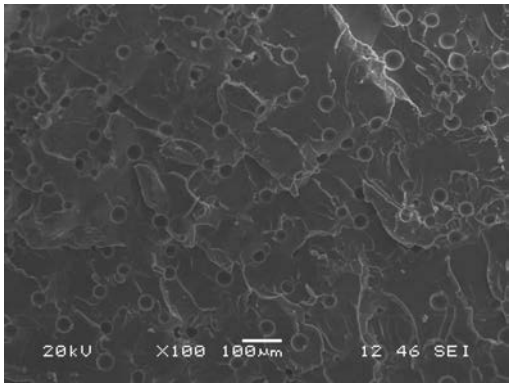

(c)

Fig. 6.7 SEM images of the PS foamed by two different types of depressurization profiles (Figure 6.6a and b, respectively). (a) No foaming; (b) image (a) at a much higher magnification confirming that there was no foaming; (c) Foaming occurred.

6.4.2 Interaction between small and large cells during the holding stage

To study the interaction among cells during the holding stage, a series of experiments was done. The sample of Fig. 6.3a was re-saturated at 15MPa and 100^{o}C for 0, 10, 30, 45 or 60 min and then cooled to 0^{o}C before it was taken out. From Fig. 6.8, the collapse and growth of cells occurred simultaneously till all the cells disappeared as the holding time increased. As discussed above, the existing cells in the polymer matrix were not stable during the holding stage and some of them collapsed and others grew larger in size. When the holding time was long enough, the gas inside the cells would tend to diffuse out of the polymer matrix, which ultimately led to complete disappearance of the cells.

It is worth noting that the sample in Fig. 6.3b had large cells whereas the one in Fig. 6.8e did not have any, even though they were held under the same saturation pressure and temperature conditions and for the same period of time. This is because after the first depressurization step, the sample of Fig. 6.3b was held at a fixed pressure. During that

holding stage, existing cells grew in size as a result of the diffusion of supersaturated gas from the un-foamed regions to them. On the other hand, the sample of Fig. 6.8e was re-saturated under the conditions under which the sample of Fig. 6.3b was held. However, it was done after the sample was taken out of the high pressure vessel. Therefore there was no supersaturated gas surrounding the cells. Moreover, the gas in the cells would diffuse out leading to their disappearance. These results further corroborate the above assumption that super-saturated gas indeed existed in the un-foamed regions during the holding stage and it diffused to the neighboring cells to promote their growth. However, it is possible that the cells of the sample shown in Fig. 6.3b would have been disappeared if it was maintained at the intermediate pressure for a longer period of time.

Comparison between Fig. 6.4 and Fig. 6.8 shows that at the beginning of the holding stage, the primary effect of the super-saturation gas is to promote the growth of the surrounding cells. In the latter holding stage, the concentration of the super-saturation gas decreases. Interactions among the cells become the main driving force for the collapse of the small cells and the growth of the large cells. In other words, at the beginning of the holding stage, the un-foamed area between the existed cells decreases as a result of the cell growth. As the holding stage continues, it increases as a result of the cell collapse (Fig. 6.4).

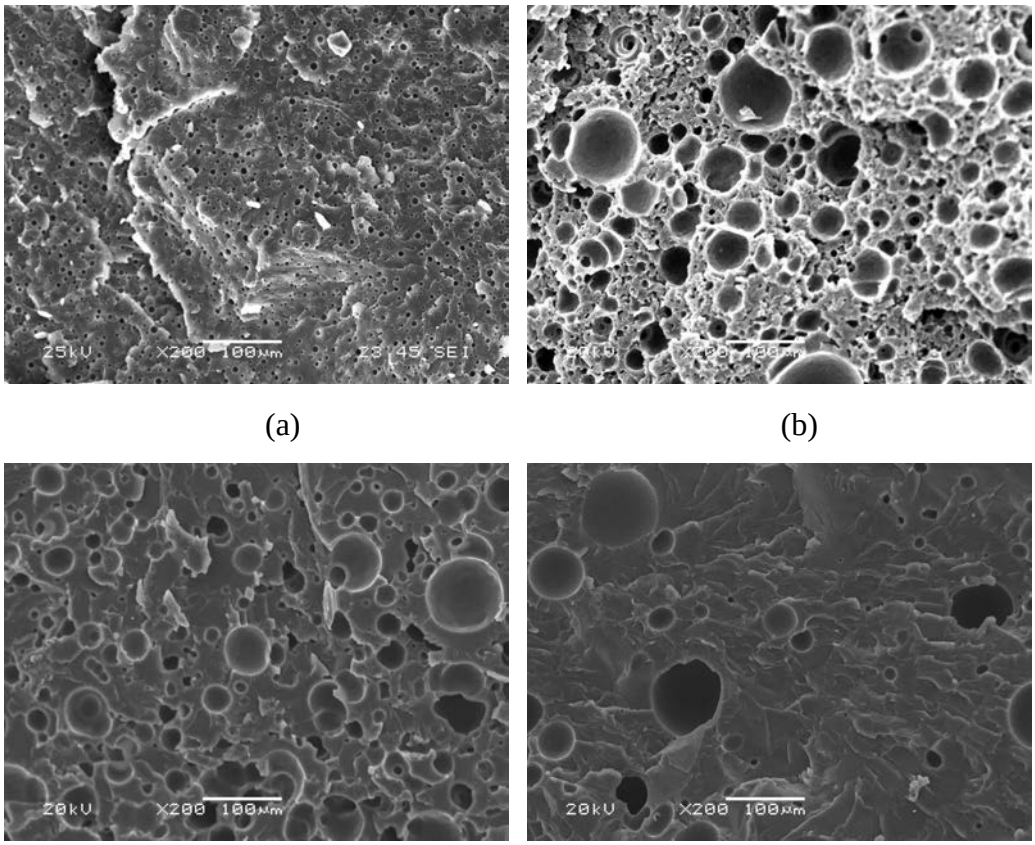

(a) (b)

(c) (d)

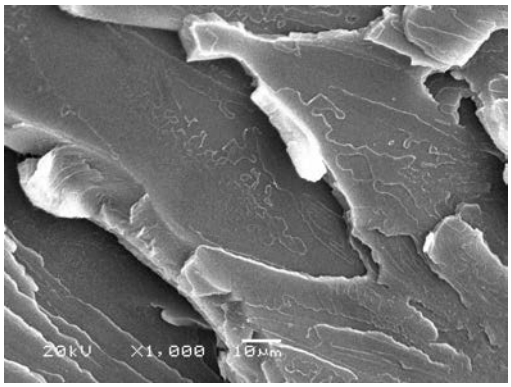

(e)

Fig. 6.8 Interaction among small cells and large cells during the holding stage. The holding time is (a) 0, (b) 10, (c) 30, (d) 45 and (e) 60 min. The scale bars of (a)-(d) are 100μm, and the scale bar of (e) is 10μm.

6.5 Controlling variables for the bi-modal cell structure

6.5.1 Holding time during the holding stage

The growth of large cells and the collapse of small ones occurred simultaneously during the holding stage. Fig. 6.9a-d show that the holding time may have a great effect on the bi-modal cell structure. When the holding time was 0 min, namely the second depressurization process immediately started operating after the end of the first depressurization process, the cell structure was not bi-modal. Both the nucleation and the growth of cells occurred during the depressurization process [14]. Inspection of Fig. 6.9a and Fig. 6.2d shows that the cell structure of the two-step depressurization process with a holding time of 0 min was similar to that of the one-step depressurization. In the case of the one-step depressurization process, during the depressurization both the expansion of existing cells and additional nucleation in the un-foamed regions took place by the gas diffusion. In the case of the two-step depressurization process, a large amount of supersaturated gas in the polymer as a result of the first depressurization step might already have diffused into the existing cells or diffused out of the polymer in the holding stage. If the second depressurization step proceeds immediately after the first depressurization step without any holding time, the nucleation and growth of the two step depressurization process are expected to be similar to those of the one step depressurization process.

Fig. 6.9b-d indicate that as the holding time increases, the area and cell density of small cells increase and their cell size deceases while the cell density of large cells decreases and their cell size increases. As stated above, in the holding stage, after the first depressurization step, the cell size indeed increases while cell density decreases with increasing holding time.

On the other hand, a decrease in the density of large cells is concomitant with an increase in the area of the un-foaming region. Thus more area is available for the second cell nucleation and growth during the subsequent depressurization stage. This results in an increase in the area and density of small cells and a decrease in their cell size.

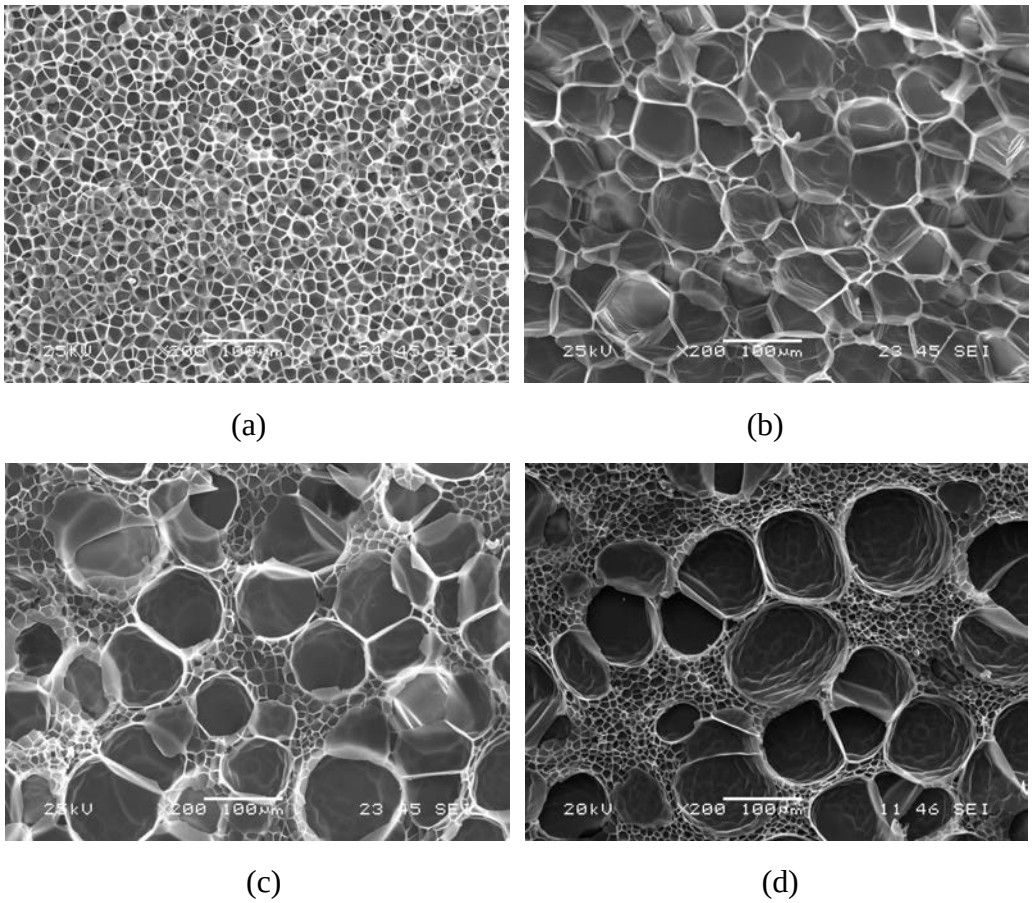

Fig. 6.9 Effect of the holding time on the cell morphology. The samples were saturated under 20MPa and 100^{o}C for at least 4 hours followed by rapid depressurization from 20 to 15MPa. They were held at the latter pressure for various periods of time before further rapid depressurization to the ambient pressure. (a) 0, (b) 10, (c) 30, (d) 60 min. The scale bars are 100μm.

Figs. 6.10a-b show the effect of the holding time on the final cell morphology in terms of the average cell diameter and cell density of large and small cells of Figs. 6.9b-d. It corroborates the above results that an increase in the holding time led to an increase in the cell density of small cells and a decrease in their size, on the one hand, and a decrease in the cell density of large cells and an increase in their size, on the other hand. This confirms that the holding time dictates, to some extent, both the sizes of small and large cells and the ratio between their densities.

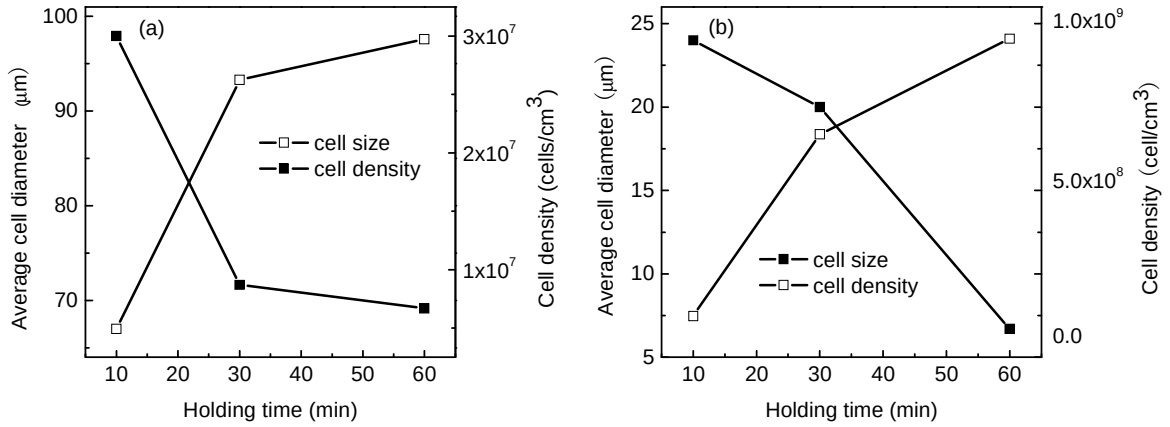

Fig. 6.10 Effect of the holding time on the final cell morphology in terms of the average cell diameter and cell density of large (a) and small (b) cells. Effect of the holding time on the cell morphology. The samples were saturated under 20MPa and 100°C for at least 4 hours followed by rapid depressurization from 20 to 15MPa. They were held at the latter pressure for various periods of time before further rapid depressurization to the ambient pressure.

6.5.2 Degree of depressurization in the first step

For a given temperature, the solubility of CO_2 in PS is approximately a linear function of the saturation pressure for low and moderate pressures [101, 102]. It reaches a plateau for high pressures [99]. In this study, the saturation conditions were 20MPa and 100°C, which were still in the region of linear function of solubility and pressure for CO_2 in PS. Therefore, a higher degree of depressurization results in a higher degree of super-saturation. As the degree of depressurization increases, a larger number of cells which correspond to the final large ones, is obtained in the first depressurization step. From Fig. 6.11, the volume ratio of the small cells to the large cells can be controlled by the degree of depressurization. However, there exists a lower depressurization threshold below which the first cell nucleation cannot be initiated. There also exists an upper depressurization threshold above which there will be no unfoamed space available for the second nucleation to occur.

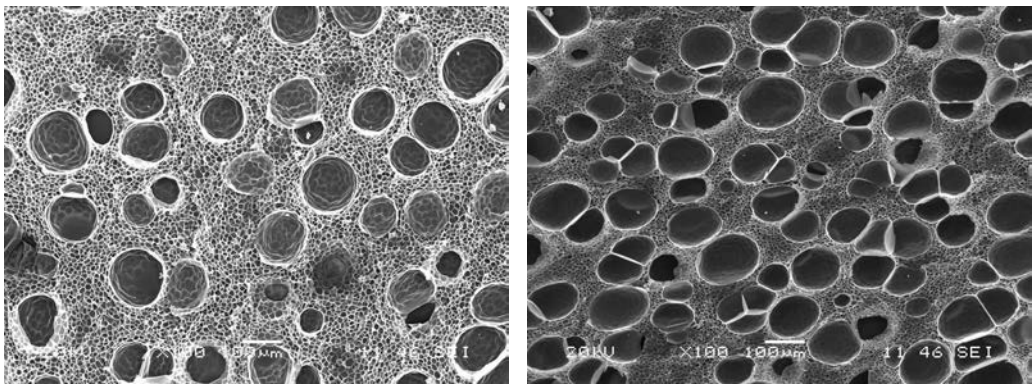

(a) (b)

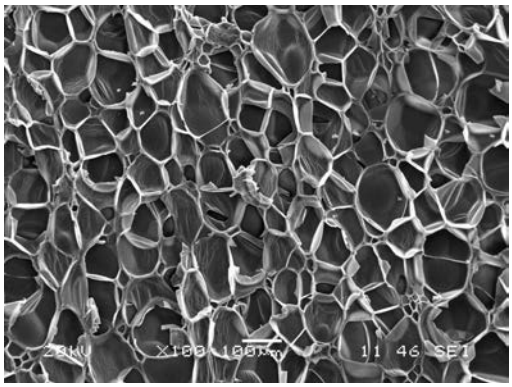

(c)

Fig. 6.11 Effect of the degree of depressurization on the cell structure of the PS foamed under the same conditions. (a) ΔP=3MPa , $V_{small}/V_{large} = 5$; (b) ΔP=5MPa , $V_{small}/V_{large} = 2$; (c) ΔP=8MPa , $V_{small}/V_{large} \approx 0$. The scale bars are 100μm.

6.5.3 Depressurization rate

In general, a higher depressurization rate can generate a higher cell density and a smaller cell size. This work studied the effect of the rate of the two depressurization steps on the final cell structure. Fig. 6.12a and b shows that the cell sizes of both large and small cells increase with increasing second depressurization rate while the cell density of small cells decreases. This is because as the gas diffusion rate increases with increasing second depressurization rate, more gas diffuses into the existing cells and consequently the amount of gas available for the cell nucleation decreases. Interestingly, Fig. 6.12a-c show that the first depressurization rate does not affect the cell sizes and cell densities of the large cells nor those of the small ones. This is because although the number of cells nucleated increases with increasing depressurization rate in the first depressurization step, most of the cells have collapsed in the holding stage. As a result, the effect of the first depressurization rate on the final cell structure is small.

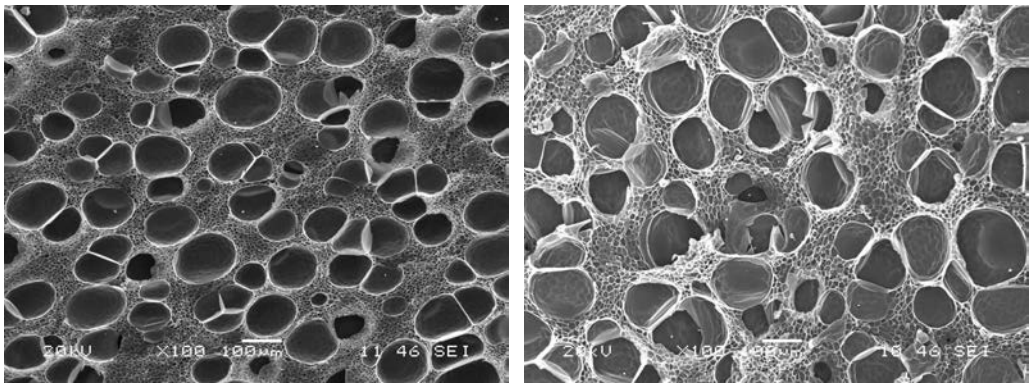

(a) (b)

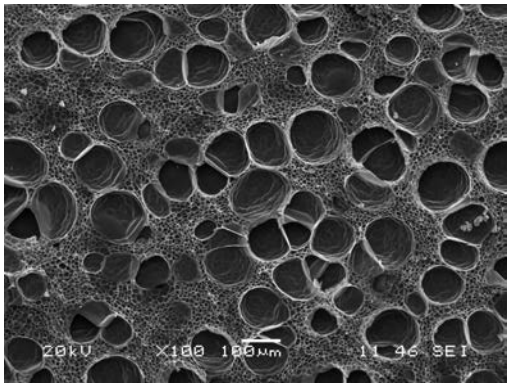

(c)

Fig. 6.12 Effect of the depressurization rates of the two steps on the cell structure of the PS foamed under the same condition: (a) 80/250 MPa/s, (b) 80/400 MPa/s, (c) 400/250 MPa/s. The scale bars are 100μm.

Table 6.1 Effects of the depressurization rates of the two stages on the average cell sizes and cell densities of large and small cells.

	80/250 MPa/s	80/400 MPa/s	400/250 MPa/s
D_{avg} of large cells (μm)	97.6	118.2	109.4
N_f of large cells (cells/cm^3)	4.5×10^6	3.3×10^6	4.5×10^6
D_{avg} of small cells (μm)	6.8	11.8	6.2
N_f of small cells (cells/cm^3)	2.9×10^{10}	6.4×10^9	2.5×10^{10}

6.5.4 Temperature

As the temperature increases, the viscosity of the polymer decreases and the force that resists to the cell growth decreases and the diffusivity of CO_2 within the polymer increases. On the other hand, the solubility of CO_2 in polymers decreases upon increasing temperature. From Fig. 6.13a-d, the effect of temperature of the second step on the cell structure is more significant than that of the first step. The average cell sizes of large and small cells increase

with the second-step temperature while the cell walls become thinner. This is because the temperature of the second-step affects not only the growth of large cells but also the nucleation and growth of small cells while the first one only affects the nucleation and growth of large cells in the first step. On the other hand, as stated above the cell structure can be significantly influenced by the holding stage conditions. Therefore, the effect of the first-step temperature on the final cell structure is small whereas the temperature of the second step can tune, to some extent, the cell sizes of both the large and small cells.

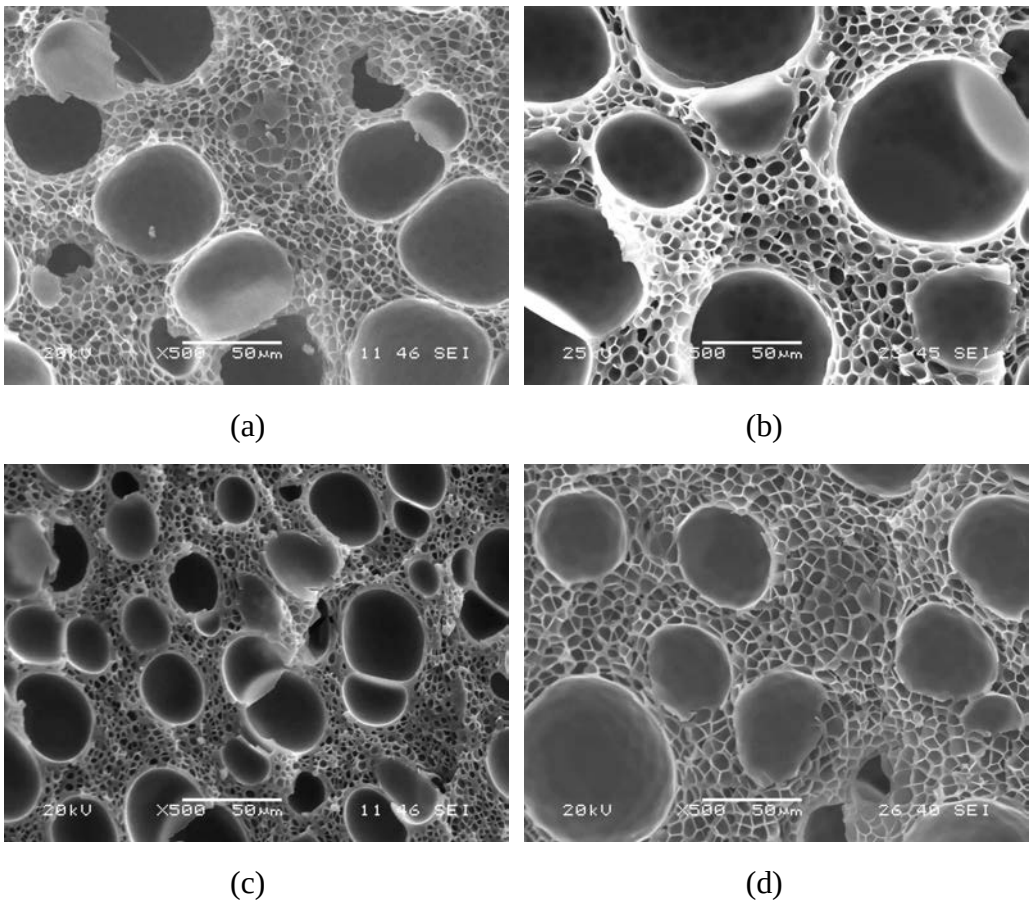

Fig. 6.13 Effects of the temperatures in the first and second steps on the cell structure of the PS foamed under the same conditions. (a) 100 ^{o}C/80 ^{o}C, (b) 120^{o}C/80 ^{o}C, (c) 110^{o}C/70 ^{o}C, (d) 110^{o}C/90 ^{o}C. The scale bars are 50 μm.

6.6 The relationship between cell structure and impact strength

Fig. 6.14 shows the notched impact strengths of the bi-modal cell structure foams with the same relative densities as the function of volume fraction of small cells (f_s). The f_s means the ratio of small cells volume to the whole cells volume. Therefore, the f_s of 100% represents the uniform cell structure containing all of small cells, and the f_s of 0 represents the uniform cell structure containing all of large cells. From Fig. 6.14, when the f_s is 80%,

the relative impact strength is higher than that of unifoam cell structure containing all of small cells. Moreover, the relative impact strength decreases with decreasing f_s.

According to the conclusion of chapter 5, the relative impact strength of isotropy foams increases with the relative density increase. The smaller bubbles could get the better toughness of foams while the relative density is constant. The area fraction of cell walls on the fracture-surface and the fine segregated cell walls by bubbles are the two main factors for the toughening of uniform microcellular foams. As the relative densities of the samples in Fig. 6.14 are all about 0.3±0.02 and the cell morphologies of foams are isotropy. Thus, the area fraction of cell walls on the fracture-surface is the same too. In other words, the segregation of the cell walls of the foams in Fig. 6.14 is the main reason for the change of the impact strength with the change of f_s. It is expected that the impact strength decreases with the decrease of f_s in the bi-modal foams. However, it is interesting that the impact strength of f_s of 80% is higher than that of 100%. It indicates that the bi-modal cell structure could better absord the impact energy than that of uniform one, although the large cells reduce the impact strength.

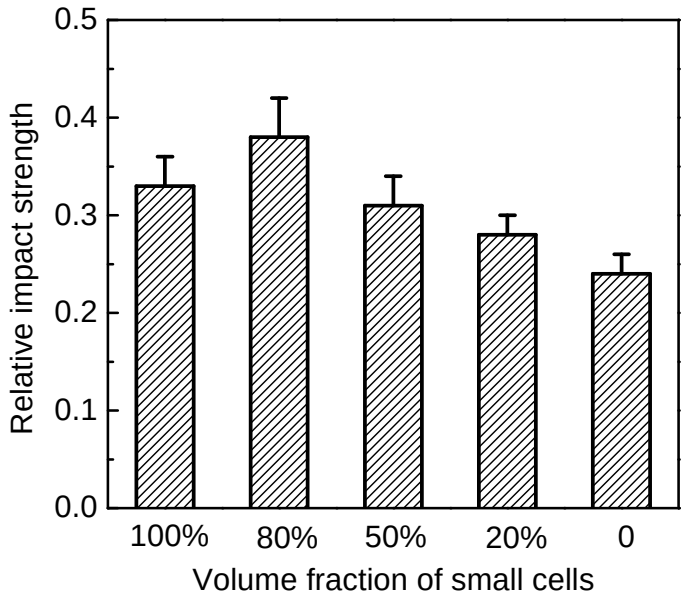

Fig. 6.14 The notched impact strength bi-modal cell structure foams with different volume fraction of small cells. The relative densities of the samples are all about 0.3±0.02. The cell size of large cells is 100±12 μm, and the cell size of small cells is 10±1.5 μm.

As we stated above, the segregation of the cell walls on the fracture-surface is the main reason for toughening, when the area fraction of cell walls on the fracture-surface is constant. The relation between the cell morphologies and the fracture propagation direction is schematically shown in Figure 6.15. Figure 6.15a, b and c represent the foams with small

cells, bi-modal cells and large cells, respectively. It is obvious that, for the foams with uniform cell structure, small cells are benefic for toughening (see Fig. 6.15a), compared with those of large cells (see Fig. 6.15c). However, if the ratio of small cells volume to the whole cells volume is proper (80%), the cell walls on fracture-surface (see Fig. 6.15b) separated non-uniformly by small and large bubbles, may induce the better absorption of crack propagation energy than the uniform one.

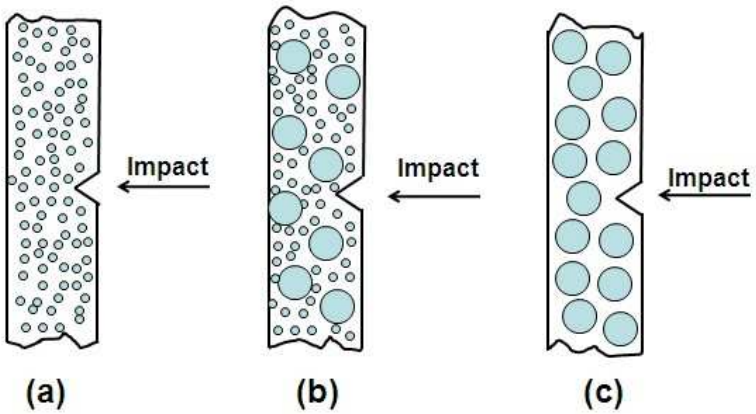

Fig. 6.15 The schematic representation of the relation between the cell morphologies and the fracture propagation direction. (a) small cells, (b) bi-modal cells, (c) large cells.

According to the foregoing statement, the bi-modal foams with the f_s of 80% get the better toughness than the uniform one while the relative densities are similar. Fig. 6.16 shows the relative impact strength of bi-modal cell structure foams and uniform cell structure foams as a function of relative density. The f_s of bi-modal foams are all 80%. For both bi-modal foams and uniform foams, the relative impact strength increases with the relative density increase. Moreover, the relative impact strengths of bi-modal foams are always higher than those of uniform one, in the range of relative density from 0.2 to 0.5. It further confirms the foregoing assumption that, when the f_s of bi-modal foams is 80%, the bi-modal cell structure could make better absorption of impact energy than the uniform one.

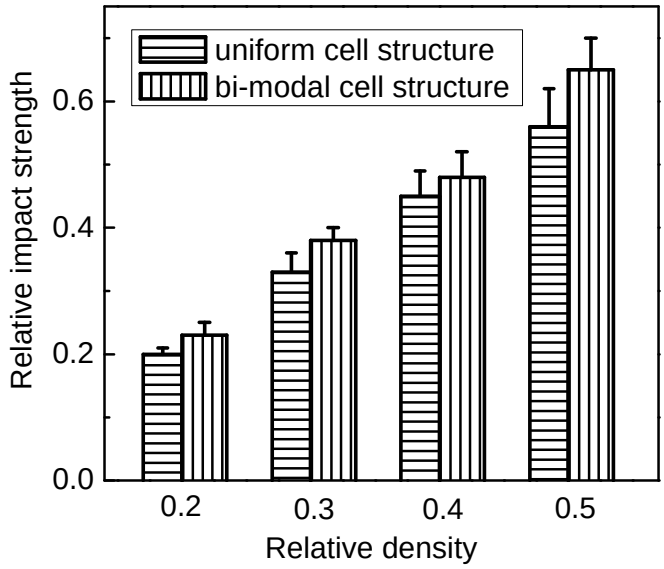

Fig. 6.16 The notched relative impact strength of bi-modal cell structure foams and uniform cell structure foams as a function of relative density. The f_s of bi-modal foams are all 80%. The average cell size of foams with uniform cell structure is 10 μm. The average cell size of large cells in the bi-modal foams is 100±12 μm, and the cell size of small cells in the bi-modal foams is 10±1.5 μm.

6.7 Conclusion

The bi-modal cell structure PS foams is successfully achieved by a two-step depressurization process using $scCO_2$ as the blowing agent. The holding stage between the two depressurization steps is the key to the control of the bi-modal cell structure. During the holding stage, larger cells further grow in size and smaller ones further decrease in size till complete collapse, by gas diffusion from small cells to large ones. The volume ratio of the large cells to the small ones can be tuned both by the holding time and the degree of depressurization in the first step. The depressurization rate and the temperatures of the first and second steps also influence the cell structure to a certain extent. On the other hand, the relationship between cell morphologies and impact properties of the bi-modal foams is investigated. When the relative density is constant, the impact strength of bi-modal foams decreases with the decrease of f_s. For both bi-modal foams and uniform foams, the relative impact strength increases with the relative density increase. Moreover, with the f_s of 80%, the relative impact strengths of bi-modal foams are always higher than those of uniform one, in the range of relative density from 0.2 to 0.5. It indicates that, when the f_s of bi-modal foams is 80%, the bi-modal cell structure could make better absorption of impact energy than the uniform one.

Chapter 7 Conclusion

The $scCO_2$ assisted toughening and foaming of PP and PS was studied in this work. The toughening of iPP by $scCO_2$ induced crystallization for the finely separation of rigid crystal phase and the soft amorphous phase in polymer matrix was first studied. The results indicates that the toughness of injection molded iPP specimens can be significantly improved by controlled shearing, CO_2 induced recrystallization and adequate cooling without loss of strength. Under shear, a high degree of orientation can be obtained with "shish-kebab" crystals formed in the shear zone. During the subsequent CO_2 treatment, a crystal network morphology may be formed as a result of an increase in the number of the primary lamellae and that of crosshatched subsidiary lamellae, which leads to an increase in the toughness. In addition, quenching in ice-water of $scCO_2$ treated iPP promotes the formation of nano-sized mesomorphic phase domains in the shear zone, which further toughens the iPP. The impact strength of the best toughened iPP is over 12 times that of the original one without loss in tensile strength and modulus.

Moreover, the highly oriented iPP samples with "shish-kebab" and "spherulite" were used for CO_2 foaming to investigate the effect of crystalline structure on the formation of cell nucleation and growth. The use of a highly oriented isotactic polypropylene (iPP) with a shish-kebab crystalline structure obtained by injection molding as a template allows obtaining nanocellular foams by CO_2 foaming in the solid state under appropriate foaming temperatures and CO_2 pressures. The underlying principle is localized cell nucleation and growth in amorphous domains confined by the shish-kebab crystalline domains. Therefore, nano-cells were generated in amorphous domains confined by shish-kebab crystalline domains which cannot foam. Moreover, at a chosen CO_2 pressure, the cell morphology depends very much on the foaming temperature. For example, when the CO_2 pressure is 15 MPa and the foaming temperature is 135^oC, only part of weak crystals is molten. When the temperature is increased to 140^oC, more crystals are molten including most of subsidiary lamellae or kebab and part of primary lamellae or shish. Thus oriented cells in submicron in size are generated and the un-foamed regions reveal the rest of the crystal structures. When the temperature is further increased to 143 ^oC, an open nanocellular morphology (See Fig. 4.10a-b) is successfully obtained with more crystals molten. However, when the temperature is increased to 146^oC, nearly all thin crystals are molten. As a result, cells in micrometer in size with smooth walls are formed due to weak restrictions of rigid crystals to cell nucleation, growth and coalescence. Moreover, the impact tests indicate that the nanocellular bubbles among the network crystals structure can toughening the $scCO_2$

treated iPP samples.

In addition, a systematic study of the effect of the foaming conditions and the cell structural parameters of PS foams on the mechanical properties was studied. PS foams with isotropy cell morphology and oriented cell morphologies were prepared. The tensile properties and the impact properties with and without notched were measured. For the isotropy cell morphologies, the mechanical properties of PS foams increase with the increase of relative density. When the relative density is constant, the cell size does not affect the tensile strength and modulus but has a weakly effect on the impact strength. The relative impact strength increases with the cell size decrease. Besides, the values of relative impact strength of notched PS samples are always higher than those of non-notched ones, indicating that the bubbles could increase the crack propagation energy during the impact process. The solid area (cell walls) fraction on the fracture-surface and the cell walls finely dispersed by the bubbles are the main reasons for the toughening of PS foams. For oriented foams, the cell morphologies oriented perpendicular to the impact direction could significantly enhance the mechanical properties of PS foams. The reasons for the toughening of c-axis oriented foams are as follows: a) the solid area fraction on the fracture-surface is higher than that of the isotropy foams with the same relative density; b) the cell walls on the fracture-surface are finely segregated by the cells, as the cells size is smaller than that of isotropic one; and c) the oriented cells perpendicular to the impact direction could increase the crack propagation energy during the fracture process. Moreover, the oriented cells along the tensile direction and the oriented molecular chains sheared by the bubbles may both lead to the improvement of strength in oriented direction. on the other hand, the cells oriented in the other two directions result in the poor impact properties, because their larger solid area fraction on the fracture-surface and the worse dispersion of cell walls by bubble compared with those of isotropy foams.

Finally, a two-step depressurization batch process is developed to produce bi-modal cell structure PS foams by using scCO_2 as the blowing agent. This unique cell structure with both small and large cells homogenous distribution throughout the entire volume of the foam sample must have particular properties which include both advantages of small cells and large cells. For instance, small closed cells could act as a role of improving the mechanical properties of foam product, and on the other hand, large closed cells could be a role of reducing bulk density. The results indicate that the bi-modal cell structure foams can be achieved by depressurization in two distinct steps and can be significantly affected by the process parameters. The process conditions at the holding stage between the two steps

are the key to controlling the bi-modal cell structure. When the relative density is constant, the impact strength of bi-modal foams decreases with the decrease of f_s. For both bi-modal foams and uniform foams, the relative impact strength increases with the relative density increase. Moreover, with the f_s of 80%, the relative impact strengths of bi-modal foams are always higher than those of uniform one, in the range of relative density from 0.2 to 0.5. It indicates that, when the f_s of bi-modal foams is 80%, the bi-modal cell structure could make better absorption of impact energy than the uniform one.

Acknowledgements

First and foremost I would like to express my best gratitude to my supervisors Prof. Guo-Hua HU, Prof. Ling Zhao, and Prof. Danielle BARTH. Their creative ideas of research, patient guidance and consistent encouragement push and inspire me to finish my PhD study. I also would like to express my great appreciation to associate Prof. Tao LIU and Prof. Sandrine HOPPE for providing much help and suggestions during my PhD study.

I am greatly thankful to my mates both in Chinese and French groups, Xiu-lei JIANG, Lei LI, Da-chao LI, Yan-tao LIU, Ming-fei DAI, Peng-jian GONG, Xiao-song LIAN, Jian LI, Zhou-bo CUI, Fang-lin ZHANG, Zheng-hui LI, Yuan FANG, Shiwei WANG and Sara RONASI, who kindly helped me a lot during my PhD study. Thanks are also due to my friends Wu-shun ZHOU, Pei-heng NI, Fang-fang ZHANG, Chuang LIU, Minglei YANG, Man LUO, Jin-bai ZHANG, Xiao-Bo SONG, Fei MAO, Yuan ZHOU, and Rong FAN, who have great contributions to my wonderful life both in China and France.

This study could not have been finished without the generous financial support from the National Natural Science Foundation of China (Grants 20976045, 20976046), Shanghai Shuguang Project (08SG28), program for New Century ExcellentTalents In University (NCET-09-0348), 111 Project (B08021), and “the Fundamental Research Funds for the Central Universities”. Thank China Scholarship Council for supporting my studying in France. Finally, I would like to express my great appreciation to my parents for their understanding and encouragement which support me to finish my PhD study.

References

[1] Cooper, A. I. *Adv. Mater*. **2003**, 15, (13), 1049-1059.

[2] Kumar, V.; Suh, N. P. *Polym. Eng. Sci.* **1990**, 30 (20), 1323-1329.

[3] Liu, T.; Hu, G.-H.; Tong, G.-S.; Zhao, L.; Cao, G.-P.; Yuan, W.-K. *Ind. Eng. Chem. Res.* **2005**, 44 (12), 4292-4299.

[4] Li, B.; Hu, G. H.; Cao, G. P.; Liu, T.; Zhao, L.; Yuan, W. K. *J. Supercrit. Fluid.* **2008**, 44 (3), 446-456.

[5] Asai, S.; Shimada, Y.; Tominaga, Y.; Sumita, M. *Macromolecules* **2005**, 38 (15), 6544-6550.

[6] Liu, T.; Hu, G. -H.; Tong, G. -S.; Zhao, L.; Cao, G. -P.; Yuan, W. -K. *Ind. Eng. Chem. Res*. **2005**, 44 (12), 4292-4299.

[7] Tong, G. -H.; Liu, T.; Hu, G. -H.; Hoppe, S.; Zhao, L.; Yuan, W. -K. *Chem. Eng. Sci*. **2007**, 62 (18-20), 5290-5294.

[8] Tong, G. -H.; Liu, T.; Hu, G. -H.; Zhao, L.; Yuan, W. -K. *J. Supercrit. Fluid*. **2007**, 43 (1), 64-73.

[9] Li, B.; Hu, G. -H.; Cao, G. -P.; Liu, T.; Zhao, L.; Yuan, W. -K. *J. Appl. Polym. Sci*. **2006**, 102 (4), 3212-3220.

[10] Li, B.; Zhu, X. Y.; Hu, G. H.; Liu, T.; Cao, G. P.; Zhao, L.; Yuan, W. K. *Polym. Eng. Sci*. **2008**, 48 (8), 1608-1614.

[11] Koga, Y.; Saito, H. *Polymer* **2006**, 47 (21), 7564-7571.

[12] Takada, M.; Tanigaki, M.; Ohshima, M. *Polym. Eng. Sci*. **2001**, 41 (11), 1938-1946.

[13] Miller, D.; Kumar, V. *Polymer* **2009**, 50 (23), 5576-5584.

[14] Chul B. Park, Daniel F. Baldwin, N.P. Suh, *Polym. Eng. Sci.* **1995**, 35, 432-440.

[15] Martini, J.; Waldman, F. A.; Suh, N. P. *SPE ANTEC:San Francisco, CA*, **1982**, 28, 674.

[16] Martini, J.; Suh, N. P.; Waldman, F. A. USA: Massachusetts Institute of Technology (**1984**), Pat. #4473665.

[17] Xu, Z.-M.; Jiang, X.-L.; Liu, T.; Hu, G.-H.; Zhao, L.; Zhu, Z.-N.; Yuan, W.-K. *J. Supercrit. Fluid*. **2007**, 41 (2), 299-310.

[18] Doroudiani, S.; Park, C. B.; Kortschot, M. T. *Polym. Eng. Sci.* **1998,** 38 (7), 1205-1215.

[19] Park, C. B.; Cheung, L. K. *Polym. Eng. Sci.* **1997,** 37 (1), 1-10.

[20] Bao, J.-B.; Liu, T.; Zhao, L.; Hu, G.-H. *J. Supercrit. Fluid.* **2011**, 55 (3), 1104-1114.

[21] Kelyn A. A.; Alan J. L.; Thomas J. M. *Macromolecules* **1998**, 31, 4614-4620.

[22] Galli, P.; Vecellio, G. *Prog. Polym. Sci*. **2001**, 26 (8), 1287-1336.

[23] Tian, Z.; Gu, X. P.; Wu, G. L.; Feng, L. F.; Fan, Z. Q.; Hu, G. H. *Ind. Eng. Chem. Res*. **2011**, 50 (10), 5992-5999.

[24] Ray, S. S.; Okamoto, M. *Prog. Polym. Sci.* **2003**, 28, 1539-1641.

[25] Thio, Y. S.; Argon, A. S.; Cohen, R. E.; Weinberg, M. *Polymer* **2002**, 43 (13), 3661-3674.

[26] Karnani, R.; Krishnan, M.; Narayan, R. *Polym. Eng. Sci*. **1997**, 37, 476-487.

[27] Grein, C. *Adv. Polym. Sci*. **2005**, 188, 43-104.

[28] Oda, T.; Saito, H. *J. Polym. Sci., Part B: Polym. Phys*. **2004**, 42 (9), 1565-1572.

[29] Teramoto, G.; Oda, T.; Saito, H. Sano, H. Fujita, Y. *J. Polym. Sci., Part B: Polym. Phys*. **2004**, 42 (14), 2738-2746.

[30] Meijer, H. E. H.; Govaert, L. E. *Prog. Polym. Sci*. **2005**, 30 (8-9), 915-938.

[31] Chen, H. B.; Karger-Kocsis, J.; Wu, J. S.; Varga, J. *Polymer* **2002**, 43 (24), 6505-6514.

[32] Varga, J. *J. Macromol. Sci. Phys*. **2002**, 41, 1121-1171.

[33] Wang, Y.; Zhang, Q.; Na, B.; Du, R.; Fu, Q.; Shen, K. *Polymer* **2003**, 44 (15), 4261-4271.

[34] Chen, Y.-H.; Zhong, G.-J.; Wang, Y.; Li, Z.-M.; Li, L. *Macromolecules* **2009**, 42 (12), 4343-4348.

[35] Schrauwen, B. A. G.; Breemen, L. C. A. v.; Spoelstra, A. B.; Govaert, L. E.; Peters, G. W. M.; Meijer, H. E. H. *Macromolecules* **2004**, 37 (23), 8618-8633.

[36] Kalay, G.; Michael, J. B. *J. Polym. Sci., Part B: Polym. Phys*. **1997**, 35, 241-263.

[37] Pantani, R.; Coccorullo, I.; Speranza, V.; Titomanlio, G. *Prog. Polym. Sci.* **2005**, *30* (12), 1185-1222.

[38] Bruckner, S.; Meille, S. V.; Petraccone, V.; Pirozzi, B. *Prog. Polym. Sci*. **1991**, *16* (2-3), 361-404.

[39] Meijer, H. E. H.; Govaert, L. E. *Prog. Polym. Sci*. **2005**, 30 (8-9), 915-938.

[40] Wang, K.; Chen, F.; Zhang, Q.; Fu, Q. *Polymer* **2008**, 49 (22), 4745-4755.

[41] Zhu, P.-W.; Tung, J.; Phillips, A.; Edward, G. *Macromolecules* **2006**, 39 (5), 1821-1831.

[42] Jiang, X. -L.; Liu, T.; Xu, Z. -M.; Zhao, L.; Hu, G. -H.; Yuan, W. -K. *J. Supercrit. Fluid*. **2009**, 48 (2), 167-175.

[43] Agarwal, P. K.; Somani, R. H.; Weng, W.; Mehta, A.; Yang, L.; Ran, S.; Liu, L.; Hsiao, B. S. *Macromolecules* **2003,** 36 (14), 5226-5235.

[44] Ogino, Y.; Fukushima, H.; Takahashi, N.; Matsuba, G.; Nishida, K.; Kanaya, T. *Macromolecules* **2006**, 39 (22), 7617-7625.

[45] Bao, J.-B.; Tiu, T.; Zhao, L.; Hu, G.-H. *Ind. Eng. Chem. Res.* **2011**, 50, 9632-9641.

[46] Siripurapu, S.; DeSimone, J. M.; Khan, S. A.; Spontak, R. J. *Adv. Mater*. **2004**, 16 (12), 989-994.

[47] Krause, B.; Koops, G. H.; van der Vegt, N. F. A.; Wessling, M.; Wübbenhorst, M.; van Turnhout, J. *Adv. Mater*. **2002**, 14 (15), 1041-1046.

[48] Yokoyama, B. H.; Li, L.; Nemoto, T.; Sugiyama, K. *Adv. Mater.* **2004**, 16 (17), 1542-1546.

[49] Xu, X.; Park, C. B.; Xu, D.; Pop-Iliev, R. *Polym. Eng. Sci.* **2003**, 43 (7), 1378-1390.

[50] Li, L.; Yokoyama, H.; Nemoto, T.; Sugiyama, K. *Adv. Mater*. **2004,** 16 (14), 1226-1229.

[51] Arora, K. A.; Lesser, A. J.; McCarthy, T. J. *Macromolecules* **1998**, 31 (14), 4614-4620.

[52] Leung, S. N.; Park, C. B.; Xu, D.; Li, H.; Fenton, R. G. *Ind. Eng. Chem. Res.* **2006**, 45 (23), 7823-7831.

[53] Nemoto, T.; Takagi, J.; Ohshima, M. *Macromol. Mater. Eng.* **2008**, 293 (7), 574-580.

[54] Colton, J. S.; Suh, N. P. *Polym. Eng. Sci.* **1987**, 27 (7), 485-492.

[55] Sun, H.; Sur, G. S.; Mark, J. E. *Eur. Polym. J.* **2002**, 38 (12), 2373-2381.

[56] Collias, D. I.; Baird, D. G.; Borggreve, R. J. M. *Polymer* **1994**, 35 (18), 3978-3983.

[57] Kabir, M. E.; Saha, M. C.; Jeehani, S. *Mater. Sci. Eng.: A* **2006**, 429 (1,2), 225-235.

[58] Rachtanapun, P.; Selke, S. E. M.; Matuana, L. M. *Polym. Eng. Sci.* **2004**, 44 (8), 1551-1560.

[59] Zeng, C.; Han, X.; Lee, L. J.; Koelling, K. W.; Tomasko, D. L. *Adv. Mater.* **2003**, 15 (20), 1743-1747.

[60] Kumar, V.; VanderWel, M.; Weller, J.; Seeler, K. *J. Eng. Mater. Technol.* **1994**, 116 (4), 439-445.

[61] Shimbo, M.; Higashitani, I.; Miyano, Y. *J. Cell. Plast.* **2007**, 43, 157-167.

[62] Kumar, V.; Weller, J.; Ma, M.; Montecillo, R.; Kwapisz, R. *Cell. Polym.* **1998**, 17 (5), 350-361.

[63] Waldman, F. M. S. Thesis, Massachusetts Institute of Technology, Cambridge, MA, **1982**.

[64] Collias, D. I.; Baird, D. G. *Polym. Eng. Sci.* **1995**, 35 (14), 1178-1183.

[65] Barlow, C.; Kumar, V.; Flinn, B.; Bordia, R.; Weller, J. *J. Eng. Mater. Technol.* **2001**, 123 (2), 229-233.

[66] Doroudiani, S.; Kortschot, M. T. *J. Appl. Polym. Sci.* **2003**, 90 (5), 1421-1426.

[67] Brandrup, S.; Immergut, E. M. Polymer Handbook, John Wiley & Sons: New York, **1975**.

[68] Turner-Jones, A.; Cobbold, A. J. *J. Polym. Sci.: Polym. Lett.* **1968**, 6, 539-546.

[69] Pornnimit, B.; Gottfried, W. E. *Adv. Polym. Technol.* **1991**, 11 (2), 91-98.

[70] Na, B.; Wang, K.; Zhang, Q.; Du, R.; Fu, Q. *Polymer* **2005**, 46 (9), 3190-3198.

[71] Varga, J.; Menyhard, A. *Macromolecules* **2007**, 40 (7), 2422-2431.

[72] Androsch, R.; Wunderlich, B. *Macromolecules* **2001**, 34 (23), 8384-8387.

[73] De Santis, F.; Adamovsky, S.; Titomanlio, G.; Schick, C. *Macromolecules* **2006**, 39 (7), 2562-2567.

[74] Androsch, R.; Wunderlich, B. *Macromolecules* **2001**, 34 (17), 5950-5960.

[75] Tanniru, M.; Yuan, Q.; Misra, R. D. K. Polymer **2006**, 47 (6), 2133-2146.

[76] Yuan, Q.; Misra, R. D. K. *Polymer* **2006**, 47 (12), 4421-4433.

[77] Yang, G.; Han, L.; Ding, H.; Wu, H.; Huang, T.; Li, X.; Wang, Y. *Mater. Sci. Eng. A* **2011**, 528 (3), 1382-1390.

[78] Jacoby, P.; Bersted, B. H.; Kissel, W. J.; Smith, C. E. *J. Polym. Sci., Part B: Polym. Phys.* **1986**, 24 (3), 461-491.

[79] Kalay, G.; Zhong, Z.P.; Allan, P.; Bevis, M.J. *Polymer* **1996**, 37 (11), 2077-2085.

[80] Zia, Q.; Androsch, R.; Radusch, H.-J.; Piccarolo, S. *Polymer* **2006**, 47 (24), 8163-8172.

[81] Wang, Z.-G.; Hsiao, B. S.; Srinivas, S.; Brown, G. M.; Tsou, A. H.; Cheng, S. Z. D.; Stein, R. S. *Polymer* **2001**, 42 (18), 7561-7566.

[82] Minami, S.; Tsurutani, N.; Miyaji, H.; Fukao, K.; Miyamoto, Y. *Polymer* **2004**, 45 (5), 1429-1432.

[83] Goel, S. K.; Beckman, E. J. *Polym. Eng. Sci.* **1994**, 34 (14), 1137-1147.

[84] Goel, S. K.; Beckman, E. J. *Polym. Eng. Sci.* **1994**, 34 (14), 1148-1156.

[85] Baldwin, D. F.; Park, C. B.; Suh, N. P. *Polym. Eng. Sci.* **1996**, 36 (11), 1437-1445.

[86] Naguib, H. E.; Park, C. B. *J. Appl. Polym. Sci.* **2008**, 109 (6), 3571-3577.

[87] Li, D.-C.; Liu, T.; Zhao, L.; Yuan, W.-K. *Ind. Eng. Chem. Res.* **2009,** 48 (15), 7117-7124.

[88] Tiu, L.; Zhao, L.; Zhu, X. Y. *J. Macromol. Sci., Part B* **2010,** 49 (4), 821-832.

[89] Tomasko, D. L.; Li, H.; Liu, D.; Han, X.; Wingert, M. J.; Lee, L. J.; Koelling, K. W. *Ind. Eng. Chem. Res.* **2003**, 42 (25), 6431-6456.

[90] Leung, S. N.; Wong, A.; Guo, Q.; Park, C. B.; Zong, J. H. *Chem. Eng. Sci.* **2009**, 64 (23), 4899-4907.

[91] Otsuka, T.; Taki, K.; Ohshima, M. *Macromol. Mater. Eng.* **2008**, 293 (1), 78-82.

[92] Taki, K.; Waratani, Y.; Ohshima, M. *Macromol. Mater. Eng.* **2008**, 293 (7), 589-597.

[93] Somani, R. H.; Yang, L.; Hsiao, B. S. *Polymer* **2006**, 47 (15), 5657-5668.

[94] Zhang, Z.; Handa, Y. P. *Macromolecules* **1997**, 30 (26), 8505-8507.

[95] Kelyn, A. A.; Alan, J. L.; Thomas, J. M. *Polym. Eng. Sci.* **1998**, 38 (12), 2055-2062.

[96] Miller, D.; Kumar, V. *Polymer* **2011**, 52 (13), 2910-2919.

[97] Chow, T. S. *Macromolecules* **1980**, 13 (2), 362-364.

[98] Chow, T. S.; Barlow, J. W.; Paul, D. R. *J. Appl. Polym. Sci.* **1985**, 30 (6), 2633-2642.

[99] Pantoula, M.; Panayiotou, C. *J. Supercrit. Fluid.* **2006**, 37, 254-262.

[100] Gibson, L. G.; Ashby, M. F. Cellular Solids: Structure and Properties; Pergamon: New York, **1988**.

[101] Sato, Y.; Takikawa, T.; Takishima, S.; Masuoka, H. *J. Supercrit. Fluid.* **2001**, 19 (2), 187-198.

[102] Sato, Y.; Fujiwara, K.; Takikawa, T.; Sumarno, Takishima, S.; Masuoka, H. *Fluid Phase Equil.* **1999**, 162 (1,2), 261-276.

[103] Knott, J. F. Fundamentals of fracture mechanics; Butterworth: London, **1973**.

[104] Fu, J.; Jo, C.; Naguib, H. E. *Cell. Polym.* **2005**, 24, 177-196.

[105] Matuana, L. M.; Park, C. B. *Cell. Polym.* **1998**, 17, 1-16.

[106] Shimbo, M.; Baldwin, D. F.; Suh, N. P. *Proceedings of the ACS Division of Polymeric Materials Science and Engineering* **1992**, 67, 512-513.

[107] Seeler, K. A.; Kumar, V.; *J. Reinforced Plastics and Composites* **1993**, 12, 359.

[108] Shimbo, M.; Baldwin, D. F.; Suh, N. P. *Polym. Eng. Sci.* **1995**, 35, 1387-1393.

[109] Sun, H.; Mark, J. E. *J. Appl. Polym. Sci.* **2002**, 86, 1692-1701.

[110] Tsivintzelis, I.; Angelopoulou, A. G.; Panayiotou, C. *Polymer* **2007**, 48, 5928-5939.

[111] Gendron, R.; Huneault M.; Tatibouet, J. *Cell. Polym.* **2002**, 21, 315–341.

[112] Kuhn, J.; Ebert, H. P.; Arduini-Schuster, M. C. *J. Heat Mass Transfer* **1992**, 35, 1795–1801.

[113] Huang Q.; Seibig B.; Paul, D. *J. Cell. Plast.* **2000**, 2, 112-125.

[114] Ahmed M. Y. S.; Park C. B.; Atalla N. *Cell. Polym.* **2006**, 25, 277-292.

[115] Arora P.; Zhang Z. *Chemical Reviews* **2004**, 104, 4419-4462.

[116] Hentze H. P.; Antonietti M. *Reviews in Molecular Biothchnology* **2002**, 90, 27-53.

[117] Park C. B.; Behravesh A. H.; Venter R. D. *ACS Symp. Ser.* **1997**, 669 (Polymeric Foams), 115-129.

[118] Lee, K. M.; Lee, E. K.; Kim, S. G.; Park, C. B.; Naguib, H. E. *J. Cell. Plast.* **2009**, 45, 539-553.

[119] Zhang, Z. Y.; Handa, Y. P. *J. Polym. Sci. Part B: Polym. Phys*. **1998**, 36, 977-982.

[120] Leung S. N.; Wong A.; Park C. B.; Guo Q. *Ind. Eng. Chem. Res.* **2009**, 48, 1921-1927.

[121] Guo Q.; Wang J.; Park C. B.; Ohshima M. *Ind. Eng. Chem. Res.* **2006**, 18, 6153-6161.

Nancy-Université
INPL

Pôle Recherche
Etudes Doctorales

Monsieur HU Guo-Hua
Professeur
LRGP - ENSIC

Vandœuvre-lès-Nancy, le 01 Décembre 2011

Référence : PR/2011/SR
Affaire suivie par : Stéphanie ROY 03 83 59 59 32
Objet : Soutenance de Thèse de Doctorat de l'I.N.P.L.

Monsieur le Professeur,

Vous avez accepté d'être membre du jury chargé d'examiner les travaux que présentera publiquement :

Monsieur BAO Jin-Biao

en vue de l'obtention du diplôme de :

DOCTEUR DE L'INSTITUT NATIONAL POLYTECHNIQUE DE LORRAINE

J'ai le plaisir de vous inviter à la soutenance qui aura lieu :

le : **16 décembre 2011** à : **15h30**
East -China University of Science and Technology - Shanghai

Le sujet est : **" Elaboration de polypropylène ou de polystyrène à l'aide du dioxyde de carbone supercritique : procédé - microstructure - propriétés mécaniques ".**

Vous trouverez ci-joint copie des rapports de présentation des rapporteurs.

Vous remerciant pour votre participation, je vous prie d'agréer, Monsieur le Professeur, l'expression de ma considération distinguée.

F. LAURENT
Président de l'INPL

Institut National Polytechnique de Lorraine
inpl@inpl-nancy.fr : www.inpl-nancy.fr

2 av. de la Forêt de Haye : BP 3
54501 Vandœuvre-lès-Nancy Cedex
FRANCE
Tél. : +33(0)3 83 59 59 59
Fax : +33(0)3 83 59 59 55

TITRE

Elaboration de polypropylène ou de polystyrène à l'aide du dioxyde de carbone supercritique : procédé – microstructure – propriétés mécaniques

RESUME

Le moussage du polypropylène (PP) et du polystyrène (PS) par le $scCO_2$ est étudié de manière systématique avec l'accent sur la relation entre le procédé, la microstructure et les propriétés mécaniques. La première partie de cette thèse porte sur l'amélioration de la résistance au choc du PP par cristallisation induite par le $scCO_2$. Dans un deuxième temps, le PP fortement orienté avec des structures shish-kebab et sphérolite est utilisé pour étudier l'influence de la structure cristalline sur la nucléation et la croissance des cellules pendant le procédé de moussage sous le $scCO_2$. Ensuite, les influences des conditions de moussage ainsi que celles des paramètres structuraux de la mousse de PS ont été étudiées. Les mousses de PS à cellules isotropes ont été comparées avec celles de PS à cellules orientées. Enfin, un procédé de moussage discontinu en deux étapes est développé afin de produire des mousses de PS à cellules bi-modales en utilisant le $scCO_2$ en tant qu'agent de moussage. Cette structure unique de petites et grandes cellules réparties de manière homogène au travers de l'ensemble du volume de la mousse confère à cette dernière des propriétés particulières.

MOTS-CLES

Polypropylène, polystyrène, $scCO_2$, cristallisation, mousse, propriétés mécaniques.

TITLE

Supercritical carbon dioxide assisted toughening of polypropylene or polystyrene:

process, microstructure and mechanical properties

ABSTRACT

In this work, $scCO_2$ induced foaming of PP or PS is systematically studied with emphasis on the relationship between process, microstructure and mechanical properties. The first part of the thesis deals with the toughening of iPP by $scCO_2$ induced crystallization for the fine separation of rigid crystalline domains and soft amorphous ones in the polymer matrix. The highly oriented iPP with "shish-kebab" and "spherulite" are then used for CO_2 foaming to investigate the effect of crystalline structure on the formation of cell nucleation and growth. In addition, the effect of the foaming conditions and the cell structural parameters of PS foams on the mechanical properties are studied systematically. PS foams with isotropic cell morphology and oriented cell one are prepared. Finally, a two-step depressurization batch process is developed to produce bi-modal cell structure PS foams by using $scCO_2$ as the blowing agent. This unique cell structure with both small and large cells homogenously distributed throughout the entire volume of the foam sample might have particular properties.

KEY WORDS

Polypropylene, polystyrene, $scCO_2$, crystallization, foam, mechanical property